COBALT GERMANIDE CONTACTS

COBALT GERMANIDE CONTACTS: GROWTH REACTION, PHASES, AND ELECTRICAL PROPERTIES

By **MOHAMED A. RABIE**, M.A.Sc.

A Thesis Submitted to the School of Graduate Studies in Partial Fulfilment of the Requirements for the Degree of Doctorate of Philosophy

McMaster University DOCTORATE OF PHILOSOPHY (2019) Hamilton, Ontario (Electrical and Computer Engineering)

TITLE: Cobalt Germanide Contacts: Growth Reaction, Phases, and Electrical Properties

AUTHOR: Mohamed A. Rabie, B.Sc. (Ain Shams University, Cairo, Egypt), M.A.Sc. (McMaster University)

SUPERVISOR: Dr. Yaser M. Haddara

NUMBER OF PAGES: viii, 110

Lay Abstract:

The main goal of this thesis is to create predictive empirical, mathematical, and physical models to help the designer of the semiconductor process technology to design high quality electric contacts, namely cobalt germanides, to their semiconductor devices, germanium based. The choice of cobalt germanides is motivated by their expected superior quality given the possibility of growing them in crystalline form. We settled a theoretical and experimental controversy regarding the first phase to form by conducting experiments demonstrating that low-temperature forming cobalt germanide phases are highly ordered and could serve as high quality contacts. A predictive physical based mathematical model was developed to assist the designer in obtaining the desired cobalt germanide phase for its needed electrical properties by design. Factors affecting the quality of the germanide were identified based on an extensive survey and the optimum choices for the parameters to obtain high quality contact were pointed.

Abstract:

This thesis is a sandwich thesis composed of three papers that are published in refereed journals or conferences. The first paper is a systematic experimental study conducted to identify the first phase to form during cobalt germanidation. Hexagonal β-Co_5Ge_3 was the first phase to form at temperatures as low as 227°C followed by monoclinic CoGe as the second phase at the same temperature. We also report for the first time that both phases that formed were highly ordered partial epitaxial crystal orientations suggesting that both of those low-temperature phases could potentially serve as high quality contacts for germanium based devices with a very low thermal budget which is advantageous for the process design. Those results contributed to a better understanding of cobalt germanidation leading to the first multiphase technology computer aided design model presented in the second paper. This kinetic model for cobalt germanide growth can predict the resulting phase based on anneal time, temperature, and ambient. The model has been calibrated to experimental results. This predictive model can help in the design of cobalt germanide contacts with low resistance and can serve as a general modeling framework for multiphase solid state reaction binary systems. A comprehensive survey of the experimental results for formation of cobalt germanides is discussed and the data are reconciled in the third paper. Factors affecting the resulting phases and their quality are identified and some optimum choices for the experimental parameters are pointed based on the survey. The role of germanium crystal orientation in ohmic and Schottky properties of the contact is analyzed. Fermi level pinning plays a role mainly on metal/(100) n-type Ge interfaces and its role is minimal on p-type Ge and other crystalline orientations. Schottky Barrier Heights for cobalt germanide contacts reported in the literature are surveyed. Crystalline cobalt germanides, forming when Co is deposited at high temperatures, are expected to have lower interface resistivities compared to those reported. The work is important because contact resistance has become one of the most important factors in advanced complementary metal oxide semiconductor (CMOS) technology and advanced devices already include germanium (Ge) in the source/drain regions of devices. It is also important because heating at the interface due to contact resistance is one of the key challenges in power devices and cobalt germanide can be used both for Si and Ge based devices as well as for gallium nitride (GaN) devices. The latter application is possible because cobalt germanide is lattice-matched to GaN.

Acknowledgements:

To my mother Seham: because I owe it all to you. Many thanks for the continuous support through this long journey! You always believed in me and your emotional support was key to this achievement.

To my father Abdel-Maksoud: Many thanks for your invaluable advice that motivated me not to stop till I reach the end goal.

To my wife Yasmin: Many thanks for your support and tolerance through this journey. You lived with me all the ups and downs of this graduate studies. Whether full time or part time, it always took from our time and you were always with me side by side. Your contribution to this work is significant.

To my supervisor Dr. Yaser Haddara: I am very grateful for your trust in me. Your guidance affected my life beyond the graduate studies. I always enjoyed our conversations. To me, you are not only a supervisor but an elder brother.

I would like to thank my children Alei, Zeyad, and Omar for helping to create a quiet and happy environment when needed during my studies.

A very special gratitude goes out to all the students who helped me in performing the experiments and reviewing the literature. I would like to specially mention Souzan Mirza who worked regularly and extensively with me in two of the three papers, Yujie Hu who continued the journey with me to the end line, Ishaq Aden-Ali, Ryan Koh, and Efe Ijevu.

I am also grateful to McMaster team who helped to perform the experiments with special mention of Victoria Jarvis and Doris Stevanovic.

In the end and in the beginning and always Alhamdulillah: thanks to God for making this possible and peace upon his prophet Muhammad who taught us what made our life meaningful.

Table of Contents

Lay Abstract: iii

Abstract: iv

Acknowledgements: v

Table of Contents vi

Declaration of Academic Achievement viii

Chapter 1 Introduction 9

1- Motivation 10

2- Objective and Outline 15

References: 18

Chapter 2 First Phase to form during Cobalt Germanidation 21

1- Introduction 24

2- Experimental Procedure 27

3- Results and Discussion 29

4- Conclusion 42

References 43

Chapter 3 Novel Experimentally Calibrated Multiphase TCAD Model for Cobalt Germanide Growth 46

1- Introduction 46

2- The Model 48

3- Simulation Results 51

4- Conclusion 56

References 56

Chapter 4 Cobalt Germanide Contacts: Growth Reaction, Phase Formation Models, and Electrical Properties 59

1- Evolution of Contacts to Semiconductor Devices: 62

1.1- Aluminum as a Contact [1]: 62

1.2- Self-Aligned Silicide Barriers: 64

1.3- Paradigm Shift to Interface Contact Resistivity Criterion: 72

2- Rise of Germanium and Need for Germanide Contacts: 74

3- Fundamental Physical Properties of Cobalt Germanides 78

4- Models for Phase Formation Sequence 84

4.1- Nucleation of a New Phase [67]: 84

4.2- Effective Heat of Formation Model 86

4.3- Walser-Bené Rule [102] 88

4.4- Cobalt Germanidation Growth Kinetics Model [106] 89

5- Experimental Phase Formation Sequence of Cobalt Germanides 92

6- Electrical properties of the contact 107

6.1- Ohmic and Schottky Properties of the Metal-Germanium contact 109
6.2- Fermi Level Pinning Mechanisms: 115
6.3- Fermi Level Depinning 118
6.4- Effect of metal crystallinity on Schottky Barrier Height 123
7- Challenges and Future Trends 125
References: 127
Chapter 5 Conclusion and Future Work 141
1- Summary of Contributions 143
2- Limitations and Future Work 145
References 147
Appendix A: TCAD Model Code 151

Declaration of Academic Achievement

The three papers presented in chapters 2, 3, and 4 are coauthored papers. I am the first author on all three papers. The experiments presented in chapter 2 are designed by me as well as the flow of the paper and the experimental results were all analyzed by me. The coauthors helped me in conducting some experiments and understanding the XRD data. I also developed and formulated the model presented in chapter 4. The coauthors helped me in conducting some simulations. The help I received from other coauthors, other than the supervisor Dr. Haddara, in the review paper presented in chapter 4 was summarizing some papers from those referenced that I requested them to read and summarize. Other than that, the paper's flow is designed and the paper is written by me and reviewed by Dr. Haddara.

Chapter 1

Introduction

Contact formation is an important step in backend process. Backend process refers to fabricating interconnect layers, contacts, vias, and dielectric layers that wire active devices into specific circuit configuration. Circuit delays associated with backend components have become an obstacle in obtaining faster integrated circuits in recent years. Those circuit delays have to be reduced to benefit from the fast active devices obtained by scaled technologies. Thus, research into improving backend technology has gained momentum in recent years. This research has been motivated by the continuous scaling down and improvement of active devices. This trend is expected to continue in the foreseeable future.

There are two main types of interconnects: local and global. Local interconnects are the lowest level of interconnects. They connect the electrodes of the same devices or neighboring devices. Those electrodes are in contact with sources, drains, gates, and bodies in MOS technology and they are in contact with bases, emitters, and collectors in bipolar technology. Global interconnects are all those interconnects above the lowest level local interconnects. They often connect different devices which might be far apart on the chip or they connect different parts of the chips. Low resistivity is a requirement in global interconnects since they extend for long distances. Local interconnects can tolerate higher resistivities but they should also tolerate higher processing temperatures as they are formed earlier in the process. Polysilicon electrodes and silicided or germanided electrodes can act as local interconnects.

The connection between the local interconnect and the active device has to be made through an ohmic contact. The choice of the contact material has to be made in such a way as to ensure that the contact resistivity is as low as possible. The contact resistivity contributes directly to the RC time delay associated with a signal propagating through the device. The low resistivity of the contact will ensure a shorter time delay. In state-of-the-art devices the contact area is shrinking due to the shrinkage of the device dimensions. The resistance of the contact is inversely

proportional to its area. The smaller contact area will result in a higher resistance and, consequently, a higher time delay. This, again, emphasizes the importance of having a low resistivity material for the contact.

In this chapter, the general theme and objectives of this work are described followed by an outline describing the organization of this sandwich thesis.

1- Motivation

Germanium was the key substrate material in the early days of the semiconductor transistor as it had the best crystalline quality at the time [1]. However, Si soon replaced Ge as the material of choice [2] and has dominated the microelectronics industry for the last five decades. This silicon domination is mainly for two reasons. First, the high quality and stable oxide that forms as a dielectric on top of silicon. By contrast, GeO_2 is a low quality unstable oxide that does not provide enough passivation of the surface. Second, the enormous amount of research and investment that has been made in silicon as a platform for MOSFET development. In recent years, two major changes have emerged in the industry. First, is the incorporation of high percentages of Ge in MOSFET devices to benefit from stress engineering in improving the mobility of carriers in p-type FET devices. Second is the replacement of thick silicon dioxide with high-k dielectrics to match the requirements of scaling down the device dimensions. This eliminates one of the major advantages in using silicon and opens the door for new materials in the microelectronics industry.

Pure germanium is a strong candidate to be included in the industry given its higher carrier mobilities and its relative compatibility with the silicon process [3]. In addition, the instability of the germanium oxide that was seen as a disadvantage in early days of semiconductors becomes an advantage when using high-k dielectrics: for the same process conditions, the interfacial oxide thickness is significantly lower in case of a Ge substrate compared with Si [4]. This makes a direct interface between the high-k dielectric and Ge more easily manufacturable compared to Si [5, 6], giving Ge an advantage in effective oxide thickness scalability. High concentrations of germanium are included in silicon FinFETs [7], the current workhorse in the advanced CMOS industry. The high concentration of germanium improves carrier mobility due to strain and bandgap engineering. CMOS devices in the future industry

nodes, 7nm and beyond, do not seem to be possible without using a higher mobility material in the fin. Germanium again is a strong candidate for the future nodes of the FinFETs.

There are a number of major obstacles to overcome in the development of Ge FETs. One of those obstacles is the passivation of the Ge-dielectric interface which does not seem to be possible using conventional silicon techniques. A second problem is the low I_{on}/I_{off} ratio of Ge MOSFETs. Ge devices suffer from high leakage current across p-n junctions due to the small bandgap of Ge (~0.67eV at room temperature compared with 1.1eV for Si) [8]. This leakage current dominates the off-state drain current of the transistors. In addition, it is difficult to obtain high active dopant concentration, especially in source and drain regions where such concentrations are needed [5]. The solubility of dopants in Ge is relatively low compared to Si [8] and dopants suffer from incomplete ionization. Small bandgap and lower active dopant concentrations in S/D regions compared to Si result in lower I_{on}/I_{off} ratio for Ge compared to Si devices. Metallic S/D regions have been proposed to overcome this issue [9]. A third problem is the lack of a complete understanding of the fundamental properties of germanium. For example, there is no agreement on the equilibrium concentration and diffusivities of vacancies in germanium. The development of many device and process models is based on those fundamental parameters. A fourth obstacle is the lack of understanding of the contact formation process and the quality of those contacts in Ge based technologies. Limitations on high active dopant concentration restrict the heavy doping technique used for lowering the contact resistivity which is effective in the case of silicides on Si. Fermi Level Pinning (FLP), which will be discussed in Chapter 4, poses another problem in controlling the metal-Ge contact.

Parasitic source/drain resistance is becoming a significant limiting factor in the scaling down of CMOS devices. This resistance is composed of four components [10]: 1- R_{ov}: source/drain extension to gate resistance, 2- R_{ext}: S/D extension resistance, 3- R_{dp}: deep S/D resistance, and 4- R_{csd}: silicide-diffusion contact resistance. Sub-100 nm short channel ultra-shallow S/D modelling of the series resistance reveals that the contact resistance (Rcsd) is the dominant contributor to the series resistance as the devices are scaled down as shown in figure 1.

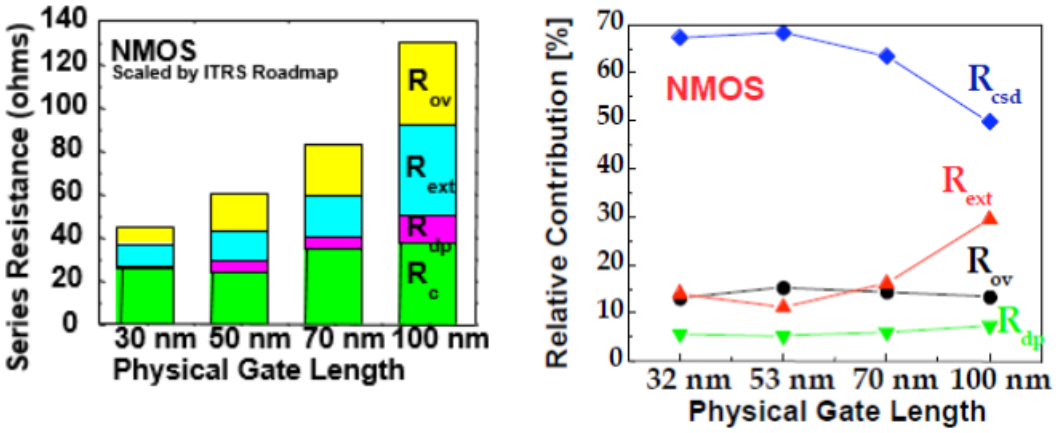

Figure 1: The contact resistance is the dominant factor to the series resistance as the device is scaled down [11]

Figure 1 emphasizes the importance of high quality low resistivity contacts in advanced CMOS technology. FLP has to be minimized or eliminated to minimize contact resistivity. The contact resistivity has to be in the range of 10^{-9} Ω.cm^2 to be compatible with the recent nodes in advanced CMOS industry. In addition to FLP, multiple processing issues exist in case of metal germanides. Various germanides and germanidation processes have to be understood and evaluated to gain better understanding of the contact formation process for germanium transistors. Melting points and Gibbs' free energy of germanide phases are lower than their silicide counterparts [12]. This indicates that germanides are less stable than silicides. They tend to react with third party species easier than silicides do. The low melting point also indicates that germanides have high reactive diffusion in them than the corresponding silicide phases [12]. Consequently, germanides form at lower temperatures compared to the corresponding silicide phases.

Gaudet et al [13] surveyed 20 different transition metal germanides for the use as contacts in CMOS technology. A first group of metals (Ti, Zr, Hf, V, Nb, and Ta) react with Ge at very high temperatures and are easily oxidized. A second group of metals (Cr, Mo, Mn, Re, Rh, Ru, Ir, and W) do not form low resistivity germanide phases. The third group of metals (Fe, Co, Ni, Pd, Pt, and Cu) formed low resistivity germanide phases at relatively low temperatures (150-360°C) and are therefore promising for further investigation and development. The lowest resistivities corresponded to NiGe and PdGe (22 and 30Ωcm, respectively).

Despite its low resistivity, PdGe has processing difficulties that are likely to limit its usage as a contact. Extra palladium has to be removed using aqua regia after germanidation [14]. Pure aqua regia etches Ge at 290 nm/min. This fast rate can be a killer in CMOS process if Ge is exposed. On the other hand, acids compatible with Ge processing like HCl, HNO_3, and H_2SO_4 can be used for etching Ni [14]. Another obstacle in the use of Pd is its high cost compared to other metals commonly used in the semiconductor industry [15].

Nickel germanides suffer from overgrowth onto neighboring oxide isolation [15]. Nickel germanides grow on the neighboring silicon dioxide isolation leaving behind voids in germanium due to germanium diffusion. Germanium is the diffusing species in the germanidation reaction with nickel [15]. This phenomenon seems to have similar root cause as the excessive nickel silicidation issue referred to in the previous section. The solution proposed by the researchers was to perform a two-step process with two low temperature RTAs (<350°C) similar to the solution proposed for excessive nickel silicidation. However, this overgrowth issue imposes a very restrictive thermal budget during back-end-of-the-line (BEoL) processes which can be impractical in a mass production setup. In addition, the two-step RTA does not completely solve the voids problem despite reducing it to a great extent.

Copper germanide was another candidate suggested by Gaudet et al. [13]. However, copper is the dominant contaminant in germanium for temperatures above 500°C [4]. This is mainly attributed to the high diffusivity of copper in germanium. Given its destructive effect on germanium devices due to deep level traps in the bandgap, copper is unlikely to be used for the purpose of creating contact on germanium. Fe and Co, on the other hand, have shown no midgap traps for germanidation temperatures up to 500°C [16]. In addition, cobalt related traps are mitigated using a long time anneal step at 700°C [17].

Platinum germanide contacts have been shown to be highly thermally stable over a wide range of temperatures (room temperature to 600°C) compared to Pd, Ni, and Co germanides [18]. It was also shown that platinum germanides contacts are the highest quality, with low reverse currents on the order of 10^{-6}-10^{-5} A. The issue with platinum silicide was its low temperature reaction with the metal on top. No complete designs have yet been reported in the literature for the stack of the platinum germanide contacts to CMOS devices. As for iron germanides,

several studies have been done [19-22] but none have investigated iron germanides' use as contacts for CMOS devices.

Despite the issues associated with titanium germanides, they are the preferred option given their compatibility with titanium silicides that the industry returned to in recent years [23-25]. Contact resistivity as low as $3x10^{-9}$ $\Omega.cm^2$ was obtained on p-Ge wafer with boron concentration of $1x10^{21}cm^{-3}$ [24]. As discussed earlier, such high doping concentration might not be feasible for some applications. The onset of ohmic behavior was a boron concentration of $10^{20}cm^{-3}$. The specific titanium germanide phase obtained in the experiment and used for such application was not reported [24]. Ab-initio simulations showed that germanide phase affects the Schottky barrier height and, therefore, the contact resistivity. Ohmic contact was formed on n-Ge with a phosphorus doping concentration of $2x10^{19}cm^{-3}$ after RTA of deposited Ti at 600°C [25]. This process step resulted in C54 titanium germanide phase with a contact resistivity as low as $1.5x10^{-5}$ $\Omega.cm^2$. Further phosphorus implant after germanidation reduced contact resistivity to $3.6x10^{-6}$ $\Omega.cm^2$. The range of the contact resistivity for titanium germanide on n-type germanium is, therefore, much higher than that on p-type germanium. Another issue was the degradation of the interface quality between titanium germanide and Ge at high temperatures [23]. This issue will be discussed in section 6 of chapter 4. No interface degradation was observed in Chou et al.'s study [25]. This might be attributed to the different annealing time or dopant concentration. A more focused study is necessary to explain the cause of the interface degradation. Titanium as a metal, rather than its germanide, has also been used as a contact material for p-type germanium [26] and it gives a reasonable contact resistance of $1.1x10^{-8}$ $\Omega.cm^2$. Titanium was also able to clean the germanium interface of oxygen residues due to the high oxygen solubility and diffusivity in germanium. On the other hand, the sheet resistance of titanium cannot be reduced and the low thermal budget necessary to avoid germanidation could impose a restriction on the succeeding process steps.

The study of cobalt germanides as contacts is motivated by the compatibility with silicon process and the expected similarities between the behavior of cobalt silicides and cobalt germanides. Nowadays, silicon germanium alloys are commonly used in the advanced CMOS industry. It is expected that both pure germanium and pure silicon will be part of future CMOS devices. Having a metal that creates barrier layers compatible with both silicon and germanium would simplify the barrier-creation process. Tungsten, titanium, cobalt, and nickel are the most common

metals used in silicides. Cobalt, among those four, is the most suitable metal for creating both silicide and germanide contacts given the aforementioned issues with tungsten, titanium, and nickel germanides. In addition, it has been shown that cobalt germanides form low resistivity phases at lower reaction temperatures and are more resistive to oxidation than titanium germanides [13]. Low resistivity cobalt germanide phase can be formed using solid-state reaction at temperatures as low as 425°C [27]. This temperature range is compatible with Middle of Line (MOL) process and is lower than the formation temperature of the low resistivity titanium germanide phase, giving cobalt germanides a processing advantage. The interface contact resistivity of cobalt germanides is expected to be better than that of titanium germanides given the expected epitaxial nature of cobalt germanides similar to cobalt silicides. Also, cobalt silicides don't have the excessive silicidation problem that nickel silicides have and similar behavior is expected for cobalt germanides. Therefore of the four elements, cobalt seems to be the best choice of contact for pure germanium devices. Cobalt germanides also form high quality ohmic contacts to wide bandgap semiconductors like GaAs [27, 28]. Cobalt germanides nanostructures are also promising structures for memory applications given their superior memory characteristics [29]. Finally, cobalt diffusion in germanium was used to probe fundamental properties of the material like point defect properties [30], the activation energy, capture cross section for holes and electrons and trap concentration profiles [31, 32]. Experiments to probe fundamental properties of germanium could be designed more efficiently if the cobalt germanidation process is well understood as well as cobalt in-diffusion during germanidation. In particular, cobalt germanidation at temperature 600°C and higher has been identified as an easy method to introduce substitutional Co into n-type Ge [33].

2- Objective and Outline

The main objective of this thesis is to investigate the optimum process design to obtain high quality low resistivity cobalt germanide contact for germanium based devices. A good quality contact would be a single phase cobalt germanide to minimize the variation in the resistivity. The first step in designing a good quality contact would be to understand the phases of cobalt germanides and the temperature ranges for formation of each of those phases. We observed theoretical and experimental controversy in the literature regarding the first phase to form during solid state anneal of Co deposited on Ge. The main thermodynamic phase formation model, effective heat of formation

(EHF), identifies CoGe as the phase with lowest EHF but this phase is non-congruent. The only congruent phase is Co_5Ge_3. The model suggests that Co_5Ge_3 would then be the first phase to form since non-congruent phases are usually skipped. The model was 80% successful to predict the first phase to form. Therefore, it cannot confirm with certainty that Co_5Ge_3 is the first phase to form. Temperature ramp-up experiments, on the other hand, show the first phase to form to be CoGe. Solid-state anneal experiment showed the first phase to form to be Co_5Ge_3. We conducted a set of long time low temperature anneal experiments with in-situ phase monitoring to investigate the first phase to form and were able to identify it to be Co_5Ge_3, conclusively settling the controversy regarding the first phase to form. The main difference between our experiments and previously conducted experiments is the in-situ XRD monitoring of the phase forming during the reaction. Our experiments are discussed in chapter 2. An important outcome of the experiments was that both Co_5Ge_3 and CoGe were partially epitaxial phases. This semi-epitaxial growth makes these phases potentially good candidates for low-temperature high quality contacts. The low thermal budget is very appealing for the process designer since it is compatible with the middle of line and back end of line processes to follow the contact formation.

The experimental results presented in chapter 2 contributed to our understanding of the cobalt germanidation process leading to the development of the first multiphase predictive physics-based mathematical model for cobalt germanide formation. The model is presented in chapter 3. It is capable of predicting the forming phase among the four phases of cobalt germanides: Co_5Ge_3, CoGe, Co_5Ge_7, $CoGe_2$, the composition of the germanide in case of mixed phase experiment, and the thickness of the forming germanide layer. The inputs to the model are germanidation time, temperature, and ambient. The goal of the model is to give the designer the capability to design a high quality contact by using different process parameters as inputs to a simulation and concluding the phase and the thickness of the cobalt germanide contact from the simulation. The model was implemented in Sentaurus Process (SProcess), a technology computer aided design (TCAD) tool specialized in semiconductor process physics. The SProcess implementation code is shown in appendix A in the end of this thesis. The model has been calibrated to experimental results reported in the literature as well as our own data. This model can help in the design of single-phase low-resistivity cobalt germanide contacts. The model can be generalized and calibrated for any multiphase solid state reaction binary system.

The experiments selected to calibrate the model presented in chapter 3 were selected to utilize solid-state anneal at a constant temperature where Co was sputtered on Ge. Other experimental setups result in different germanide phases or different quality of the germanide for the same time, temperature, and ambient conditions. It became clear that other factors contribute to the resulting phase and the quality of the germanide. To understand those factors the experimental results for cobalt germanidation were extensively reviewed in a survey presented in chapter 4. Chapter 4, first, covers the evolution history of the contacts to semiconductor devices followed by covering the current role of germanium in the industry. Fundamental physical properties of cobalt germanides are, then, detailed and the current phase prediction models are reviewed. Next, the survey on experimental data is presented. Based on the survey, we concluded that there are mainly three different methods that have been used for cobalt germanidation. Reactive deposition, the first method, yields interfacial germanides at temperatures as low as room temperature. The thickness of such layer is not easily controlled and the slow deposition methods used are impractical for industrial mass production. In addition, mixed phases have been observed even at temperatures as high as 650°C. Temperature ramp-up experiments result in high formation temperatures compared to solid state anneal at a constant temperature. Therefore, solid state anneal at a constant temperature seems to be the best option for contact formation. The effect of other factors on the phase and the quality of the germanide was evaluated including the crystallinity of Ge, mechanical strain, and the pretreatment of the surface.

The main practical factor that determines the quality of the germanide is its electrical properties. It was important, next, to understand the electrical properties of cobalt germanide contacts and other factors contributing to the quality of the contact other than the ones enlisted in section 5 in chapter 4. Section 6 in chapter 4 aims to evaluate the electrical interface resistivity of various cobalt germanide phases and the parameters controlling that resistivity. The available data in the literature on Schottky and ohmic properties of cobalt germanide contacts is reviewed in that section. The role of germanium crystal orientation in ohmic and Schottky properties of the contact is analyzed. We concluded that FLP plays a role only on one of four interfaces, that is, the germanide/(100) n-Ge interface. The role of FLP is minimal on other interfaces including p-type Ge interfaces and germanide/(111) n-Ge interface. Schottky barrier heights for cobalt and cobalt germanide contacts reported in the literature were surveyed. The factors contributing to the variation in SBH were identified including the crystallinity of the germanide, the

deposition technique used for Co, the doping concentration in Ge, and the surface pretreatment. Epitaxial cobalt germanides are expected to reduce the SBH significantly. We identified the main technique used to grow such epitaxial germanides which is high temperature Co deposition followed by a constant temperature anneal. The thesis is, finally, concluded with chapter 5 which summarizes the contributions made in this thesis and gives suggestions for future work.

References:

[1] Bardeen, J., & Brattain, W. H., *Phys. Rev.*, *74*(2), 230–231 (1948).

[2] Tanenbaum, Morris, Bell Labs Notebook No. 25505, page 30 (January 26, 1954).

[3] Schuegraf, K., Abraham, M. C., Brand, A., Naik, M., & Thakur, R., *IEEE J. Electron Devices Soc.*, *1*(3), 66–75 (2013).

[4] C. Claeys, E. Simoen, *Germanium-Based Technologies: From Materials to Devices*, (Elsevier, 2007), pp. 246–261.

[5] Chui, C. O., Gopalakrishnan, K., Griffin, P. B., Plummer, J. D., & Saraswat, K. C., *Appl. Phys. Lett.*, *83*(16), 3275–3277 (2003).

[6] Kita, K., Kyuno, K., & Toriumi, A., *Appl. Phys. Lett.*, *85*(1), 52–54 (2004).

[7] Huang, X., Lee, W.-C., Kuo, C., Hisamoto, D., Chang, L., Kedzierski, J., et al., In *Int. Electron Devices Meeting 1999. Technical Digest (IEDM)*, (pp. 67–70) (1999).

[8] Chui, C. O., Kulig, L., Moran, J., Tsai, W., & Saraswat, K. C., *Appl. Phys. Lett.*, *87*(9), 091909 (2005).

[9] Maeda, T., Ikeda, K., Nakaharai, S., Tezuka, T., Sugiyama, N., Moriyama, Y., & Takagi, S., *IEEE Electron Device Lett.*, *26*(2), 102–104 (2005).

[10] S.-D. Kim, C.-M. Park, and J. Woo, "Advanced Model and Analysis of Series Resistance for CMOS Scaling Into Nanometer Regime – Part II: Quantitative Analysis," IEEE Transactions on Electron Devices, V. 49, N. 3, Mar. 2002.

[11] http://web.stanford.edu/class/ee311/NOTES/Shallow%20Junctions%20Slides.pdf

[12] Zhang, S.-L., & Östling, M., *Crit. Rev. Solid State Mater. Sci.*, *28*(1), 1–129 (2003).

[13] Gaudet, S., Detavernier, C., Kellock, A. J., Desjardins, P., & Lavoie, C., *J. Vac. Sci. Technol. A*, *24*(3), 474–485 (2006).

[14] Brunco, D. P., Jaeger, B. D., Eneman, G., Mitard, J., Hellings, G., Satta, A., et al., *J. Electrochem. Soc.*, *155*(7), H552–H561 (2008).

[15] Brunco, D. P., Opsomer, K., Jaeger, B. D., Winderickx, G., Verheyden, K., & Meuris, M., *Electrochem. Solid State Lett.*, *11*(2), H39–H41 (2008).

[16] E. Simoen, K. Opsomer, C. Claeys, K. Maex, C. Detavernier, R.L. Van Meirhaeghe, P. Clauws, *Solid State Phenom.*, Vols. 131-133, pp. 47-52 (2008).

[17] L. Lajaunie, M.-L. David, K. Opsomer, E. Simoen, C. Claeys, J. F. Barbot, *Solid State Phenom.*, Vols. 131-133, pp. 107-112 (2008).

[18] Chawanda, A., Nyamhere, C., Auret, F. D., Mtangi, W., Diale, M., & Nel, J. M., *Phys. Status Solidi C*, *7*(2), 248–251 (2010).

[19] Jaafar, R., Nehme, Y., Berling, D., Bubendorff, J. L., Mehdaoui, A., Pirri, C., Garreau, G., Uhlaq-Bouillet, C., Appl. Phys. Lett., *93*(3), 033114 (2008).

[20] Jaafar, R., Berling, D., Sébilleau, D., & Garreau, G., *Phys. Rev. B*, *81*(15), 155423 (2010).

[21] Yoon, H., Lee, A. T., Choi, E.-A., Seo, K., Bagkar, N., Cho, J., Jo, Y., Chang, K. J., Kim, B., *J. Am. Chem. Soc.*, *132*(49), 17447–17451 (2010).

[22] Adelson, E., & Austin, A. E., *J. Phys. Chem. Solids*, 26(12), 1795–1804 (1965).

[23] Janardhanam, V., Kim, J.-S., Moon, K.-W., Ahn, K.-S., & Choi, C.-J., *Microelectron. Eng.*, *89*, 10–14 (2012).

[24] Dixit, H., Niu, C., Raymond, M., Kamineni, V., Pandey, R. K., Konar, A., et al., *IEEE Trans. Electron Devices*, *64*(9), 3775–3780 (2017).

[25] Chou, C., Chang, H., & Wu, Y., *IEEE Electron Device Lett.*, *39*(1), 91–94 (2018).

[26] Yu, H., Schaekers, M., Schram, T., Aderhold, W., Mayur, A. J., Mitard, J., et al. D., *IEEE Electron Device Lett.*, *37*(4), 482–485 (2016).

[27] Koltin, E., & Eizenberg, M., *J. Appl. Phys.*, *71*(9), 4604–4611 (1992).

[28] Genut, M., & Eizenberg, M., *J. Appl. Phys.*, *68*(5), 2146–2157 (1990).

[29] Joo, B. S., Kim, H., Jang, S., Han, D., & Han, M., *J. Phys. Chem. Solids*, *119*, 309–313 (2018).

[30] Stolwijk, N. A., & Lerner, L., *J. Appl. Phys.*, *110*(3), 033526 (2011).

[31] Opsomer, K., Simoen, E., Claeys, C., Maex, K., Detavernier, C., Van Meirhaeghe, R. L., Forment, S., Clauws, P., *Mater. Sci. Semicond. Process.*, *9*(4), 554–558 (2006).

[32] Simoen, E., Opsomer, K., Claeys, C., Maex, K., Detavernier, C., Van Meirhaeghe, R. L., Forment, S., Clauws, P., *Appl. Phys. Lett.*, *88*(18), 183506 (2006).

[33] Simoen, E., Opsomer, K., Claeys, C., Maex, K., Detavernier, C., Van Meirhaeghe, R. L., & Clauws, P., *J. Appl. Phys.*, *104*(2), 023705 (2008).

Chapter 2

First Phase to form during Cobalt Germanidation

Mohamed A. Rabie, Souzan Mirza, Victoria Jarvis, and Yaser Haddara, "First Phase to form during Cobalt Germanidation," J. Appl. Phys. 121, 145304 (2017)

First phase to form during cobalt germanidation

Mohamed A. Rabie,[1] Souzan Mirza,[2] Victoria Jarvis,[3] and Yaser M. Haddara[2]

[1]Global Foundries, 400 Stone Break Rd Extension, Malta, NY 12020 USA.

[2]Department of Electrical and Computer Engineering, McMaster University, 1280 Main St West, Hamilton ON, L8S 4L8 CANADA.
[3]McMaster Analytic X-Ray Diffraction Facility, Department of Chemistry, McMaster University, 1280 Main St West, Hamilton ON, L8S 4L8 CANADA.

Abstract

The first systematic study for the first phase to form during cobalt germanidation was conducted. Hexagonal β-Co_5Ge_3 was the first phase to form in case of cobalt germanidation on (100) Ge. This phase formed at a temperature as low as 227°C. Monoclinic CoGe was shown experimentally to be the second phase to form at the same temperature. Our results are contrary to previous reports suggesting monoclinic CoGe to be the first phase to form. This is mainly due to the experimental setup that was designed to detect all forming phases: in-situ XRD monitoring at a constant low temperature long time anneals of 24-48 hours. We also report for the first time that both β-Co_5Ge_3 and monoclinic CoGe phases that formed during cobalt germanidation were highly ordered partial epitaxial crystal orientations.

1- Introduction

Silicon (Si) has been the dominant material in the semiconductor industry for decades. As scaling down of CMOS devices continued, Si devices and processes approached fundamental physical limits. One of the major limits was the thickness of silicon dioxide gate dielectric, which had to be scaled down to a few monolayers to cope with the gate capacitance and drive current requirements of the shrinking device. This resulted in process integration problems due to dopant diffusion across the oxide as well as device issues such as the destructive tunneling current into the gate metal.[1] Two innovations extended the life of the Si CMOS industry. The first was the introduction of the FinFET where geometry of the MOS gate is a fin-like shape instead of the traditional planar gate,[2] which permitted better gate control of the channel. The second innovation was the introduction of the silicon germanium (SiGe) alloy to enhance channel mobility by engineering the bandgap and the strain.[3] Germanium (Ge) is also compatible with the Si process given its similar crystal lattice and dimension. As scaling down continues, the industry is considering a pure Ge channel in CMOS devices.[4] To successfully develop Ge-based FETs, research has to overcome a number of obstacles, including passivation of the Ge-dielectric interface, high leakage current across Ge p-n junctions, incomplete understanding of the fundamental properties of Ge, and fabrication of high quality contacts in Ge-based technologies.[3]

The need for high quality contacts in Ge-based devices is the primary motivation for the study of cobalt germanidation. Gaudet et al.[5] surveyed 20 different transition metal germanides for use as contacts in CMOS technology. The authors found six metals that can form low resistivity germanide phases at low temperatures (150-360°C): iron (Fe), cobalt (Co), nickel (Ni), palladium (Pd), platinum (Pt), and copper (Cu). Of these, only Ni and Co are compatible with Si process technology. The use of SiGe in CMOS technology is now standard. It is expected that both Ge and Si will be part of future CMOS devices. Having a metal that creates contact layers compatible with both Si and Ge would simplify the contact-creation process. Of the two viable candidates, nickel is not ideal because it has been observed that nickel germanides overgrow neighboring oxide isolation, leaving behind voids in Ge due to Ge diffusion since Ge is the diffusing species in the germanidation reaction with nickel.[6] This phenomenon seems to have a similar root cause as the excessive nickel silicidation.[7] The solution proposed by Brunco et al.[6] was to perform a two-step low temperature RTA procedure (<350°C), similar to the solution proposed for excessive nickel

silicidation. This has the drawback that it imposes a very restrictive thermal budget during the Back End of Line (BEoL) process which can be impractical in a mass production setup. Additionally, the two-step RTA doesn't eliminate voids created in the Ge substrate, despite reducing them to a great extent.

The other viable transition metal that Gaudet et al. identified is Co. Multiple phases have been identified for cobalt germanides[8] including: Co_5Ge_3, CoGe, $CoGe_2$, Co_5Ge_7, Co_5Ge_2, and Co_3Ge. The contact resistance is composed of two components in series: a) the equivalent resistance of the germanide-germanium interface which is typically dependent on the Schottky Barrier Height (SBH) and the active dopant concentration at the germanide/Ge interface and b) the metal resistance dependent on resistivity, thickness, and area of the contact.[8] Both components are important; however, the first component is dominant in state-of-the-art silicon devices. SBH has been observed to be independent of the metal in contact with n-type Ge due to Fermi level pinning.[9] Conversely, metal in contact with p-type Ge exhibits ohmic behavior.[9] The SBHs of different cobalt germanides/n-type Ge interfaces measured by Chawanda et al.[10] were close to each other in value as expected due to Fermi level pinning. Some researchers have already shown Fermi level depinning at the metal-Ge interface using careful design.[11,12] Historically, Fermi-level pinning was observed for metal-silicon interfaces.[13] However, with the very high quality interfaces currently produced in the industry, the current state of the art is that the SBH is highly dependent on the metal work function.[9] This is especially true for the source and drain of nano CMOS devices since the silicide is in direct contact with silicon. The contact resistance contribution from metal resistivity depends on the germanide phase. Resistivities of CoGe and $CoGe_2$ at room temperature have been reported to be 65.7 and 150 μΩ.cm, respectively.[14] This wide resistivity range emphasizes the importance of careful cobalt germanide contact design.

The temperature at which each of these phases forms also varies. It is important to understand the phase formation sequence in order to design a high quality, low resistivity cobalt germanide contact that forms at a temperature compatible with the semiconductor process. Cobalt germanidation has been the subject of a number of studies.[14-21] Different phases have been reported to form during cobalt germanidation including Co_5Ge_3, CoGe, $CoGe_2$, and Co_5Ge_7. Once the initial phase forms, the sequence of phases to appear for longer reaction times will be determined by the Co-Ge balance. Under Ge-rich conditions we will move to the right on the phase diagram,

whereas Co-rich conditions will drive the reaction to the left on the phase diagram. In this paper, we investigate the first phase to form at low temperature.

No germanide formation has been detected experimentally at or below 200°C.[15-17] This is true for both (100)Ge and (111)Ge and it is also true for atmospheric and low pressure. Interfacial reactions were found to start to occur between Co and (111)Ge at 220°C.[17] Hsieh et al.[17] reported weak x-ray diffraction (XRD) signals of a germanide after one hour anneal at 220°C in low pressure vacuum. The authors indicated that the forming phase likely matches monoclinic CoGe or β-Co_5Ge_3. The phase was not confirmed since the XRD signal was weak. Grzela et al.[16] observed the nucleation of ordered nanocrystals after annealing 4 monolayers of Co deposited on (100)Ge for one hour at 250°C. These ordered nanocrystals start to form islands of rectangular shape and grow at random places on the surface. In addition, the Ge terrace-structure morphology, which was initially visible, disappears after anneal. These results indicate the onset of Co-Ge reaction. However, the authors didn't analyze which cobalt germanide phase formed. Wittmer et al.[15] detected Co_2Ge, which was shown in a later phase diagram study[22] to be β-Co_5Ge_3, in their experiment performed at 250°C for 1-20 hours. However, Wittmer et al. did not perform in-situ XRD. The first germanide phase to form in the Co-Ge reaction has been shown to be monoclinic CoGe by in-situ XRD during temperature ramp-up.[5,18] The authors ramped up the temperature at a rate of 3°C/sec. Monoclinic CoGe formed at approximately 400°C in those ramp-up experiments. However, those experiments cannot confirm the first phase to form during constant temperature cobalt germanidation because the fast ramp-up rate may not allow the reaction to reach equilibrium.

We report the first experimental results for germanidation conducted for long-time constant temperature anneals with in-situ XRD monitoring. We executed a number of cobalt germanidation experiments at constant temperatures, as low as 94°C for periods as long as 48 hours, to determine the first phase to form. The temperatures were gradually increased from one experiment to another to determine the onset temperature for germanidation. This paper is comprised of four sections: this introduction, a description of the experimental procedure, results and discussion, and conclusions.

2- Experimental Procedure

Blanket Co films, nominally 30 nm thick, were deposited at room temperature by magnetron RF sputtering on (100)Ge. Prior to deposition, Ge orientation and purity were confirmed using XRD. Before deposition, Ge substrates were exposed to UV ozone for 15 minutes to grow a thin oxide layer. This oxide layer was etched using buffered HF (1:10) for 20 seconds to remove the oxide and any contamination on the wafer surface. Samples were rinsed in deionized water for 2 minutes. The base vacuum of the magnetron RF sputtering system was $7x10^{-6}$ Torr and the deposition parameters used were argon pressure of 2 mTorr at a flow rate of 10 sccm and 30 W RF power. The sample was rotated during deposition at a speed of 10 rpm and the substrate temperature was maintained at 22ºC during the 52 minute deposition. These parameters were calibrated on Si to deposit a 30 nm thick film. The thickness of the 30 nm thick Co film was confirmed using AFM and the uniformity by SEM. Additional analysis of the sample using EDS confirmed the presence of the Co film on top of Ge and SIMS confirmed the Co depth profile.

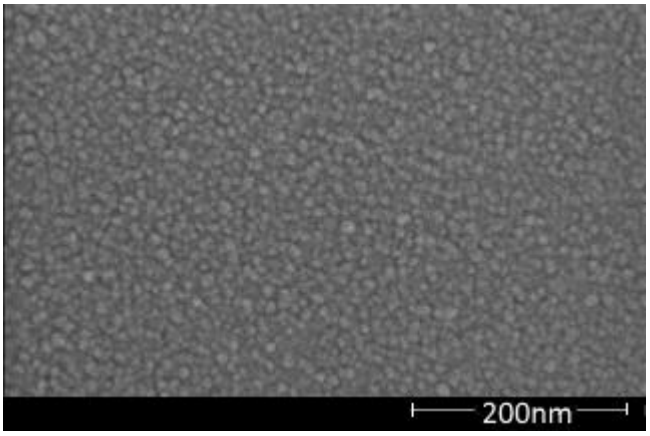

FIG. 1. SEM image of the top surface of the sample showing a uniform film.

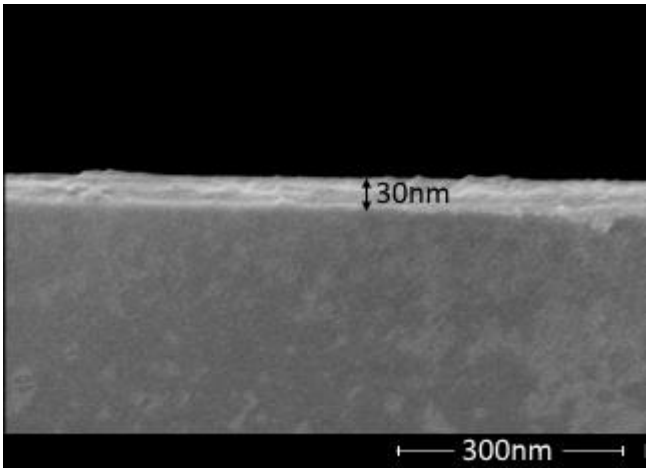

FIG. 2. SEM image of the cross section of the sample showing a 30 nm uniform film.

Native Ge oxide after HF cleaning is expected to be less than 1 nm.[23] Similarly, native Co oxide after sputtering and before XRD measurement is expected to be less than 2 nm.[24] For the samples used for the experiments at or below 184.5°C and at 457°C, SEM images showed that Co was deposited in the form of nanowhiskers. For samples used in anneals at 227°C the film was uniform.

The film after deposition did not show any signal with XRD and is likely amorphous. During the constant temperature anneals, the Co-Ge reaction was monitored in-situ using a Co-Kα XRD diffractometer. Scans were performed every 30 minutes. For later experiments scans were done every 2 hours to increase diffraction peak intensities thereby increasing the likelihood of detecting phase transformations. The anneal set-up required a PEEK (PolyEther Ether Ketone) vacuum dome mounted over the sample on a heating stage to maintain a vacuum pressure in the mTorr range. Temperature calibration was done by measuring the d-spacing, which is the distance between members of a family of parallel crystal planes, of a magnesium oxide powder as it was heated. MgO has a well-defined thermal expansion coefficient which can be used to determine the temperature by comparing the measured d-spacings against a reference table. In a separate temperature calibration experiment, a thermocouple was mounted on the heating stage under the dome, similar to the setup of the samples during the anneals, and temperature measurements were taken as the thermocouple was heated. This resulted in the final temperature calibration curve which was used to determine anneal temperatures for the germanidation experiments. The sample size was in the

range of 1cm^2 and the collimated XRD beam diameter was 0.5 mm at an incidence angle of 1°. The temperature was ramped up at 1°C/s and then held at a constant temperature for 24-48 hours. After the anneal, the sample was left to cool to room temperature in air. A post-anneal scan was performed on a Cu-Kα1 XRD diffractometer to detect if any germanide phases had formed. The post-anneal scans allowed us to measure sample diffraction with greater spatial coverage, a better signal-to-noise ratio and at higher angles due to the setup of the system which allowed the detector to move closer to the sample and the advantageous shorter wavelength of Cu radiation compared to Co radiation.

3- Results and Discussion

Table 1 summarizes our results. Experiments 1-3 and 6 were scanned in 30 minute intervals and experiments 4 and 5 were scanned in 2 hr intervals to improve phase detection. The samples annealed below 227°C showed no germanide formation in-situ or in post-anneal scans. Experiment 4 showed phase formation in in-situ scans which was later confirmed using texture analysis on the Cu-Kα1 source to be two growth orientations of β-Co_5Ge_3. Experiment 5 was conducted using the same experimental parameters as 4 but for longer time anneal and also resulted in the formation of β-Co_5Ge_3. Experiment 6 was annealed at 227°C in atmospheric conditions and resulted in the formation of four orthogonal orientations of monoclinic CoGe. Experiment 7 was annealed at 457°C for 1 minute and resulted in the formation of Co_5Ge_7.

TABLE I. Summary of the results of the anneal experiments.

Experiment Number	Temperature (°C)	Pressure	Time	Germanide Phase
1	94.3	Vacuum (mTorr range)	48 hours/30 min scans	No germanide
2	139.3	Vacuum (mTorr range)	36 hours/30 min scans	No germanide
3	184.5	Vacuum (mTorr range)	41 hours/30 min scans	No germanide
4	227	Vacuum (mTorr range)	24 hours/2 hr scans	β-Co_5Ge_3
5	227	Vacuum (mTorr range)	48 hours/2 hr scans	β-Co_5Ge_3
6	227	Atmospheric	48 hours/30 min scans	Monoclinic CoGe
7	457	Vacuum (mTorr range)	1 minute	Co_5Ge_7

Experiment 7 was carried out to test the detection capability of the XRD diffractometers. This experiment is similar in setup to that of Hseih et al.[17] Similar to their results, our measurements identified the formation of Co_5Ge_7. Figure 3 shows the XRD profile of the highly ordered Co_5Ge_7 phase detected in post-anneal scans.

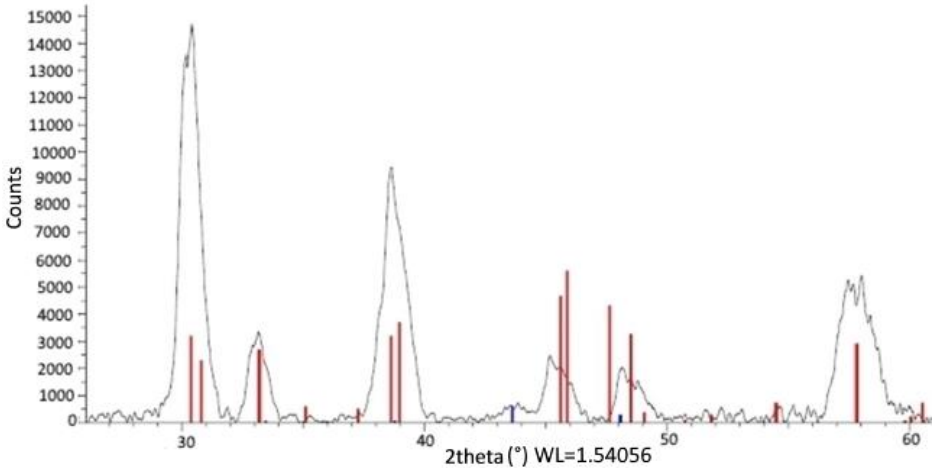

FIG. 3. Post-anneal XRD scans of experiment 7 (black trace) measured on Cu-Kα1 identify the phase as Co_5Ge_7 (red trace).

At low temperatures, we expected monoclinic CoGe to form based on previous reports.[5] To monitor for the formation of monoclinic CoGe, scans were recorded at $2\theta=52^{\circ}$ for experiment 1 and $2\theta=41^{\circ}$ for experiments 2 and 3. XRD profiles pre- and post-anneal did not show any changes indicative of phase formation which is consistent with previous work showing no germanide formation below $220^{\circ}C$.[17]

Subsequently, we performed multiple anneals at $227^{\circ}C$ in different ambient and for different durations. In experiment 6 the sample was annealed in air at atmospheric pressure for 48 hours and scanned every 30 minutes at $2\theta=48°$. Figure 4 reveals the growth of 2 peaks at 54° and 57° belonging to the same phase. These peaks correspond to shifted peaks of β-Co_5Ge_3 at 53° and 55° seen in the standard powder diffraction pattern in figure 5. They appear slightly shifted in 2θ possibly because the detector was not intercepting at the center of the diffraction spot and/or because the Co:Ge composition may vary from the database structure causing a unit cell shift. The two peaks were detected clearly after about 10 hours. After 20 hours the intensity of the peaks recede as the β-Co_5Ge_3 phase transforms to another phase. The new phase was confirmed in post-anneal scans to be monoclinic CoGe as shown in figure 6. Figure 7 shows the texture analysis of the resulting monoclinic CoGe phase. The film was highly ordered and exhibited a polycrystalline structure with four orthogonal orientations in which the principal axis was [-1 1 1]. Monoclinic CoGe phase has many peaks with a lot of overlap that would appear in 2θ XRD analysis. Three hkl peak poles were detected given their expected higher intensity in a 46°-48° XRD analysis: (-5 1 0), (-3 1 2), and (0 1 0).

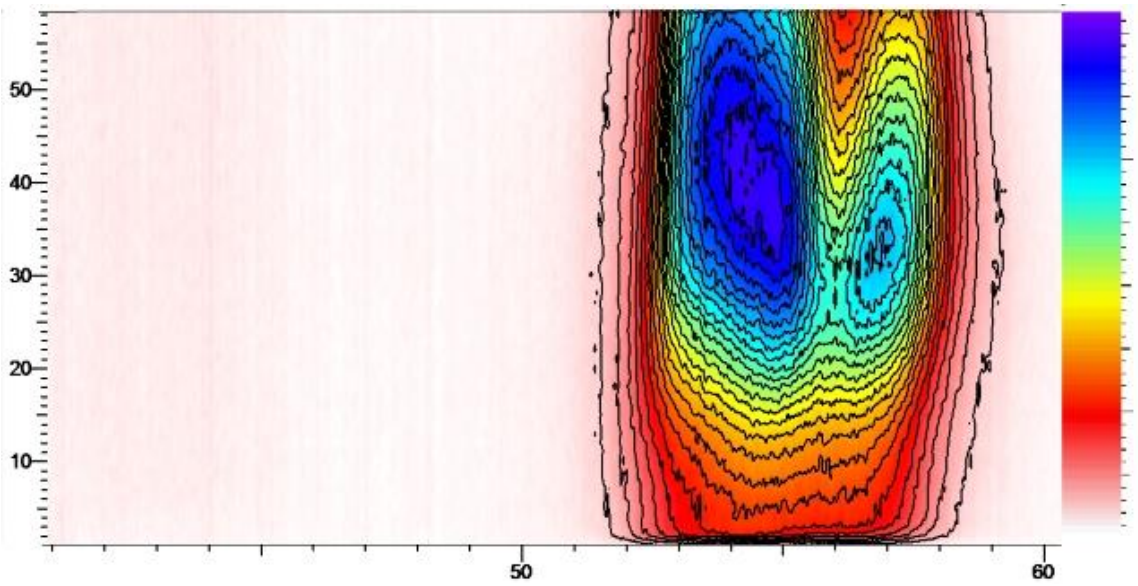

FIG. 4. The colour map of experiment 6 in-situ scans measured on Co-Kα displays 2θ values on the horizontal axis and 30 minute time intervals on the vertical axis. The colour map clearly depicts the growth on-set of peaks at 54° and 57° belonging to the β-Co_5Ge_3 phase after 10 hours. After 20 hours these peaks are consumed by the onset of phase transformation to monoclinic CoGe.

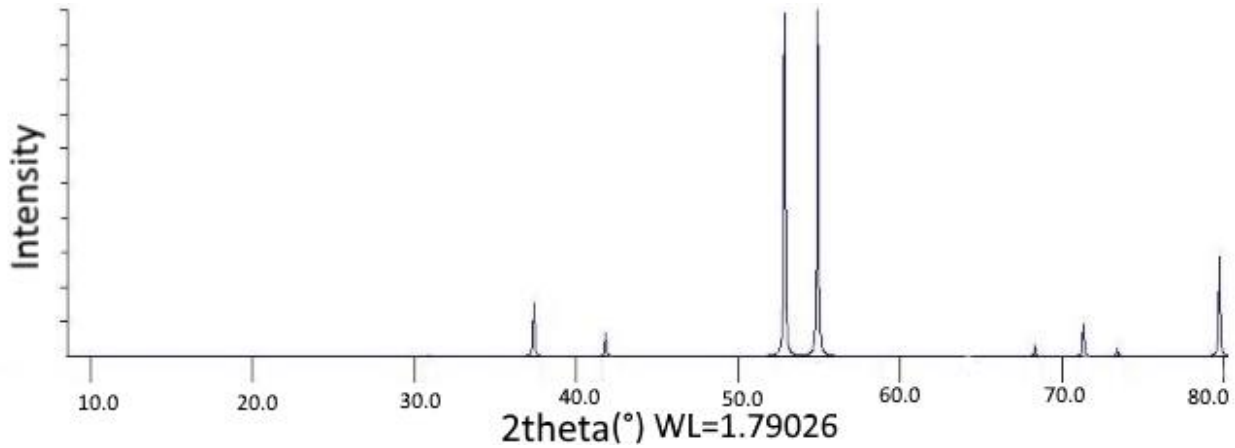

FIG. 5. Standard XRD profile of β-Co_5Ge_3 from ICSD (PDF 623425).

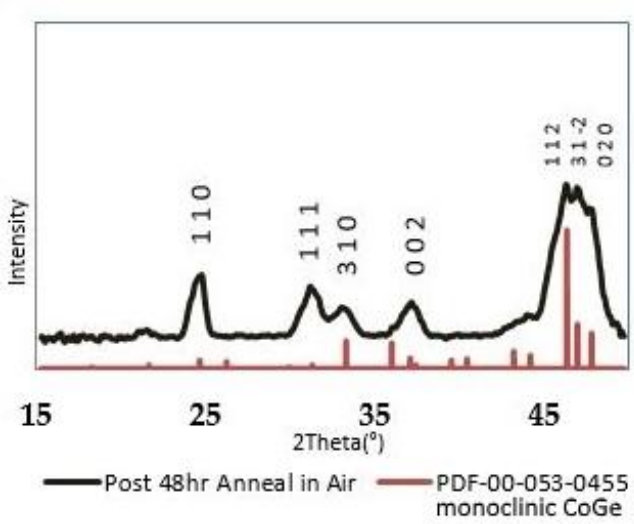

FIG. 6. Post-anneal 2θ texture analysis of experiment 6 measured on Cu-Kα1 (black) identified the phase as monoclinic CoGe (red).

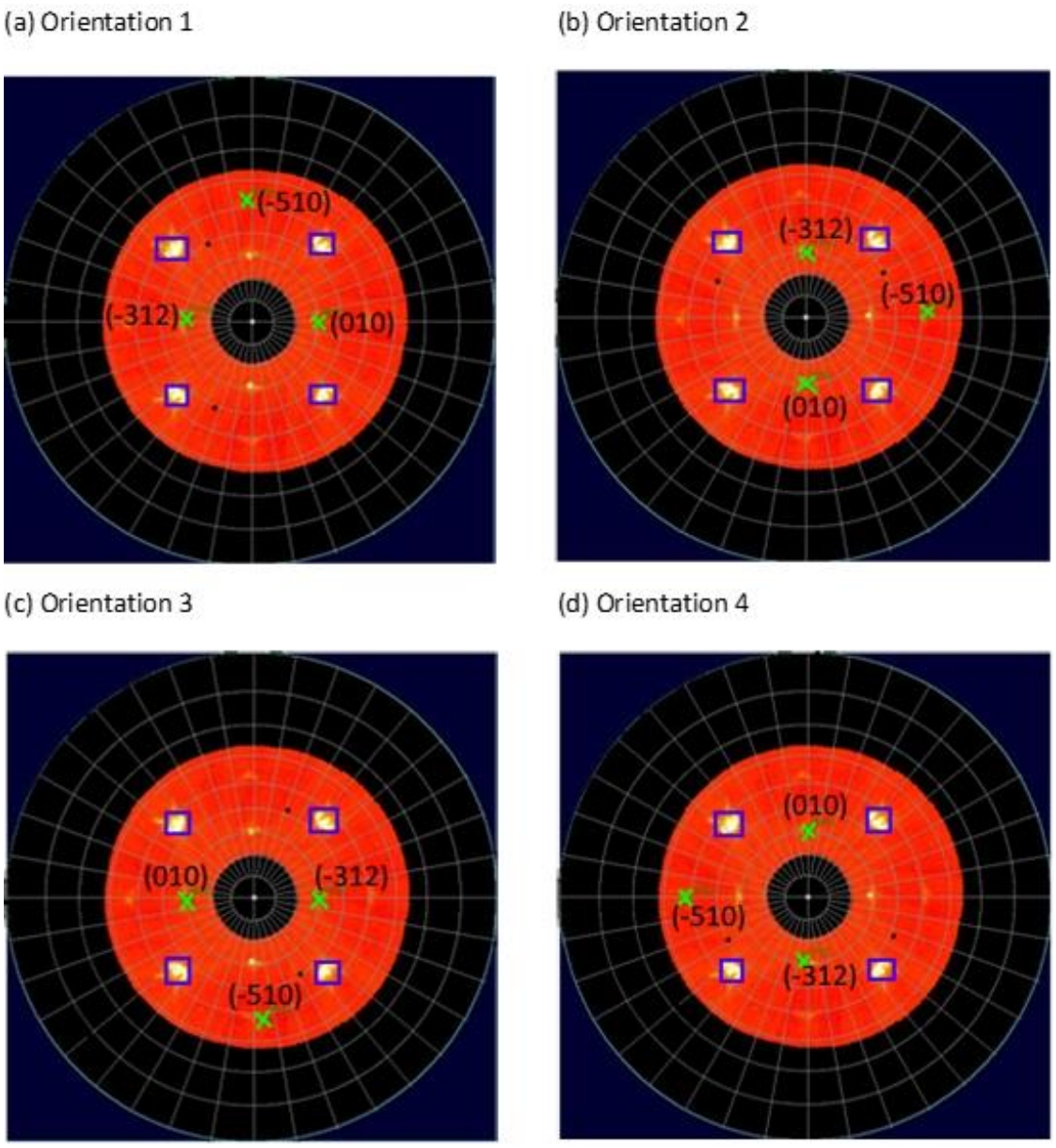

FIG. 7. Experimental pole figure analysis of experiment 6, integrated between 2θ=46-48°, encompassing in that range 7 different families of planes from the monoclinic CoGe phase: <5 1 0>, <1 1 2>, <3 1 -2>, <5 1 -1>, <6 0 0>, <0 2 0>, and <6 0 -1>. Four orthogonal growth orientations are identified with observed hkl peaks labelled in green. The black spots correspond to weaker reflections not detected experimentally. The blue squares indicate <2 2 0> Ge substrate peaks.

Experiments 4 and 5 were annealed at 227°C in vacuum for 24 and 48 hours, respectively. During the anneal, in-situ scans were taken every 2 hours. In-situ scans of the sample annealed for 24 hours, were able to detect germanide growth clearly after 10 hours with the growth of a peak at approximately 55°, indicating the β-Co_5Ge_3 phase. This is shown in the colour map in figure 8. This result is in agreement with experiment 6, in which β-Co_5Ge_3 was clearly detectable after 10 hours as well. Figure 9 shows the post-anneal scan results which confirm the formation of β-Co_5Ge_3. The pole figure analysis shown in figure 10 demonstrates the highly ordered polycrystalline nature of the phase. The film resulted in two orientations 180° apart with the principle axis [0 -1 0] perpendicular to the sample surface. The same results were seen in the post-anneal scan for the 48 hour anneal (experiment 5).

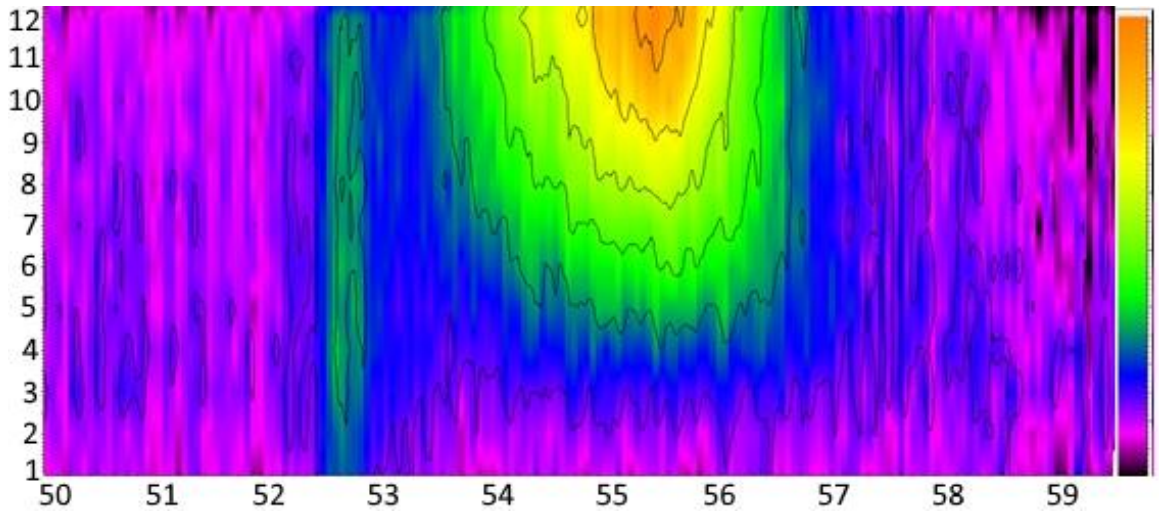

FIG. 8. The colour map of experiment 4 in-situ scans measured on Co-Kα displays 2θ values on the horizontal axis and 2 hour time intervals on the vertical axis. The map clearly depicts the growth of a peak at 55° belonging to the β-Co_5Ge_3 phase after 10 hours. Growth of the peak at 52.5° corresponds to crystallization of the PEEK dome during the anneal.

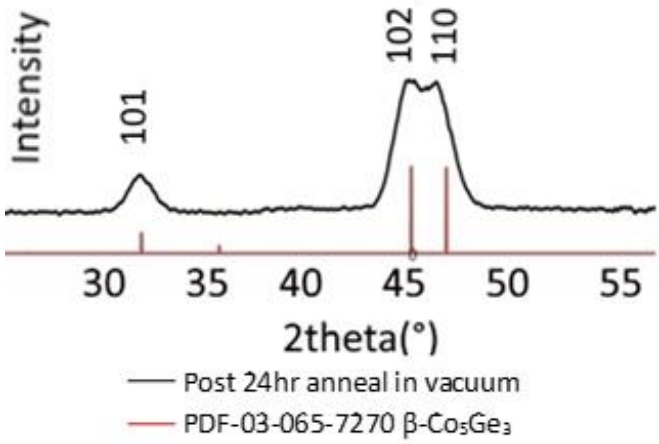

FIG. 9. Post-anneal 2θ texture analysis of experiment 4 measured on Cu-Kα1 (black) identified the phase as β-Co_5Ge_3 (red).

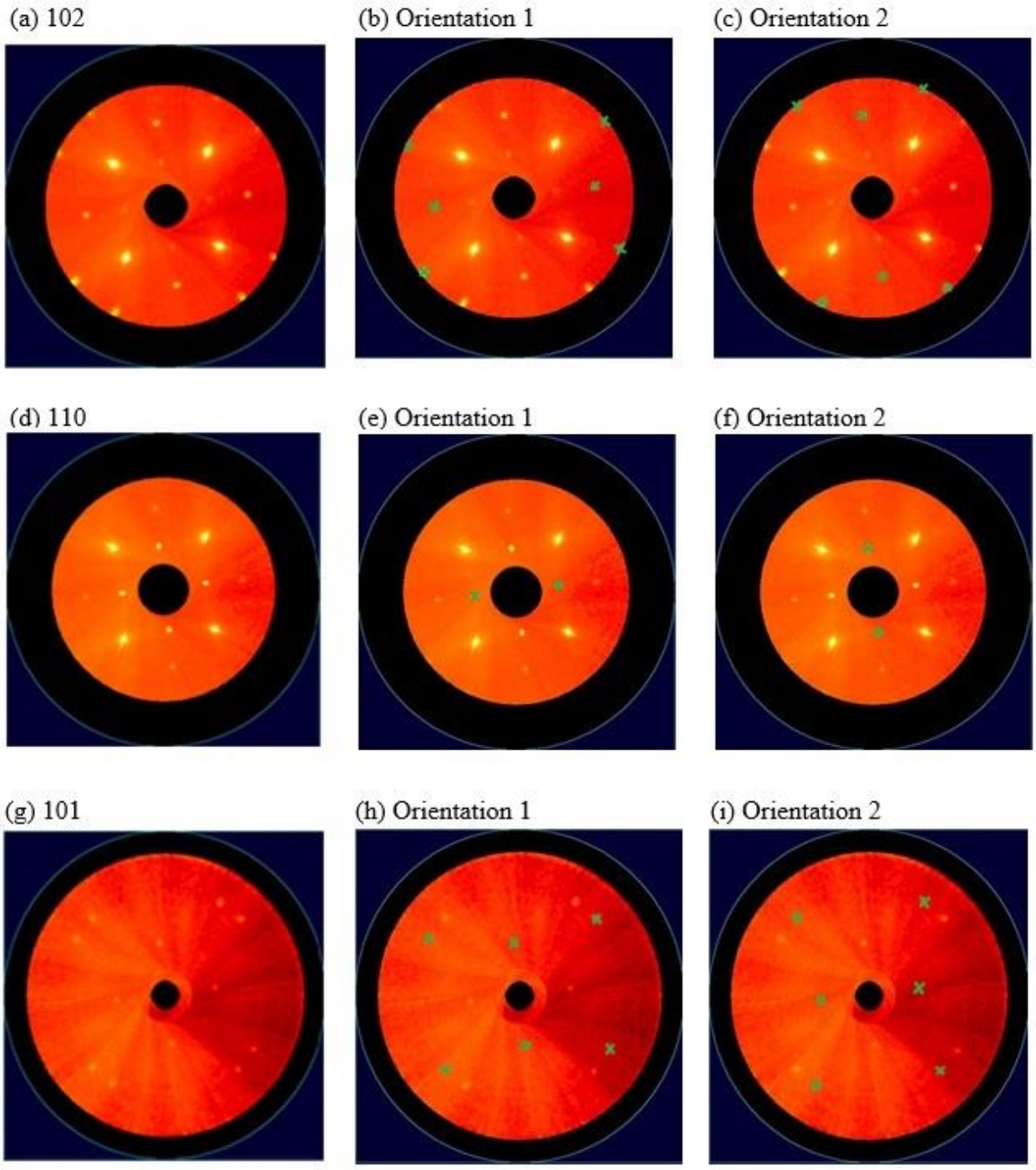

FIG. 10. Experimental pole figure analysis of experiment 5 reveals two orientations of β-Co_5Ge_3, 180° apart with principle axis [0 -1 0] perpendicular to the sample surface. Peaks measured on <1 0 2>, <1 0 1> and <1 1 0> planes are labelled with green crosses.

Our in-situ and post-anneal experimental results showed that the first phase to form in the cobalt germanidation reaction is β-Co_5Ge_3. Given sufficient reaction time in an ambient of air at atmospheric conditions, monoclinic CoGe subsequently forms. Under vacuum and atmospheric conditions β-Co_5Ge_3 becomes detectable after 10 hours. No monoclinic CoGe formed under vacuum conditions for anneals up to 48 hours. We expect a transformation of β-Co_5Ge_3 to monoclinic CoGe under vacuum conditions if the reaction continues for a time sufficient to consume all the cobalt.

Both the presence of oxygen and the higher pressure of the atmospheric ambient compared with the vacuum anneals could also have an effect on the germanidation rate. It has been previously observed that the presence of oxygen retards silicidation rates.[25] It is expected that presence of oxygen would have an effect on the germanidation reaction rate as well. However, based on previous reports we expect these two factors to have a minor effect.[25] This is also consistent with our result that the onset of formation of β-Co_5Ge_3 is the same regardless of ambient.

However, as indicated above, the subsequent behavior is strongly affected by the ambient, with CoGe forming after about 20 hours in air and not forming up to 48 hours in vacuum. For anneals in air ambient at atmospheric pressure, Co reacts simultaneously with germanium and oxygen in the atmosphere forming, respectively, cobalt germanide at the growth interface and cobalt oxide on the surface. This increases the rate at which Co is consumed compared to reactions under vacuum conditions. When the Co has been completely consumed, Ge reacts with β-Co_5Ge_3 to form monoclinic CoGe. The longer the reaction time the more β-Co_5Ge_3 gets consumed until it is completely transformed into monoclinic CoGe. The reaction steps are summarized in figure 11. It has been established in silicide/silicon systems that Si is the diffusing species in the silicidation reaction.[26] For cobalt germanidation, experiments have also shown that germanium is the diffusing species.[27] A solid state reaction is a dynamic non-equilibrium process and it is usually found that one compound phase forms at a particular interface.[28] This is different from equilibrium systems in which a mixture of phases might lead to the lowest free energy state for the system. Our experimental results show that monoclinic CoGe forms through the indirect reaction that we have described. Indirect reactions to form the second phase have been previously reported for nickel silicides in

which nickel reacts with Si to form Ni_2Si which in turn reacts with Si forming NiSi.[29] The similarities between our understanding of the cobalt germanidation reaction and the nickel silicidation results provides further support to our theory. β-Co_5Ge_3 forms first but the same temperature is sufficient to cross the energy barrier needed for monoclinic CoGe formation. Monoclinic CoGe is the most thermodynamically stable phase at low temperatures.

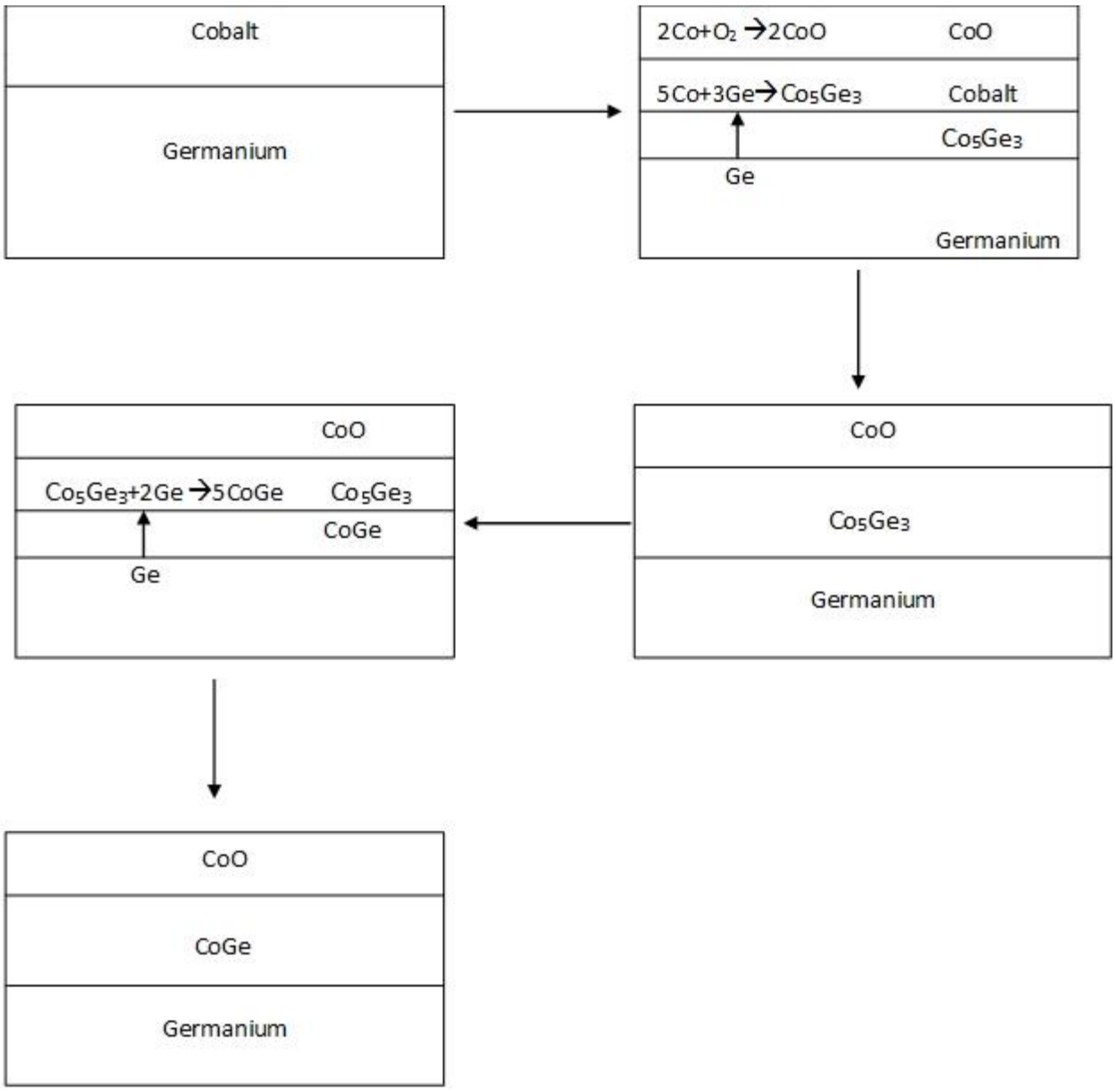

FIG. 11. Diagram depicting steps of the solid state reaction of cobalt germanidation in atmospheric conditions.

Anneal time plays a key role in formation of the first phase and subsequent phase transformations. In our experiments the first phase to form was only detectable after 10 hours at 227°C. Hsieh et al.[17] obtained a weak XRD signal after a 1 hour anneal at 220°C indicating nucleation of some germanide but not sufficient to identify the phase of the germanide formed. Their experiment was on (111)Ge and ours was on (100) but there is insufficient data in

the literature to postulate an orientation dependence. At 184.5°C we detected no germanide after a 48 hour anneal. Therefore, for practical purposes, the onset temperature for germanidation is somewhere between 185°C and 220°C. However, in experiments with fast temperature ramps[5,18] the onset temperature is higher because of the time required for the reaction to produce a detectable germanide film. In these fast ramp cases the initial phase to form may be different than for a constant temperature anneal or the initial phase may be missed during in-situ monitoring. For example, at high temperatures between 450°C-655°C both theoretical[28] and experimental[5] results lead to an expectation of Co_5Ge_7 as the final phase to form. This is consistent with our own experiment at 457°C. Yet Opsomer et al.[18] did not observe this phase (Co_5Ge_7) in cobalt germanidation on amorphous Ge despite having a similar setup to Gaudet et al.[5] Opsomer et al.[18] observed, instead, $CoGe_2$. Both studies: Opsomer et al.[18] and Pretorius et al.[28] only detected monoclinic CoGe and the β-Co_5Ge_3 phase was missed, either because there was insufficient reaction time at lower temperatures to form β-Co_5Ge_3 or because the phase was missed during in-situ monitoring.

Our finding that β-Co_5Ge_3 is the first phase to form at low temperature is supported by the data of Wittmer et al.[15] who conducted a 20 hour anneal at 250°C. They identified the phase formed as Co_2Ge, but this has been shown in later detailed phase diagram study to be β-Co_5Ge_3.[22]

Only one phase forms at a time in solid thin film reactions.[30] There are two models in the literature that can predict unambiguously the first phase to nucleate in binary solid reactions: the Walser-Bené rule[31] and the Effective Heat of Formation (EHF) model.[28] Walser and Bené (WB) proposed that, "*The first compound nucleated in planar binary reaction couples is the most stable congruently melting compound adjacent to the lowest-temperature eutectic on the bulk equilibrium phase diagram*".[31] The only congruent solid phase in the Co-Ge phase diagram is β-Co_5Ge_3.[22] Therefore, the WB rule predicts β-Co_5Ge_3 to be the first phase to form. Conversely, the EHF model predicts the first phase to form to be the phase with the lowest effective heat of formation. In the Co-Ge system this is monoclinic CoGe. However, Pretorius et al.[28] have pointed out that non-congruent phases do not nucleate easily at a moving interface and are usually skipped. This suggests that β-Co_5Ge_3 should be the first phase to form despite monoclinic CoGe having the lowest effective heat of formation. Our results support this understanding.

Only two orientations were observed in the formation of the hexagonal Co_5Ge_3 and only four orientations in the case of monoclinic CoGe. The principal axis for β-Co_5Ge_3 was [0 -1 0] and the principal axis for monoclinic CoGe was [-1 1 1]. Highly ordered cobalt germanides are advantageous for use as ohmic contacts in semiconductor devices since they result in a lower Schottky barrier height than amorphous contacts.[32] $CoSi_2$ has been previously reported to grow a single crystalline phase on (111)Si.[17] Therefore, Co results in good ohmic contacts for both germanides and silicides. Epitaxial Co_5Ge_7 has been previously reported by Hsieh et al.[17] after 1 hour anneal at 500°C. Partial epitaxy with two different orientations has been observed for $CoGe_2$ resulting from anneals performed between 600°C-700°C.[17] The epitaxial growth covered about 70% of the surface in this case. Partial epitaxial growth has also been reported by Sun et al.[19] for Co_5Ge_7. De Keyser found three epitaxial orientations of Co_5Ge_7 grown on (100)Ge and five of $CoGe_2$ on (100)Ge.[33] Our work is the first study that reports the partial epitaxial nature of both β-Co_5Ge_3 and monoclinic CoGe. It can be concluded that all phases of cobalt germanides that form during anneal-based germanidation result in good quality contacts with either single crystal or highly ordered polycrystalline structure.

4- Conclusion

We have studied cobalt germanidation during constant temperature anneals at temperatures from 94°C to 457°C. The anneal at 457°C was conducted for 1 minute and resulted in Co_5Ge_7 consistent with previous experiments at high temperatures as well as theoretical prediction. For temperatures at or below 185°C after 48 hour anneals no cobalt germanides were detected. We monitored cobalt germanidation using in-situ XRD at 227°C for 24-48 hours. β-Co_5Ge_3 was shown to be the first phase to form and was clearly detected in-situ after 10 hours in vacuum and in atmosphere. In vacuum, β-Co_5Ge_3 was the only detected phase even after 48 hours of anneal. Monoclinic CoGe formed in case of atmospheric germanidation and was clearly detected after 48 hours. In-situ XRD monitoring shows a phase change after about 20 hours of anneal. The formation of β-Co_5Ge_3 is consistent with the Walser-Bené rule and the transformation to monoclinic CoGe indicates an indirect reaction to form the thermodynamically stable phase. Post-anneal XRD texture analysis showed highly ordered polycrystalline structures for both β-Co_5Ge_3 and monoclinic CoGe phases.

Acknowledgements

We would like thank Dr. James Britten from McMaster Analytical X-Ray Diffraction facility for fruitful discussions. We also gratefully acknowledge the assistance of Ryan Koh, Efe Ijevu, and Ishaq Aden-Ali. The work was supported by a grant from the Natural Science and Engineering Research Council (NSERC).

References

[1]D. A. Buchanan, IBM Journal of Research and Development **43,** 245 (1999).

[2]X. Huang, W.-C. Lee, C. Kuo, D. Hisamoto, L. Chang, J. Kedzierski, E. Anderson, H. Takeuchi, Y.-K. Choi, and K. Asano, in *Sub 50-nm finfet: Pmos*, Washington, 1999 (IEEE), p. 67.

[3]C. Claeys and E. Simoen, *Germanium-based technologies: from materials to devices* (Elsevier, 2011).

[4]K. J. Kuhn, A. Murthy, R. Kotlyar, and M. Kuhn, ECS Transactions **33,** 3 (2010).

[5]S. Gaudet, C. Detavernier, A. J. Kellock, P. Desjardins, and C. Lavoie, Journal of Vacuum Science & Technology A: Vacuum, Surfaces, and Films **24,** 474 (2006).

[6]D. P. Brunco, K. Opsomer, B. De Jaeger, G. Winderickx, K. Verheyden, and M. Meuris, Electrochemical and Solid-State Letters **11,** H39 (2008).

[7]J. Kittl, K. Opsomer, C. Torregiani, C. Demeurisse, S. Mertens, D. Brunco, M. Van Dal, and A. Lauwers, Materials Science and Engineering: B **154,** 144 (2008).

[8]S.-D. Kim, C.-M. Park, and J. C. Woo, IEEE Transactions on Electron Devices **49,** 457 (2002).

[9]T. Nishimura, K. Kita, and A. Toriumi, Applied Physics Letters **91,** 123123 (2007).

[10]A. Chawanda, C. Nyamhere, F. D. Auret, W. Mtangi, T. T. Hlatshwayo, M. Diale, and J. M. Nel, Physica B: Condensed Matter **404,** 4482 (2009).

[11]S.-h. C. Baek, Y.-J. Seo, J. G. Oh, M. G. Albert Park, J. H. Bong, S. J. Yoon, M. Seo, S.-y. Park, B.-G. Park, and S.-H. Lee, Applied Physics Letters **105,** 073508 (2014).

[12]Y. Zhou, M. Ogawa, X. Han, and K. L. Wang, Applied Physics Letters **93,** 202105 (2008).

[13]J. Bardeen, Physical Review **71,** 717 (1947).

[14]C. Krontiras, S. Georga, S. Sakkopoulos, E. Vitoratos, and J. Salmi, Journal of Physics: Condensed Matter **2,** 3323 (1990).

[15]M. Wittmer, M. A. Nicolet, and J. W. Mayer, Thin Solid Films **42,** 51 (1977).

[16]T. Grzela, W. Koczorowski, G. Capellini, R. Czajka, M. W. Radny, N. Curson, S. R. Schofield, M. A. Schubert, and T. Schroeder, Journal of Applied Physics **115,** 74307 (2014).

[17]Y. F. Hsieh, L. J. Chen, E. D. Marshall, and S. S. Lau, Applied Physics Letters **51,** 1588 (1987).

[18]K. Opsomer, D. Deduytsche, C. Detavernier, R. L. Van Meirhaeghe, A. Lauwers, K. Maex, and C. Lavoie, Applied Physics Letters **90,** 31906 (2007).

[19]H. P. Sun, Y. B. Chen, X. Q. Pan, D. Z. Chi, R. Nath, and Y. L. Foo, Applied Physics Letters **86,** 71904 (2005).

[20]S. Ashburn, M. Öztürk, J. Wortman, G. Harris, J. Honeycutt, and D. Maher, Journal of electronic materials **21,** 81 (1992).

[21]L. Lajaunie, M.-L. David, K. Opsomer, E. Simoen, C. Claeys, and J. F. Barbot, Solid State Phenomena **131-133,** 107 (2008).

[22]K. Ishida and T. Nishizawa, Journal of Phase Equilibria **12,** 77 (1991).

[23]S. K. Sahari, H. Murakami, T. Fujioka, T. Bando, A. Ohta, K. Makihara, S. Higashi, and S. Miyazaki, Japanese Journal of Applied Physics **50,** 04DA12 (2011).

[24]H. Tompkins and J. Augis, Oxidation of Metals **16,** 355 (1981).

[25]M. Berti, A. Drigo, C. Cohen, J. Siejka, G. Bentini, R. Nipoti, and S. Guerri, Journal of applied physics **55,** 3558 (1984).

[26]J. D. Plummer, *Silicon VLSI technology: fundamentals, practice and modeling* (Prentice Hall, 2000).

[27]S. Dhar and V. Kulkarni, Thin Solid Films **333,** 20 (1998).

[28]R. Pretorius, T. Marais, and C. Theron, Materials Science Reports **10,** 1 (1993).

[29]R. Černý, V. Chab, and P. Přikryl, Computational materials science **4,** 269 (1995).

[30]C. Theron, O. Ndwandwe, J. Lombaard, and R. Pretorius, Materials chemistry and physics **46,** 238 (1996).

[31]R. Walser and R. Bene, Applied Physics Letters **28,** 624 (1976).

[32]C. Wronski, D. Carlson, and R. Daniel, Applied Physics Letters **29,** 602 (1976).

[33]K. De Keyser, R. L. Van Meirhaeghe, C. Detavernier, J. Jordan-Sweet, and C. Lavoie, Journal of The Electrochemical Society **157,** H395 (2010).

Chapter 3

Novel Experimentally Calibrated Multiphase TCAD Model for Cobalt Germanide Growth

M. A. Rabie, I. Aden-Ali and Y. M. Haddara, "Novel experimentally calibrated multiphase TCAD model for cobalt germanide growth," *2017 International Conference on Simulation of Semiconductor Processes and Devices (SISPAD)*, Kamakura, Japan, 2017, pp. 69-72.

***Abstract*—**We propose the first multiphase TCAD cobalt germanide growth model that can predict the resulting phase based on germanidation time, temperature, and ambient. The model has been calibrated to experimental results reported in the literature as well as our own data. This model can help in the design of cobalt germanide contacts with low resistance.

Keywords—silicidation, germanidation, cobalt silicide, cobalt germanide, kinetic model

1- Introduction

A major change has been seen in the industry in the last two decades with the incorporation of high percentages of Ge in MOSFET devices to benefit from the stress engineering in improving the mobility of carriers in those devices. Silicon germanium and pure germanium metal contacts are formed using both silicides and germanides. The industry has a mature understanding of silicides and they have been used for many decades now.[1] Less attention has been given to germanides.[2] Careful selection of contact materials and control of the contact formation process are needed for an efficient contact to the CMOS devices and to minimize the contact resistance. The reduction in the contact resistance is necessary since it contributes directly to the RC circuit delays associated with a signal propagating through the device. RC time delays have become an obstacle in obtaining faster integrated circuits in recent years.

The need for high quality contacts in Ge-based devices is the primary motivation for the study of cobalt germanidation. Cobalt is a good candidate for the contact material in Ge-based devices given its compatibility with silicon process, stability, and low resistivity.[3,4] The contact resistance contribution from metal resistivity depends on

the germanide phase. Resistivities of CoGe and $CoGe_2$ at room temperature have been reported to be 65.7 and 150 μΩ.cm, respectively.[5] This wide resistivity range emphasizes the importance of careful cobalt germanide contact design.

The temperature at which each of these phases forms also varies. It is important to understand the phase formation sequence in order to design a high quality, low resistivity cobalt germanide contact that forms at a temperature compatible with the semiconductor process. Cobalt germanidation has been the subject of a number of studies.[5-12] Different phases have been reported to form during cobalt germanidation including Co_5Ge_3, CoGe, $CoGe_2$, and Co_5Ge_7. Once the initial phase forms, the sequence of phases to appear for longer reaction times will be determined by the Co-Ge balance. Under Ge-rich conditions we will move to the right on the phase diagram, whereas Co-rich conditions will drive the reaction to the left on the phase diagram.

Technology Computer Aided Design (TCAD) models for silicidation are being used in the industry to predict the accurate shape of the silicide, the effect of silicidation on the dopant profiles, and the stress in silicon resulting from silicidation.[1] These predictive models help in designing devices as well as understanding unwanted behavior resulting from the process steps. TCAD saves the industry time and money that can otherwise be spent on expensive and time consuming experiments. Multiphase silicide models have gained importance in recent years with the use of nickel silicides.[13] Nickel silicides have multiple phases with different resistivities. It is important for the process designer to design the process in such a way to obtain the specific silicide with the target resistivity. The process can be accurately designed using TCAD simulations.

Cobalt germanidation has multiple phase outcomes similar to nickel silicidation. The process is also very similar since the cobalt is deposited on germanium as nickel is deposited on silicon. The wafer is, then, annealed to obtain the desired silicide or germanide. There are no reports in the literature on the progress of the cobalt germanide thickness with anneal temperature and time. However, there are many[5-12] reports for the dependence of the resulting phase on time, temperature, and ambient of the experiment. These reports are sufficient to calibrate the model parameters to accurately predict the cobalt germanide phase depending on time, temperature, and ambient of the process. In

addition, the thickness dependence can also be obtained given the phase transformation with the process conditions. The model is described in the next section and the simulation results are discussed in the third section of this paper.

2- The Model

Co_5Ge_3 is the first phase to form by diffusion of Ge through the forming Co_5Ge_3 layer and the reaction of Ge and Co at the Co_5Ge_3-Co interface to form new Co_5Ge_3 layers.[4, 14] Cobalt germanidation process is illustrated in figure 1. The EHF model [15] predictions and experimental results [3, 4] show that, in the presence of excess Ge, the next phase to form is CoGe which is the phase to the right of Co_5Ge_3 in the phase diagram.[16] CoGe will not form until either all cobalt is consumed or the thickness of the Co_5Ge_3 layer causes the germanidation reaction to become diffusion limited. CoGe and Co_5Ge_3 are expected to coexist until cobalt is fully consumed. At that point, Ge will continue to react with Co_5Ge_3 forming CoGe and consuming the remaining Co_5Ge_3. The next phase to form will be Co_5Ge_7 and finally $CoGe_2$. The phases to the left of Co_5Ge_3 in the phase diagram [16] won't form unless Co is in excess of Ge in the system.

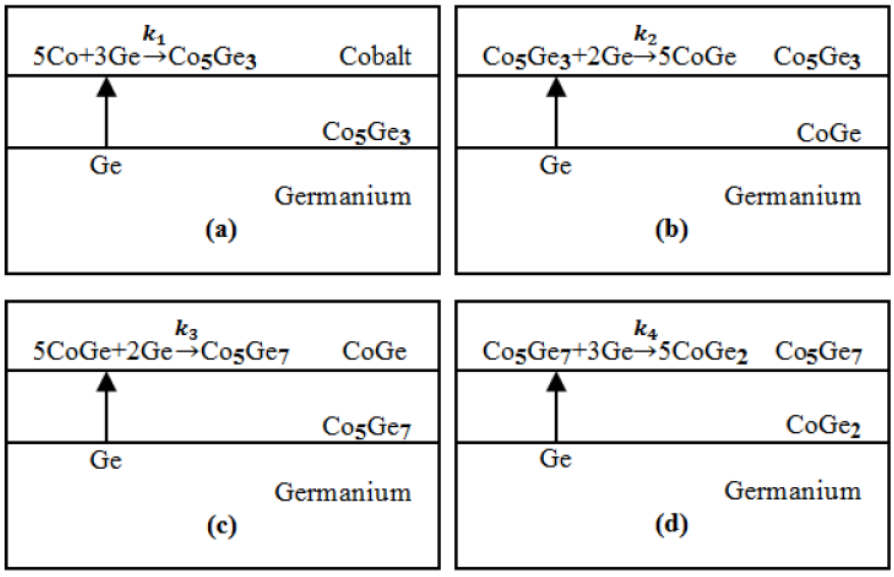

Figure 1: Illustration of cobalt germanidation.

During cobalt germanidation, the four reactions shown in figure 1 take place. The reaction rates, k_1-k_4, have Arrhenius dependence on temperature similar to the silicon oxidation model.[1] The reverse reactions are thermodynamically unfavorable and have not been reported in the experimental literature previously. Therefore, the reverse reactions are not considered in the TCAD model. The rate of consumption of cobalt is proportional to its reaction rate constant (k_1) with Ge to form Co_5Ge_3.[17] k_1 is the reaction constant assuming Co is available at its equilibrium concentration at the reacting interface and, therefore, it needs to be scaled by the actual concentration of cobalt available at the interface: C_{Co}/C_{Co0}. The rate of generation of Co_5Ge_3 at the Co-Co_5Ge_3 interface is proportional to the concentration of germanium at the interface C_{Ge}. 3 Ge atoms are needed to form one Co_5Ge_3 molecule. Therefore, the rate of generation of Co_5Ge_3 or consumption of Co is proportional to (⅓)C_{Ge}. The rate of consumption of Co is 5 times that of generation of Co_5Ge_3 since it takes 5 Co atoms to form one Co_5Ge_3 molecule:

$$\frac{\partial C_{Co}}{\partial t} = -\frac{5}{3} k_1 \frac{C_{Co}}{C_{Co_0}} C_{Ge} \qquad (1)$$

where C_{Co0} is the solid solubility of cobalt in Co_5Ge_3. Equation (1) doesn't limit the forming phase at the interface to Co_5Ge_3; other phases are possible mathematically despite not physically possible. This has been handled by careful calibration of the model.

Co_5Ge_3 is generated when Co and Ge react and is consumed when Ge reacts with Co_5Ge_3 forming CoGe. 2 Ge atoms are needed in the reaction. Therefore, the rate of consumption of Co_5Ge_3 is proportional to ½ C_{Ge}. k_2 is the reaction rate assuming the concentration of Co_5Ge_3 is the equilibrium concentration and has to be scaled by the available concentration of Co_5Ge_3 $C_{Co5Ge3}/C_{Co5Ge30}$:

$$\frac{\partial C_{Co_5Ge_3}}{\partial t} = \frac{1}{3} k_1 \frac{C_{Co}}{C_{Co_0}} C_{Ge} - \frac{1}{2} k_2 \frac{C_{Co_5Ge_3}}{C_{Co_5Ge_{3_0}}} C_{Ge} \qquad (2)$$

The constant $C_{Co5Ge30}$ is the number of Co_5Ge_3 molecules per unit volume in a pure Co_5Ge_3 material.

Equation (2) can be generalized: when a phase is consumed, it contributes to the formation of the next phase. When the right hand side of the above equation yields an overall positive value, it implies Co_5Ge_3 is growing. When it is a negative value, Co_5Ge_3 is being consumed. The generation/consumption of both CoGe and Co_5Ge_7 are very

similar in nature to the generation /consumption of Co_5Ge_3 described above. The equations governing their growth /consumption are:

$$\frac{\partial C_{CoGe}}{\partial t} = \frac{5}{2} k_2 \frac{C_{Co_5Ge_3}}{C_{Co_5Ge_{3_0}}} C_{Ge} - \frac{5}{2} k_3 \frac{C_{CoGe}}{C_{CoGe_0}} C_{Ge} \qquad (3)$$

$$\frac{\partial C_{Co_5Ge_7}}{\partial t} = \frac{1}{2} k_3 \frac{C_{CoGe}}{C_{CoGe_0}} C_{Ge} - \frac{1}{3} k_4 \frac{C_{Co_5Ge_7}}{C_{Co_5Ge_{7_0}}} C_{Ge} \qquad (4)$$

The equation that governs $CoGe_2$ is slightly different from the equations used for the other phases. The main difference is that $CoGe_2$ is never consumed, as it is the last phase to form:

$$\frac{\partial C_{CoGe_2}}{\partial t} = \frac{5}{3} k_4 \frac{C_{Co_5Ge_7}}{C_{Co_5Ge_{7_0}}} C_{Ge} \qquad (5)$$

Since Ge is the diffusing species, the diffusion term of Ge is used to describe the generation rate of Ge. Ge is consumed by reacting with Co or with cobalt germanides forming new phases of cobalt germanides. All 4 phases have to be considered in this case:

$$\frac{\partial C_{Ge}}{\partial t} = \nabla.(D_{Ge} \nabla C_{Ge}) - k_1 \frac{C_{Co}}{C_{Co_0}} C_{Ge} - k_2 \frac{C_{Co_5Ge_3}}{C_{Co_5Ge_{3_0}}} C_{Ge} - k_3 \frac{C_{CoGe}}{C_{CoGe_0}} C_{Ge} - k_4 \frac{C_{CoGe_2}}{C_{CoGe_{2_0}}} C_{Ge} \qquad (6)$$

D_{Ge} is the germanium diffusivity in cobalt germanide and has Arrhenius dependence on temperature.

The flux of Ge at the reacting interface is given by:

$$F_{Ge} = -D_{Ge}(C_{Ge} - C_{Ge}^*) \qquad (7)$$

where C_{Ge}^* is the solid solubility of Ge in cobalt germanide. Germanides react with germanium to form new germanide phases. Germanide flux is given by:

$$F_{Co_xGe_y} = -\frac{m_n r_n}{\sum r} F_{Ge} \qquad (8)$$

where r is the multiphase reaction rate for different germanides and m_n is a stoichiometric constant. 3 Ge atoms are needed to form one molecule of Co_5Ge_3: m_1=⅓. r_n and m_n values are presented in table 1.

The consumed volume of cobalt is:

$$\frac{\partial v_{Co\ Consumed}}{\partial t} = -5F_{Co_5Ge_3}\Omega_{Co} = -\frac{5\Omega_{Co}r_1}{3\sum r}F_{Ge} = -\frac{\beta}{DR}F_{Ge} \quad (9)$$

where Ω_{Co} is the atomic volume of Co, R is the conversion ratio from consumed material: Co to the growing material: Co_5Ge_3, D is the density of the growing material: Co_5Ge3, and β is a stoichiometric constant. The assumption of the model is that cobalt reacts with germanium forming only Co_5Ge_3 which, then, reacts with germanium again to form other germanide phases. β and D for various germanides are summarized in table 1.

Table 1: Parameters for different phases

Growing phase	m_n	r_n	β_n	$D_n\ (cm^{-3})$
Co_5Ge_3	$1/3$	$k_1\frac{C_{Co}}{C_{Co_0}}$	$5/3$	1.525083e22 [18]
CoGe	$5/2$	$k_2\frac{C_{Co_5Ge_3}}{C_{Co_5Ge_{3_0}}}$	$1/2$	4.0745208e+22 [19]
Co_5Ge_7	$1/2$	$k_3\frac{C_{CoGe}}{C_{CoGe_0}}$	$5/2$	5.9296394e+21 [19]
$CoGe_2$	$5/3$	$k_2\frac{C_{Co_5Ge_7}}{C_{Co_5Ge_{7_0}}}$	$1/3$	2.3082184e+22 [18]

The consumed volumes of the other 3 germanides can be obtained using table 1 in a similar way to equation 9. The total growing volume of the germanide is given by the sum of the growing volumes of the 4 individual germanides:

$$\frac{\partial v_{grow}}{\partial t} = \sum F_{Co_xGe_y}\Omega_{Co_xGe_y} = \frac{\sum \Omega_{Co_xGe_y}r_n m_n}{\sum r}F_{Ge} \quad (10)$$

The consumed volume of Ge is given by:

$$\frac{\partial v_{Ge\ Consumed}}{\partial t} = -F_{Ge}\Omega_{Ge} \quad (11)$$

3- Simulation Results

The model parameters were calibrated to correctly predict the resulting phase for different experimental conditions reported in the literature detailed in table 2. Most experiments report the final phase based on

measurements. Some experiments didn't report the measured final phase but instead speculated the phase based on other works. The model assumptions and the understanding of the germanidation process have been used in those cases to predict the correct resulting phase. Intermediate phases and germanide thickness progress have not been reported by any researchers. Hsieh et al. [8] reported interfacial reaction at 220°C. Cobalt didn't completely react at that temperature. The researchers weren't able to confirm the resulting phase to be CoGe or Co_5Ge_3. Based on our results in experiments 1 and 2 [4], we concluded that the resulting phase was Co_5Ge_3. Cobalt is not completely consumed in experiment 1, since in the longer time experiment 2, Co continues to react with Ge forming new layers of Co_5Ge_3. Oxidation of cobalt had to be considered for experiments: 3 and 6. After cobalt consumption in experiment 6, Ge reacted with the Co_5Ge_3 resulting in a new phase: CoGe as shown in figure 4. Cobalt is not expected to be completely consumed in experiment 3 as shown in figure 2 since Co_5Ge_3 was detected. Grzela et al. [7] didn't detect the actual forming phase in their experiments. They detected the structural changes in cobalt germanides forming at different temperatures and concluded the forming phases based on other works. Table 2 shows the expected phases in Grzela et al.'s work based on our model. Figure 3 shows all the results of experiments 1, 2, 4, and 5. All cobalt is consumed in experiment 8 since the detected phase was Co_5Ge_7 which will only result after Ge reacts with CoGe. CoGe forms through the reaction of Ge and Co_5Ge_3 after the consumption of cobalt.

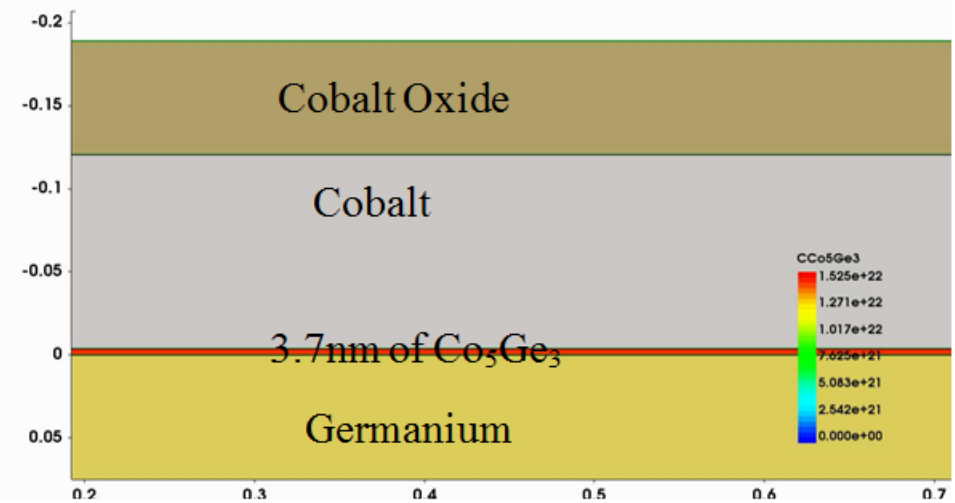

Figure 2: Experiment 3 simulation results after 1h anneal

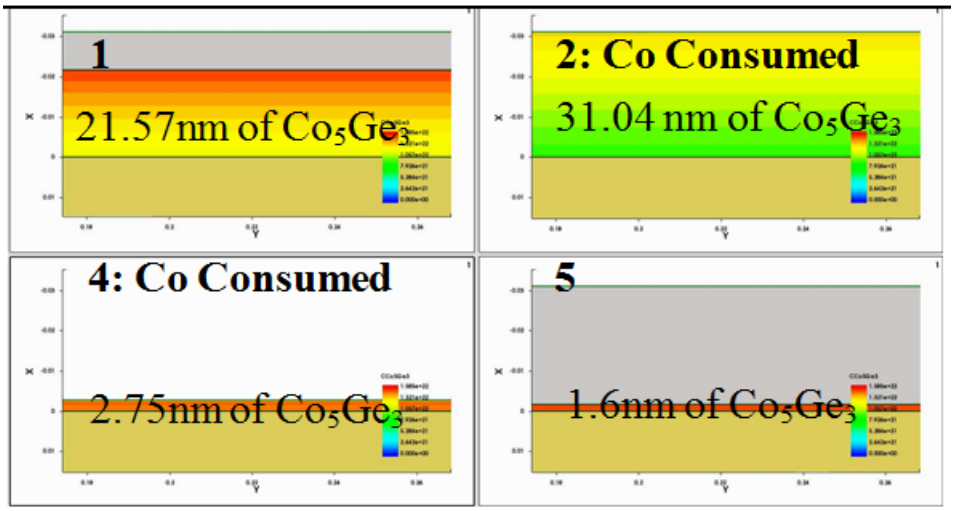

Figure 3: Experiment 1, 2, 4, and 5 simulation results. As the germanide gets thicker, the concentration of Co_5Ge_3 decreases and other phases form.

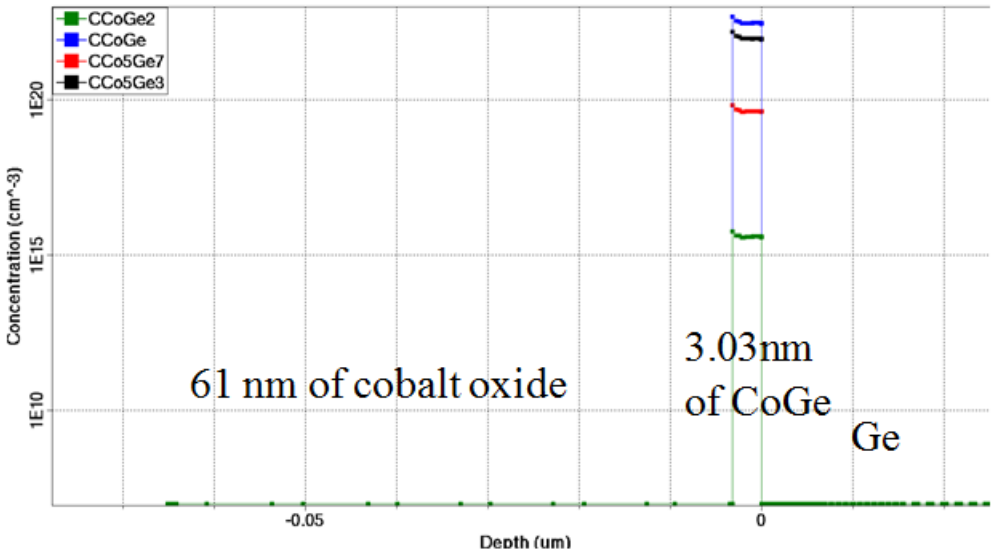

Figure 4: Experiment 6 results. Dominant phase is CoGe.

We are able to calibrate the reaction rates to fit the results of all the experiments in table 2. k_2, k_3, and k_4 are responsible for forming the later phases. Calibrating their values to the different conditions reported in the literature

allows us to all the experiments in table 2. k_2, k_3, and k_4 are responsible for forming the later phases. Calibrating their values to the different conditions reported in the literature allows us to obtain their temperature dependence. Their values are given in table 3. k_1 is the reaction rate to form the first phase as well as the rate of growth of the cobalt germanide. In all the experiments in table 2 the first phase has to form prior to forming other phases. We have not found reports of Co_5Ge_3 thickness as a function of time and temperature and there have not been many studies with long time anneals at different temperatures. k_1 has been calibrated by considering the different germanide growth rates to satisfy the results detailed above for the 10 experiments.

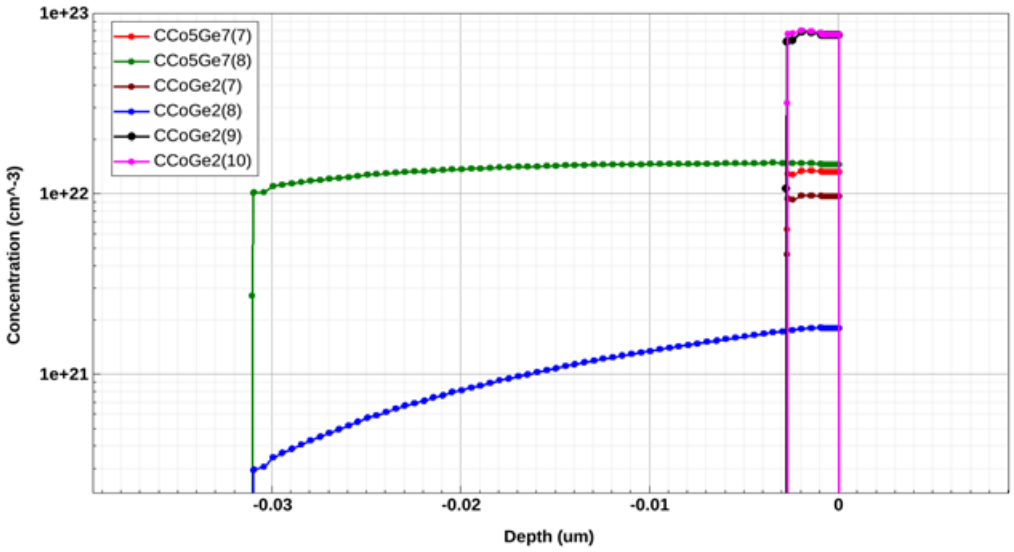

Figure 5: Experiment 7, 8, 9, and 10 results. Dominant phases are shown. Concentrations below$10^{20}cm^{-3}$ are not shown.

Table 2: Experimental parameters used in simulation

#	Temp.°C	Ambient	Time	Phase	Reference
1	227	Vacuum	24h	Co_5Ge_3	[4]
2	227	Vacuum	48h	Co_5Ge_3	[4]
3	250	Oxygen	1-20h	Co_5Ge_3	[6]
4	250	Vacuum	1h	Co_5Ge_3	[7]
5	220	Vacuum	1h	Co_5Ge_3	[8]
6	227	Oxygen	48h	CoGe	[4]
7	400	Vacuum	1h	Co_5Ge_7	[7]
8	457	Vacuum	1min	Co_5Ge_7	[4]
9	600	Vacuum	1h	$CoGe_2$	[7]
10	700	Vacuum	30min	$CoGe_2$	[7]

Table 3: Simulation calibrated reaction constants.

Arrhenius equation	A (s^{-1})	E_a(eV)	Respective Co-Ge phase
k_1	2e15	1.1	Co_5Ge_3
k_2	1.817e8	1.385	CoGe
k_3	1.897e13	2.07	Co_5Ge_7
k_4	9.2695e9	1.972	$CoGe_2$

4- Conclusion

The first multiphase kinetic TCAD model for cobalt germanidation was presented. The model parameters have been calibrated to experimental results reported in the literature. The model shows excellent agreement with experimental results and can explain all the results accurately. This model is an important process model for the design of cobalt germanide contacts.

Acknowledgment

We are grateful to Yujie Hu for her help. We would like to thank Dr. Peter Kruse for the useful discussions on solid kinetics.

References

[1] J. D. Plummer, M. D. Deal, and P. B. Griffin, "Silicon VLSI Technology: Fundamentals, Practice, and Modeling," Prentice Hall, Inc., 2000, pp. 737-744.

[2] J. A. Kittl, K. Opsomer, C. Torregiani, C. Demeurisse, S. Mertens, D. P. Brunco, M. J. H. Van Dal, and A. Lauwers, "Silicides and Germanides for Nano CMOS Applications," Mat. Sci. Eng. B-Solid 154-155, 2008, pp.144-154.

[3] S. Gaudet, C. Detavernier, A.J. Kellock, P. Desjardins, C. Lavoie, "Thin film reaction of transition metals with germanium," J. Vac. Sci. Technol. A 24, 2006, pp. 474-485.

[4] Mohamed A. Rabie, Souzan Mirza, Victoria Jarvis, and Yaser M. Haddara, "First phase to form during cobalt germanidation," J. Appl. Phys. 121, 2017, p. 145304.

[5] C. Krontiras, S. Georga, S. Sakkopoulos, E. Vitoratos, and J. Salmi, "The resistivity and Hall coefficient of CoGe and $CoGe_2$ thin films," J. Phys.: Condens. Matter 2, 1990, pp. 3323-3328.

[6] M. Wittmer, M. A. Nicolet, and J. W. Mayer, “The first phase to nucleate in planar transition metal-germanium interfaces,” Thin Solid Films 42, 1977, pp. 51-59.

[7] T. Grzela, W. Koczorowski, G. Capellini, R. Czajka, M. W. Radny, N. Curson, S. R. Schofield, M. A. Schubert, and T. Schroeder, “Interface and nanostructure evolution of cobalt germanides on Ge(001),” J. Appl. Phys. 115, 2014, p. 74307.

[8] Y. F. Hsieh, L. J. Chen, E. D. Marshall, and S. S. Lau, “Partial epitaxial growth of cobalt germanides on (111)Ge,” Appl. Phys. Lett. 51, 1987, pp. 1588-1590.

[9] K. Opsomer, D. Deduytsche, C. Detavernier, R. L. Van Meirhaeghe, A. Lauwers, K. Maex, and C. Lavoie, “Influence of Ge substrate crystallinity on Co germanide formation in solid-state reactions,” Appl. Phys. Lett. 90, 2007, p. 031906.

[10] H. P. Sun, Y. B. Chen, X. Q. Pan, D. Z. Chi, R. Nath, and Y. L. Foo, “Formation and evolution of epitaxial Co_5Ge_7 on Ge(001) surface by reactive deposition inside an ultrahigh-vacuum transmission electron microscope,”Appl. Phys. Lett. 86, 2005, p. 071904.

[11] S. Ashburn, M. Öztürk, J. Wortman, G. Harris, J. Honeycutt, and D. Maher, “Formation of titanium and cobalt germanides on Si (100) using rapid thermal processing,” J. Electron. Mater. 21, 1992, pp. 81-86.

[12] L. Lajaunie, M.-L. David, K. Opsomer, E. Simoen, C. Claeys, and J. F. Barbot, “Co-germanide Schottky contacts on Ge,” Solid State Phenom. 131-133, 2008, pp. 107-112.

[13] Sentaurus Process User Guide, Version M-2016.12, Synopsys Inc., December 2016.

[14] S. Dhar and V. N. Kulkarni, “Atomic transport in Cu/Ge and Co/Ge systems during ion-beam mixing,” Thin Solid Films 333, 1998, pp. 20-24.

[15] R. Pretorius, T. K. Marais, and C. C. Theron, “Thin Film Compound Phase Formation Sequence: An Effective Heat of Formation Model,” Mat. Sci. Eng. R. 10, 1993, pp. 1-83.

[16] K. Ishida and T. Nishizawa, " The Co-Ge (Cobalt-Germanium) System," J. Phase Equilib. 12, 1991, pp. 77-83.

[17] R. Černý, V. Chab, and P. Přikryl, "Numerical simulation of the formation of Ni silicides induced by pulsed lasers," Computational materials science 4, 1995, pp. 269-281.

[18] Kanematsu, K.; Yasukochi, K.; Ohoyama, T., "Magnetic properties of (Fe, Co) 1.67 Ge and (Fe, Ni) 1.67 Ge," J. Phys. Soc. Jpn. 18, 1963, pp. 1429-1436.

[19] Morozkin, A.V., "Gd-Co-Ge system at 870/1070 K," Intermetallics 25, 2012, pp. 136-138.

Chapter 4

Cobalt Germanide Contacts: Growth Reaction, Phase Formation Models, and Electrical Properties

Accepted in Journal of Materials: Materials in Electronics

Cobalt Germanide Contacts: Growth Reaction, Phase Formation Models, and Electrical Properties

Mohamed A. Rabie[(a)*], Souzan Mirza[(b)], Yujie Hu [(c)] and Yaser M. Haddara[(c)]

(a) GLOBALFOUNDRIES, Inc.
400 Stone Break Road Extension
Malta, NY 12020
USA

(b) Institute of Biomaterials & Biomedical Engineering
University of Toronto
Rosebrugh Building, 164 College Street, Room 407
Toronto, Ontario M5S 3G9 Canada

(c) Department of Electrical and Computer Engineering
McMaster University
1280 Main St. West,
Hamilton, ON
Canada L8S 4K1

*Corresponding author: **rabiema@gmail.com, (t) +1-518-930-8299**

Abstract:

State of the art of cobalt germanide contacts to semiconductor devices is reviewed in this article. First, evolution of contacts is covered from the dawn of the transistor to present day. The history of contact has three stages: a) elemental metals as direct contacts to the semiconductor with focus on aluminum, b) self-aligned silicide contacts, and, recently, c) the paradigm shift that emphasizes the interface contact resistivity. The second section outlines the current role of germanium in the semiconductor industry and the reasons cobalt germanide is an ideal contact material to germanium and silicon germanium semiconductor devices. Fundamental physical properties of cobalt germanides are presented next. Models for phase formation sequence are, then, detailed. This is followed by a comprehensive survey of the experimental results of formation of cobalt germanides. Those results are discussed and reconciled. Factors affecting the resulting phases and their quality are identified and some optimum choices for the experimental parameters are pointed based on the survey. After that, electrical properties of the contact are discussed. The role of germanium crystal orientation in ohmic and Schottky properties of the contact is analyzed. Fermi level pinning (FLP) plays a role mainly on metal/(100) n-type Ge interfaces. The role of FLP is minimal on p-

type Ge and other crystalline orientations even if they were n-type. Schottky barrier heights (SBH's) for cobalt and cobalt germanide contacts reported in the literature are surveyed. Mechanisms of fermi level pinning and methods adopted by the industry to depin the fermi level at the interface are outlined. The electrical properties section is concluded with a subsection that focuses on the effect of the crystallinity of the contact material on its electrical behavior. Crystalline epitaxial cobalt germanides are expected to have lower interface resistivities compared to those calculated based on the SBH survey. The role of heat during Co deposition to obtain epitaxial germanides is pointed. Finally, current challenges and future trends of cobalt germanide contacts are summarized.

Keywords: cobalt germanide, germanium, electric contact, cobalt germanide phases, fermi level pinning, Schottky barrier height.

Relevance summary:

- First comprehensive review for cobalt germanides contacts to semiconductor devices.
- A complete survey of the experimental results for forming germanide contacts provides in-depth understanding of the germanidation process and the parameters that contribute to variations in the contact phases and other physical properties.
- The cause for variability in Schottky barrier height for the same cobalt germanide formed by different processes is explained and all the process parameters causing such variations are detailed.

1- Evolution of Contacts to Semiconductor Devices:

Contact formation is an important step in backend process in the semiconductor industry. Careful selection of contact materials and control of the contact formation process are needed to have an efficient contact and minimize its resistance. It is necessary to reduce the contact resistance since it contributes directly to RC circuit delays associated with a signal propagating through the semiconductor device. RC time delays have become an obstacle in obtaining faster integrated circuits in recent years. In state-of-the-art devices, the contact area is shrinking due to the shrinkage of the device dimensions. The resistance of the contact is inversely proportional to its area. The smaller contact area will result in a higher resistance and consequently, a longer time delay. This emphasizes the need for lower contact resistance.

The history of contact formation for silicon CMOS devices is split into three stages. The first stage was aluminum contacts directly in touch with the semiconductor: silicon or germanium. Soon, it was realized that such contacts are destructive to silicon devices due to aluminum-silicon interdiffusion. That observation marked the dawn of the second stage in contact development, the era of self-aligned silicide barriers. Different silicide barriers were used as contacts and as diffusion barriers to eliminate the interdiffusion process between the top metal and the underlying silicon. Silicides were often formed by a uniform deposition of a metal that reacted with silicon at higher temperatures only in the areas where silicon was exposed to form a contact. The resistivity and the quality of the silicide were the main factors in the choice of the silicide material. In the last decade, as 3D devices became mainstream and the device dimensions were scaled down to the nanometer scale, the interface resistance became a major concern. The focus in the third stage, the current stage, is on interface resistance rather than resistivity of the silicide. In this section, we will summarize the major milestones in the three stages.

1.1-Aluminum as a Contact [1]:

Gold was the metal of choice in the very first transistor invented in 1947, the point contact transistor [2]. Shortly after, aluminum became the metal of choice for contacts in the early devices in the 1950's and contacts and interconnect layers in early integrated circuits in 1960's [3]. Aluminum was initially chosen because it serves the

dual purpose of an electrode and p-type dopant in germanium [3]. Several other reasons contributed to this early choice. Aluminum has low electrical resistivity at room temperatures. Additionally, the strong adhesion of aluminum to silicon and silicon dioxide and the good quality of the aluminum contact made it a good candidate. Aluminum reacts with SiO_2 at low temperatures forming a thin layer of Al_2O_3 which results in good adhesion of Al to SiO_2. This reaction also gets rid of the native oxide on Si which results in a good contact with Si. Finally, Al passivates the traps at the Si-SiO_2 interface by reacting with H_2O and converting it to free hydrogen resulting in annealing out the interface traps. This improves the quality of the interface. For all these reasons, Al was chosen to be the material of contacts and interconnects in early integrated circuits.

In the mid 1960's, Al-contact based devices lifetime became a concern [4, 5]. It was found that lifetime decreases with higher current density and higher temperature. This decrease in lifetime was caused by Al-Si interdiffusion [6]. As the technology advanced, an anneal step at 450˚C became necessary to activate the reaction of Al with the native silicon oxide and to obtain a better gate oxide/silicon interface by reducing the interface traps. Little change was seen in the current-voltage characteristics of the Al-Si contact up to 450˚C [7]. Temperatures higher than 450˚C would result in a significant change in current-voltage characteristics, because of the change in the Schottky barrier height [7-9]. This change is accompanied by silicon out-diffusion into the aluminum as well as Al spikes into the Si substrate that can be as deep as 1μm. Even at 450˚C silicon solid solubility in Al is as high as 0.5 atomic percent. The solubility increases rapidly to 1 atomic percent at 500˚C. Also the diffusivity of Si in polycrystalline Al is high. Therefore, Si in direct contact with Al tends to diffuse into Al creating voids in Si. Al does not reduce the native oxide uniformly leading to localized voids at the interface. Al penetrates those voids creating spikes into Si. Those deep spikes can short the diffused junction if the spike went deeper than the junction line. As a result, Al contacts cannot be practically used for junction depths less than 2-3um.

The Al spiking problem was solved by using Al that already has 1 atomic percent of Si which is the solubility limit of Si in Al at 500˚C. However, another problem arises when the contact structure is cooled down. The solubility limit of Si is lower at lower temperatures. The excess Si above solubility limit precipitates usually at the interface forming Si nodules. Those nodules have enough Al in them to make them p-type causing higher contact resistance to N^+ regions. This high contact resistance became a limiting factor for the circuit performance as the

device dimensions continued to shrink. The solution was to use barrier layers between aluminum and silicon to limit the interdiffusion.

1.2-Self-Aligned Silicide Barriers:

Barrier layers have specific requirements to perform their function efficiently. They should [1]:

a) Limit the interdiffusion between Al and Si up to 500˚C.

b) Be thermally stable.

c) Have low mechanical stress meaning the coefficient of thermal expansion close to that of Si.

d) Adhere to Si, Al, and SiO_2. There should be some minimal interfacial reaction between the barrier layer and Si and Al.

e) Have good electrical conductivity and low contact resistivity to both Si and Al.

Three different types of barriers were considered initially [10]: a) sacrificial barriers, b) stuffed barriers, and c) passive barriers. Sacrificial barriers act as a barrier until it is consumed. Refractory metals are commonly used. They are extremely resistant to heat and wear due to their very high melting points. Ti for example adheres well to both Si and SiO_2, has very low resistivity, and it reduces and breaks the native oxide resulting in a good electric contact. At low temperatures, it reacts with Al forming $TiAl_3$. It is consumed quickly for processing temperatures above 400˚C. It also reacts with Si forming titanium silicides at temperatures above 500˚C. Titanium acts as a good adhesion layer with other barrier layer on top but it is not a good barrier layer in itself. The low resistivity phase C54 of $TiSi_2$ forms at high temperatures (>700˚C) [8] and, therefore, Si out diffusion along the grain boundaries is more likely at those temperatures. This results in interdiffusion between Si and the top metal destroying the Si devices.

Si diffusion into the neighboring metal alloy could be prevented by doping the metal alloy with another element that reside in fast diffusion paths including grain boundaries and other structural defects [10]. This configuration is named stuffed barriers. Si diffusion in stuffed barriers is much slower than in undoped alloys. Ti-W alloy stuffed with nitrogen atoms was used as a diffusion barrier layer between Si and Al. Ti fraction of 10-30% helps the alloy

layer to adhere to Si and SiO_2 and increases its corrosion resistance. Ti in the alloy reacts with Al at a higher temperature (600˚C) than if it were alone. However, diffusion through the layer limits its use to 500˚C. The contact resistance of Ti-W alloy is not as low as the common silicides due to the difficulty in dissolving native oxide. It is common to use both PtSi and Ti-W alloy layered on top of each other as a barrier. PtSi provides the low resistivity contact to silicon and stuffed Ti-W alloy on top prevents the interdiffusion. There are two main problems with Ti-W alloy as a barrier layer. First, Ti diffuses into Al at temperatures as low as 400˚C increasing its resistance. Second, Ti-W alloy is brittle and causes high stress in Si that can result in cracking and peeling on the wafer.

TiN is a very common passive barrier layer. TiN is a polycrystalline material with a very small grain size; less than 10 nm. Diffusion is very slow through TiN. If nitrogen or oxygen is incorporated in those films, their quality is improved. TiN is chemically inert and does not react easily with any other layer. The electrical resistivity of TiN is low enough for it to be used as a local interconnect. However, its contact resistance to Si is higher than silicides. Therefore, it is commonly used with $TiSi_2$ underneath. TiN is compatible with $TiSi_2$ process. Ti can be deposited and then annealed in nitrogen ambient to form the silicide in the bottom and the nitride on top.

It is common to use both sacrificial and passive barrier layers together. Most refractory metal silicides satisfy the requirements for the barrier layers in contact with silicon. In addition, they result in a good metal-semiconductor contact that has [11]: a) low contact resistivity, b) good thermal stability, c) low sheet resistance, d) low formation temperature, e) good scalability, f) good uniformity and g) ability to selectively etch. Silicides are formed by blanket metal deposition of a metal on top of silicon followed by two annealing step. The first anneal is a low temperature anneal sufficient for the reaction of the metal with silicon forming the silicide; usually below 400˚C. The temperature has to be low enough not to cause diffusion of Si over the sidewall spacer resulting in short circuiting the device by connecting the gate and other terminals. The unreacted metal is then removed and a second high temperature anneal step follows to transform the silicide into the desired low resistivity phase.

There are a number of advantages in using silicides as barrier layers. First, the surface of silicon is consumed during the formation reaction and a new clean interface is obtained. This interface usually has better electrical characteristics, especially lower interface trap concentration, than the original interface since it was exposed

resulting in high density of traps and impurities. Second, the silicide is self-aligned. Silicides are only formed wherever silicon is exposed and then the extra metal can be etched away. There is no need for an extra mask for the silicidation step. In addition, the variability in the external resistance is reduced using this self-alignment technique. Third, the entire source and drain areas can be contacted since the metal is deposited everywhere and then etched away after annealing. The contact resistance to the local interconnects is reduced due to the large area of contact. The main contributor to the contact resistance is the silicide/silicon resistance rather than the silicide/barrier-layer/metal resistance. The large contact area reduces the contribution of the silicide/silicon to the contact resistance. Fourth, the silicide can be used as a local interconnect that is compatible with the Si process. Fifth, the silicide has low sheet resistance itself which results in improving the performance of the device. Sixth, silicides can be easily plasma etched. Finally, silicides do not exhibit much electromigration.

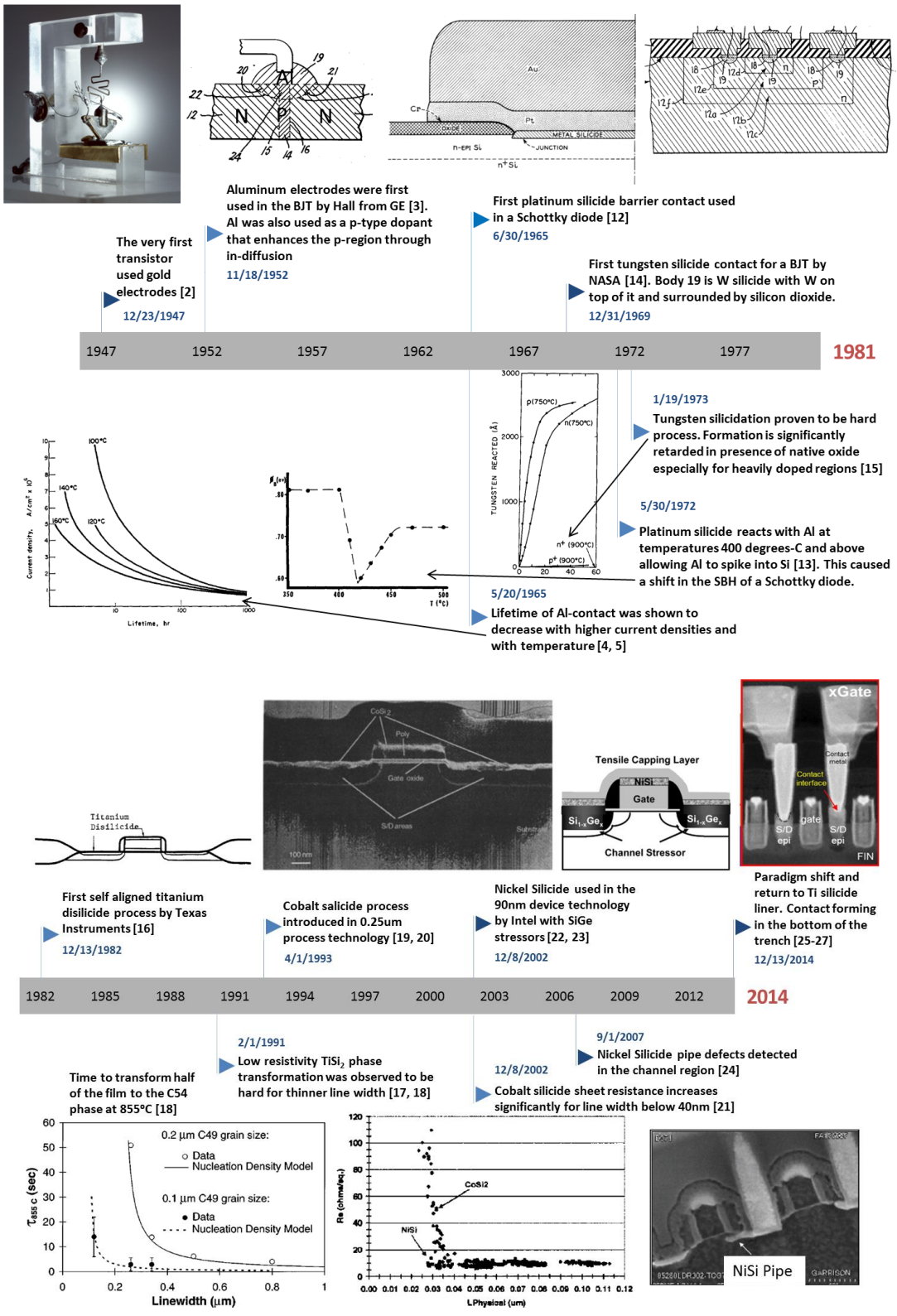

Figure 1: History of contacts to semiconductor devices from the inception of the transistor to the present time.

Platinum silicide was one of the earliest barrier layers used by the industry [12]. However, it is only suitable if no subsequent processing above 400˚C is done and if the junction depths underneath are greater than 0.3um. At such temperatures PtSi reacts with Al forming Pt-Al intermetallic compounds and allows Al to spike into the Si substrate [13]. Tungsten silicide has also been one of the early choices [1, 14] as a contact given that it can be deposited using CVD. CVD deposition provides good step coverage and good process control. Tungsten silicide can be easily oxidized resulting in a high quality dielectric layer on top. However, tungsten silicide results in high stresses in the structure which often cause stability and adhesion problems [28]. In addition, tungsten silicide cannot be easily formed through reaction with Si [15]. The formation reaction is significantly retarded in the presence of a native oxide between the metal and silicon especially for heavily doped surfaces [15]. Thus, it is harder to form self-aligned tungsten silicides.

Titanium silicide was the barrier metal of choice once the industry learned how to control the shorting problem between the gate and the drain [16, 27]. The advantage of $TiSi_2$ is that it reacts with Al at higher temperatures than noble metal silicides like PtSi (500˚C for $TiSi_2$). As mentioned previously, Al diffusion into the Si is expected at the silicidation temperatures used to form $TiSi_2$. Titanium silicide is, therefore, used with another barrier layer on top. TiN is mostly used and can be formed in the same process with $TiSi_2$ by annealing in a nitrogen ambient. This gives an advantage to using $TiSi_2$ in having less process steps. TiN is a better diffusion barrier than $TiSi_2$. It blocks most dopants from diffusing. Titanium silicide low resistivity phase ("C54") is able to reduce native oxides, and adheres well to silicon and most other materials. The first low temperature anneal would result in a high resistivity $TiSi_2$ phase ("C49"). The second anneal step would transform this phase into the desired C54 phase that is about four times lower in resistivity. It was soon observed that the thinner line width reduces the nucleation density required for phase transformation especially for line width <0.25 μm [11, 17, 18, 27, 29]. Therefore, as the line width decreased to 0.25 um and lower, it became hard to form the low resistivity phase. Both phases C49 and C54 coexisted resulting in variability in the resistance between different circuit components. In addition, thin $TiSi_2$ films tend to agglomerate at higher annealing temperatures [30]. Agglomerates are non-uniform masses of titanium silicides that form in multiple locations of the film causing non-uniformity of the film thickness, increased surface roughness, and

increased sheet resistance. Small percentages of Ta or Nb were added to improve the nucleation of the low resistivity phase but this was not able to sustain the $TiSi_2$ for too long and another metal was needed [27, 31, 32].

Although the resistivity of cobalt silicides is slightly higher than that of titanium silicides and the adhesion is not as good, cobalt silicides give a practical solution to agglomeration and high resistivity phase problems of titanium silicides. Thin cobalt silicide films do not agglomerate at higher annealing temperatures. $CoSi_2$, also, behaves better than $TiSi_2$ in terms of change in resistivity during anneal. In addition, cobalt silicides cause less lateral encroachment into the neighboring oxides and nitrides than titanium silicides. $CoSi_2$ was reported to grow epitaxially as single crystalline material on top of (111) Si substrates [33]. Single crystalline silicides or germanides eliminate the possibility of metal diffusion through the grain boundaries. Finally, $CoSi_2$ is more resistive to HF etching which gives it a strong processing advantage over $TiSi_2$. $CoSi_2$ replaced $TiSi_2$ starting the 0.25 μm technology given the aforementioned advantages [19, 20]. The cobalt silicidation reaction is more sensitive to surface contaminants and oxides which can lead to non-uniform silicidation and junction leakage. Therefore, an additional cleaning step for the contact areas became crucial to obtain the desired $CoSi_2$ quality contact [8]. Also, cobalt had to be capped with a TiN film to inhibit its reaction with the existing oxygen in the annealing environment [8, 20]. A new defect was observed with the replacement of Ti by Co silicide resulting from the fast diffusion of Co into Si: a sword like silicide penetration through junctions similar to the old Al issue [27, 34]. The spike silicides formed by in-diffusion of Co followed by reaction of Co with Si. The spikes grow rapidly during annealing at temperatures between 400 to 450°C for 30 seconds to reach a length of 20 to 100 nm which is enough to break shallow junctions [34]. Higher temperature anneals can resolve the spikes issue since the surface silicidation reaction becomes faster than the in-diffusion of Co. The optimum silicidation temperature window is 800-850°C [34].

As dimensions continued to shrink, cobalt silicide also showed scalability issues [11, 27]. The sheet resistance of cobalt silicides increased significantly for linewidths below 40nm [21]. This, again, is a problem related to nucleation issues. $CoSi_2$ grows from the reaction of the high resistivity CoSi with Si. That process is nucleation controlled. For linewidths below 40nm, $CoSi_2$ cannot nucleate and CoSi starts to agglomerate. As a consequence, anneal will result in an increase rather than a decrease in the resistivity since more CoSi forms. In addition, voids

form in the source/drain areas in silicon and are attributed to out diffusion of silicon from areas where the supply of silicon is limited. The high surface roughness for such cobalt silicides is another consequence of the nucleation limited formation of $CoSi_2$ [35]. Alloying nickel with cobalt has been reported to reduce the nucleation temperature for the di-silicide phase [11]. The presence of Ge with the introduction of silicon germanium (SiGe) in CMOS technology further delayed the nucleation of cobalt silicide [36]. The solubility of Ge is higher in CoSi than in $CoSi_2$ [35]. Germanium has to be expelled from CoSi before the formation of $CoSi_2$ resulting in further delayed nucleation of the low resistivity phase [37, 38]. As the Ge percentage increases, the formation temperature of $CoSi_2$ increases [37]. For Ge concentration as low as 20%, the formation temperature of $CoSi_2$ could be as high as 800°C. As Ge concentration increases the formation temperature approaches the melting temperature of Ge [37]. This closed the process window for cobalt silicide and the industry moved to a different silicide that was considered more compatible with the SiGe process.

Nucleation issues are not present in nickel silicidation. Nickel silicidation process is mainly interface or diffusion limited. A clean planar uniform interface forms at NiSi/Si surface. The interface growth front advances according to the diffusion-limited thickness proportional to square root of time Deal-Grove relation [39]. The smoother NiSi/Si interface is an advantage especially for Silicon-On-Insulator (SOI) applications in which the interface can be closer to the buried oxide without creating a direct contact [35]. Formation of nickel silicides for dimensions below 25 nm has been experimentally shown to be possible [11]. Nickel silicide was used in the 90 nm technology and became the standard starting the 65 nm technology node [22, 40]. The NiSi low resistivity phase is formed at lower temperatures even on SiGe substrates. Ge presence doesn't retard low resistivity NiSi formation to the same extent than it does for $CoSi_2$ [41]. NiSi forms at temperatures as low as 350°C compared to 600°C for $CoSi_2$ [35]. The ease of formation could be attributed to two factors. First, the solubility of Ni is four times higher than that of Co in Si at high temperatures and six times higher at lower temperatures [35]. Second, the diffusivity of Ni is higher than that of Co in Si at lower temperatures [35]. On the other hand, NiSi cannot withstand high temperature given its fast diffusion into silicon at high temperatures [27, 42]. Two steps RTA (rapid thermal anneal) was used to form the desired nickel silicide contact. The first RTA controls how much nickel is supposed to react. Then the

excess nickel is etched away on top of silicon as well as other areas in the structure. The second RTA drives the reaction to completion forming the target NiSi thickness and phase.

Ni is the dominant diffusing species creating a new clean interface between Si and the silicide. Nickel silicidation is, therefore, much less sensitive to oxygen presence compared to cobalt process. The fact that Ni is the diffusing species also resolves the voids issue that was observed for smaller dimensions during cobalt silicidation. However, the very fast diffusion of Ni has led to unwanted excess silicidation causing poly depletion and increasing the leakage current [21]. The subsequent BEOL processing steps to the nickel silicidation should always keep the temperature below 500°C to minimize the leakage caused by Ni diffusion as well as excessive silicidation resulting from unintended nickel diffusion to unwanted areas in the structure. High temperatures should also be avoided to avoid the formation of $NiSi_2$ high resistivity phase and to avoid agglomeration of NiSi thin films [35]. This agglomeration results from the anisotropic nature of the coefficients of thermal expansion of NiSi which causes significant localized variation in mechanical stresses. $NiSi_2$ phase formation could be retarded by adding Pt or Pd to the $NiSi_2$ and the agglomeration issue could be reduced by implantation of BF_2 [35]. On the other hand, temperatures below 450°C result in deep level defects due to the in-diffusion of Ni into Si which is faster than the rate of interface front advancement at those temperatures [43]. Despite solving the high resistivity phase and the agglomeration problems, the encroachment problem related to excess silicidation proved to be a difficult problem to solve and required very careful process control [24, 35].

The consumption of silicon is lower in nickel silicidation compared to cobalt silicidation for two reasons [35]: the low resistivity cobalt phase is silicon rich and NiSi has lower resistivity (~13-14 μΩ-cm) compared to $CoSi_2$ (~18 μΩ-cm) and therefore a thinner NiSi layer could be used to obtain the same sheet resistance of a thicker $CoSi_2$ layer. Lower Si consumption is an advantage for Si limited applications like SOI devices. Interstitial dopants pile up near the NiSi-silicon interface during silicidation and the dopants are activated at low temperatures (<600°C) resulting in reduced junction leakage and contact resistivity [27, 44, 45]. Despite this apparent advantage, two issues have been identified when looking at the impact of dopants on nickel silicidation [11]. First, it has been observed that pyramidal silicide grains form at low temperatures on p-type Si as a result of direct epitaxial growth of $NiSi_2$. This is a significant challenge for PMOS devices since it creates diode leakage issues. Surface preparation before Ni

deposition has been shown to reduce this issue. Second, the addition of dopants has a big impact on silicidation kinetics and thermal stability of the films. In particular, the snowplow effect of dopants causes retardation of the silicidation kinetics and, therefore, higher temperatures might be required causing all the issues discussed previously [46].

1.3- Paradigm Shift to Interface Contact Resistivity Criterion:

The introduction of the FinFET in the industry [47] caused a paradigm shift in the criteria for choosing contact metals. Multiple factors contributed to this change [27]: 1) replacement of the polysilicon gate to metal gates eliminating the need for silicide contact for the gate, 2) the newly developed process step for forming the source/drain (S/D) contacts involve etching a trench to reach the S/D and forming a liner silicide that is covered by another metal, typically tungsten, reducing the importance of silicide resistivity, and 3) with this process change there was no need for selective etch since the excess metal is removed by Chemical Mechanical Polishing (CMP). Criteria for the new linear silicide contacts are low intrinsic resistivity (ρ_c) between metal and Si [48] and morphological stability due to reduction in line width [27]. Intrinsic resistivity is primarily reduced by increasing doping at the interface, increasing process temperature to activate more dopants, and decreasing process time to reduce diffusion of dopants from the interface into the device. Therefore, ideal metals for silicide will react at high temperatures to allow dopant activation. High processing temperature will also result in faster dopant diffusion away from the interface and a decrease in active dopant concentration at the interface. Therefore, the selection of the silicidation temperature has to be done carefully to achieve high activation and minimal diffusion away from the interface. The high active dopant concentration at the interface results in substantial carrier tunneling through the narrow Schottky barrier at the contact interface decreasing the intrinsic resistivity [49]. Multiple metals meet the criteria mentioned above including Ti, Ni, and Co. However, since the high resistivity phase of Ti is not an obstacle any more given the paradigm shift discussed above, the industry quickly returned to Ti contacts given the advantages presented in the previous subsection [25-27]. The return to Ti resolved the main NiSi issue of encroachment.

The high doping concentration option is not feasible for some applications including solar cells in which low doping in the contact region is required for high efficiency [50] and junction-less nanowires transistors, recently suggested, to replace conventional transistors [51]. Therefore, research continues to consider silicides other than pure titanium silicide with lower workfunction [52] or to utilize techniques other than high doping to lower the intrinsic resistivity as will be discussed later in this work. Other attempts are also taking place to lower the contact resistivity of titanium silicide [53-56]. Lower Schottky barrier height is beneficial for lower contact resistivity. This is difficult to achieve on n-Si due to Fermi-Level-Pinning (FLP) [57, 58]. One of the current solutions is to utilize metal/insulator/n-Si contact stack. Such contact system cannot withstand high temperatures [55, 57]. Another solution is to utilize Ge pre-amorphization implant (Ge PAI) [55]. A record low $1.5x10^{-9}\Omega\text{-cm}^2$ contact resistivity was achieved on n-type Si using such an implant with phosphorus dose as high as $2x10^{21}cm^{-3}$ [55]. High P concentrations suppress Ti silicidation rate. The effect of Ge PAI is to enable Ti silicidation at a low temperature of $550^{\circ}C$ limiting P in-diffusion, while simultaneously, achieving high activation levels of P during solid phase epitaxial regrowth (SPER) of amorphized Si due to the implant. However, such an implant is unfavorable for the channel mobility of n-type devices given the compressive stress it is expected to create in the channel. It was later replaced with a pre-amorphizing phosphorus implant [56] resulting in an even lower contact resistivity of $8.4x10^{-10}\Omega\text{-cm}^2$. Complicated process was used and the tight control on the forming titanium silicide phase pose restrictions on later process thermal budget. Ge PAI was also successful in obtaining very low contact resistivities in the range of $3.8x10^{-9}\Omega\text{-cm}^2$ in p+ SiGe MOSFETs [59]. The active boron concentration used was $4x10^{20}cm^{-3}$ and the silicidation had to be performed in the low temperature range of $450^{\circ}C$-$525^{\circ}C$. Higher or lower silicidation temperatures would result in an appreciable increase in the contact resistivity. Cobalt silicide for liner has received less attention in recent years but it remains as a possible candidate given the paradigm shift especially with the possibility of growing a single crystalline silicide on silicon.

2- Rise of Germanium and Need for Germanide Contacts:

Germanium was the key substrate material in the early days of the semiconductor transistor as it had the best crystalline quality at the time [2]. However, Si soon replaced Ge as the material of choice [60] and has dominated the microelectronics industry for the last five decades. This silicon domination is mainly for two reasons. First, the high quality and stable oxide that forms as a dielectric on top of silicon. By contrast, GeO_2 is a low quality unstable oxide that does not provide enough passivation of the surface. Second, the enormous amount of research and investment that has been made in silicon as a platform for MOSFET development. In recent years, two major changes have emerged in the industry. First, is the incorporation of high percentages of Ge in MOSFET devices to benefit from the stress engineering in improving the mobility of carriers in p-type FET devices. Second is the replacement of thick silicon dioxide with high-k dielectrics to match the requirements of scaling down the device dimensions. This eliminates one of the major advantages in using silicon and opens the door for new materials in the microelectronics industry.

Pure germanium is a strong candidate to be included in the industry given its higher carrier mobilities and its relative compatibility with the silicon process [61]. In addition, the instability of the germanium oxide that was seen as a disadvantage in early days of semiconductors becomes an advantage when using high-k dielectrics. For the same process conditions, the interfacial oxide thickness is significantly lower in case of a Ge substrate compared with Si [62]. This makes a direct interface between the high-k dielectric and Ge easily manufacturable compared to Si [63, 64], giving Ge an advantage in effective oxide thickness scalability. High concentrations of germanium are included in silicon FinFETs [47], the current workhorse in the advanced CMOS industry. The high concentration of germanium improves carrier mobility due to strain and bandgap engineering. CMOS devices in the future industry nodes, 7nm and beyond, do not seem to be possible without using a higher mobility material in the fin. Germanium again is a strong candidate for the future nodes of the FinFETs.

There are a number of major obstacles to overcome in the development of Ge FETs. One of those obstacles is the passivation of the Ge-dielectric interface which does not seem to be possible using conventional silicon techniques. A second problem is the low I_{on}/I_{off} ratio of Ge MOSFETs. Ge devices suffer from high leakage current

across p-n junctions due to the small bandgap of Ge (~0.67eV at room temperature compared with 1.1eV for Si) [65]. This leakage current dominates the off-state drain current of the transistors. In addition, it is difficult to obtain high active dopant concentration, especially in source and drain regions where such concentrations are needed [63]. The solubility of dopants in Ge is relatively low compared to Si [65] and dopants suffer from incomplete ionization. Small bandgap and lower active dopant concentrations in S/D regions compared to Si result in lower I_{on}/I_{off} ratio for Ge compared to Si devices. Metallic S/D regions have been proposed to overcome this issue [66]. A third problem is the lack of a complete understanding of the fundamental properties of germanium. For example, there is no agreement on the equilibrium concentration and diffusivities of vacancies in germanium. The development of many device and process models is based on those fundamental parameters. A fourth obstacle is the lack of understanding of the contact formation process and the quality of those contacts in Ge based technologies. Limitations on high active dopant concentration restrict the heavy doping technique used for lowering the contact resistivity which is effective in the case of silicides on Si. Fermi Level Pinning (FLP), which will be discussed in section 6, poses another problem in controlling the metal-Ge contact.

In addition to FLP, multiple processing issues exist in case of metal germanides. Various germanides and germanidation processes have to be understood and evaluated to gain better understanding of the contact formation process for germanium transistors. Melting points and Gibbs' free energy of germanide phases are lower than their silicide counterparts [67]. This indicates that germanides are less stable than silicides. They tend to react with third party species easier than silicides do. The low melting point also indicates that germanides have high reactive diffusion in them than the corresponding silicide phases [67]. Consequently, germanides form at lower temperatures compared to the corresponding silicide phases.

Gaudet et al [68] surveyed 20 different transition metal germanides for the use as contacts in CMOS technology. A first group of metals (Ti, Zr, Hf, V, Nb, and Ta) react with Ge at very high temperatures and are easily oxidized. A second group of metals (Cr, Mo, Mn, Re, Rh, Ru, Ir, and W) do not form low resistivity germanide phases. The third group of metals (Fe, Co, Ni, Pd, Pt, and Cu) formed low resistivity germanide phases at relatively low temperatures (150-360°C) and are therefore promising for further investigation and development. The lowest resistivities corresponded to NiGe and PdGe (22 and 30Ωcm, respectively).

Despite its low resistivity, PdGe has processing difficulties that are likely to limit its usage as a contact. Extra palladium has to be removed using aqua regia after germanidation [69]. Pure aqua regia etches Ge at 290 nm/min. This fast rate can be a killer in CMOS process if Ge is exposed. On the other hand, acids compatible with Ge processing like HCl, HNO_3, and H_2SO_4 can be used for etching Ni [69]. Another obstacle in the use of Pd is its high cost compared to other metals commonly used in the semiconductor industry [70].

Nickel germanides suffer from overgrowth onto neighboring oxide isolation [70]. Nickel germanides grow on the neighboring silicon dioxide isolation leaving behind voids in germanium due to germanium diffusion. Germanium is the diffusing species in the germanidation reaction with nickel [70]. This phenomenon seems to have similar root cause as the excessive nickel silicidation issue referred to in the previous section. The solution proposed by the researchers was to perform a two-step process with two low temperature RTAs (<350°C) similar to the solution proposed for excessive nickel silicidation. However, this overgrowth issue imposes a very restrictive thermal budget during back-end-of-the-line (BEoL) processes which can be impractical in a mass production setup. In addition, the two-step RTA does not completely solve the voids problem despite reducing it to a great extent.

Copper germanide was another candidate suggested by Gaudet et al. [68]. However, copper is the dominant contaminant in germanium for temperatures above 500°C [62]. This is mainly attributed to the high diffusivity of copper in germanium. Given its destructive effect on germanium devices due to deep level traps in the bandgap, copper is unlikely to be used for the purpose of creating contact on germanium. Fe and Co, on the other hand, have shown no midgap traps for germanidation temperatures up to 500°C [71]. In addition, cobalt related traps are mitigated using a long time anneal step at 700°C [72].

Platinum germanide contacts have been shown to be highly thermally stable over a wide range of temperatures (room temperature to 600°C) compared to Pd, Ni, and Co germanides [73]. It was also shown that platinum germanides contacts are the highest quality, with low reverse currents on the order of 10^{-6}-10^{-5} A. The issue with platinum silicide was its low temperature reaction with the metal on top. No complete designs have yet been reported in the literature for the stack of the platinum germanide contacts to CMOS devices. As for iron germanides,

several studies have been done [74-77] but none have investigated iron germanides' use as contacts for CMOS devices.

Despite the issues associated with titanium germanides, they are the preferred option given their compatibility with titanium silicides that the industry returned to with the paradigm shift discussed previously [78-80]. Contact resistivity as low as $3x10^{-9}$ $\Omega.cm^2$ was obtained on p-Ge wafer with boron concentration of $1x10^{21}cm^{-3}$ [79]. As discussed earlier, such high doping concentration might not be feasible for some applications. The onset of ohmic behavior was a boron concentration of $10^{20}cm^{-3}$. The specific titanium germanide phase obtained in the experiment and used for such application was not reported [79]. Ab-initio simulations showed that germanide phase effects the Schottky barrier height and, therefore, the contact resistivity. Ohmic contact was formed on n-Ge with a phosphorus doping concentration of $2x10^{19}cm^{-3}$ after RTA of deposited Ti at 600°C [80]. This process step resulted in C54 titanium germanide phase with a contact resistivity as low as $1.5x10^{-5}$ $\Omega.cm^2$. Further phosphorus implant after germanidation reduced contact resistivity to $3.6x10^{-6}$ $\Omega.cm^2$. The range of the contact resistivity for titanium germanide on n-type germanium is, therefore, much higher than that on p-type germanium. Another issue was the degradation of the interface quality between titanium germanide and Ge at high temperatures [78]. This issue will be discussed in section 6 of this paper. No interface degradation was observed in Chou et al.'s study [80]. This might be attributed to the different annealing time or dopant concentration. A more focused study is necessary to explain the cause of the interface degradation. Titanium as a metal, rather than its germanide, has also been used as a contact material for p-type germanium [54] and it gives a reasonable contact resistance of $1.1x10^{-8}$ $\Omega.cm^2$. Titanium was also able to clean the germanium interface of oxygen residues due to the high oxygen solubility and diffusivity in germanium. On the other hand, the sheet resistance of titanium cannot be reduced and the low thermal budget necessary to avoid germanidation could impose a restriction on the succeeding process steps.

The study of cobalt germanides as contacts is motivated by the compatibility with silicon process and the expected similarities between the behavior of cobalt silicides and cobalt germanides. Nowadays, silicon germanium alloys are commonly used in the advanced CMOS industry. It is expected that both pure germanium and pure silicon will be part of future CMOS devices. Having a metal that creates barrier layers compatible with both silicon and germanium would simplify the barrier-creation process. Tungsten, titanium, cobalt, and nickel are the most common

metals used in silicides. Cobalt, among those four, is the most suitable metal for creating both silicide and germanide contacts given the aforementioned issues with tungsten, titanium, and nickel germanides. In addition, it has been shown that cobalt germanides form low resistivity phases at lower reaction temperatures and are more resistive to oxidation than titanium germanides [68]. Low resistivity cobalt germanide phase can be formed using solid-state reaction at temperatures as low as 425°C [81]. This temperature range is compatible with Middle of Line (MOL) process and is lower than the formation temperature of the low resistivity titanium germanide phase, giving cobalt germanides a processing advantage. The interface contact resistivity of cobalt germanides is expected to be better than that of titanium germanides given the expected epitaxial nature of cobalt germanides similar to cobalt silicides. Also, cobalt silicides don't have the excessive silicidation problem that nickel silicides have and similar behavior is expected for cobalt germanides. Therefore of the four elements, cobalt seems to be the best choice of contact for pure germanium devices. Cobalt germanides also form high quality ohmic contacts to wide bandgap semiconductors like GaAs [81, 82]. Cobalt germanides nanostructures are also promising structures for memory applications given their superior memory characteristics [83]. Finally, cobalt diffusion in germanium was used to probe fundamental properties of the material like point defect properties [84], the activation energy, capture cross section for holes and electrons and trap concentration profiles [85, 86]. Experiments to probe fundamental properties of germanium could be designed more efficiently if the cobalt germanidation process is well understood as well as cobalt in-diffusion during germanidation. In particular, cobalt germanidation at temperature 600°C and higher has been identified as an easy method to introduce substitutional Co into n-type Ge [87].

3- Fundamental Physical Properties of Cobalt Germanides

Cobalt germanides exist in a number of different phases. Figure 2 shows the equilibrium phases in the Co-Ge system including: "*1- the liquid (L), 2- the Co-rich fcc terminal solid solution (αCo) where a terminal solid solution refers to a solid phase that exists at either of the extremities of the phase diagram, i.e. 0% or 100%, 3- the Co-rich hcp terminal solid solution (εCo), 4- Co_3Ge, 5- hexagonal Co_5Ge_2, 6- hexagonal β-Co_5Ge_3, 7- orthorhombic, low temperature α-Co_5Ge_3, 8- monoclinic CoGe, 9- tetragonal Co_5Ge_7, 10- orthorhombic $CoGe_2$, 11- cubic Ge*" [88].

The phase diagram of the cobalt-germanium binary alloy, shown in figure 2, is also useful in understanding the transition conditions between the different phases. Transition points are summarized in table 1. At 1210°C, the liquid phase L goes through a reaction to become solid hexagonal β-Co_5Ge_3. The reaction is a congruent reaction in which there is no compositional alteration during phase change from liquid to solid. At 1108°C, the liquid phase L transitions into εCo and hexagonal β-Co_5Ge_3 through a eutectic reaction where the liquid phase is transformed into two separate solid phases after cooling. At 985°C, β-Co_5Ge_3 and L react to form monoclinic-CoGe through a peritectic reaction in which a solid and a liquid phase transform into a single solid phase after cooling. At 832°C, monoclinic CoGe and the liquid phase L react and transform into $CoGe_2$. The lowest temperature the liquid phase L is in equilibrium is 817°C where L transforms into two solid phases: $CoGe_2$ and Ge in a eutectic reaction. At 806°C, CoGe and $CoGe_2$ react to form tetragonal Co_5Ge_7 through a peritectoid reaction in which two solids transform into a different solid phase after cooling. At 650°C, cubic Co_3Ge phase transforms into two different phases: εCo and hexagonal β-Co_5Ge_3 in a eutectoid reaction where one solid phase transforms into two distinct solid phases after cooling. Each of these transitions may occur during germanidation at elevated temperatures. As will be shown in the next section, Co_5Ge_3, CoGe , Co_5Ge_7 and $CoGe_2$ are the phases of interest in case of cobalt germanidation.

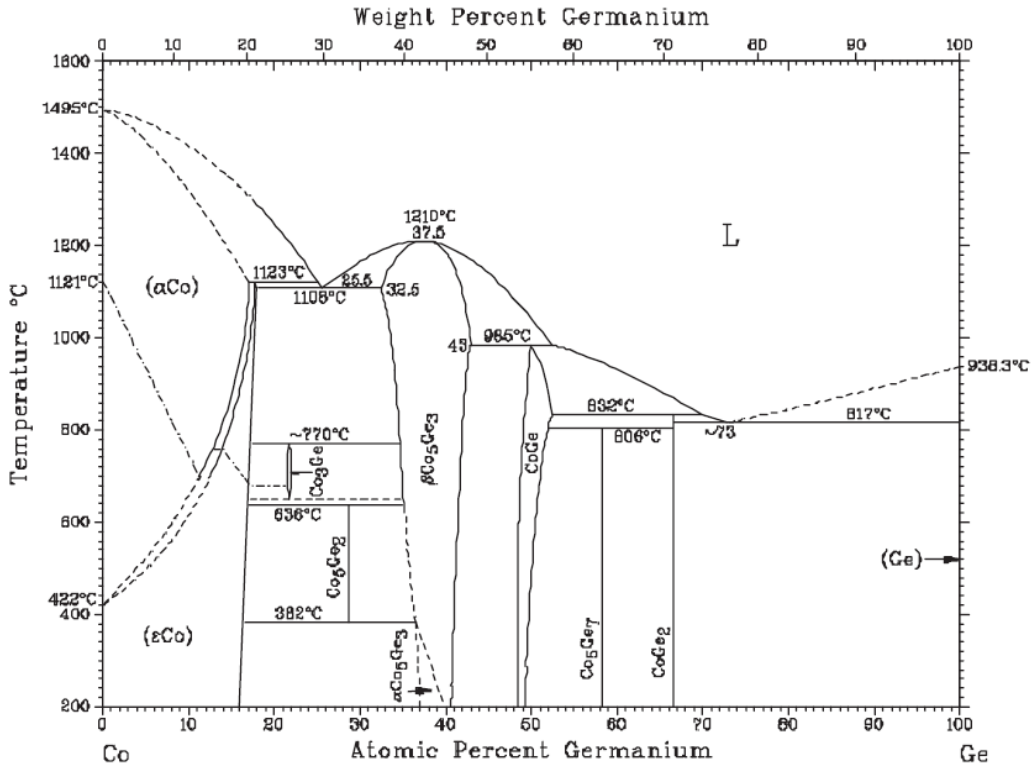

Figure 2: Phase diagram of Co-Ge binary alloy. Reprinted with permission from [88].

Table 1: Transition points in the cobalt-germanium phase diagram from [88].

Reaction	**Temperature °C**	**Reaction type**
$L \rightleftharpoons \alpha Co$	1495	Melting
$L \rightleftharpoons \beta Co_5Ge_3$	1210	Congruent
$L + \alpha Co \rightleftharpoons \varepsilon Co$	1123	Peritectic
$L \rightleftharpoons \varepsilon Co + \beta Co_5Ge_3$	1108	Eutectic
$\beta Co_5Ge_3 + L \rightleftharpoons CoGe$	985	Peritectic
$L \rightleftharpoons Ge$	983.3	Melting
$CoGe + L \rightleftharpoons CoGe_2$	832	Peritectic
$L \rightleftharpoons CoGe_2 + Ge$	817	Eutectic
$CoGe + CoGe_2 \rightleftharpoons Co_5Ge_7$	806	Peritectoid
$\varepsilon Co + \beta Co_5Ge_3 \rightleftharpoons Co_3Ge$	770	Peritectoid
$Co_3Ge \rightleftharpoons \varepsilon Co + \beta Co_5Ge_3$	650	Eutectoid
$\varepsilon Co + \beta Co_5Ge_3 \rightleftharpoons Co_5Ge_2$	636	Peritectoid
$\alpha Co \rightleftharpoons \varepsilon Co$	422	Allotropic
$Co_5Ge_2 \rightleftharpoons \varepsilon Co + \alpha Co_5Ge_3$	382	Eutectoid

An older version of the phase diagram is shown in figure 3 [89]. Comparing both phase diagrams, the more recent work identifies some new phases including Co_3Ge and Co_5Ge_2. In addition, new phases replaced older phases in the phase diagram. In particular, Co_5Ge_3 replaced Co_2Ge in the phase diagram. Co_2Ge(L) and Co_2Ge(H) could still be obtained by liquid quenching as demonstrated by Auderbrand et al. [90].

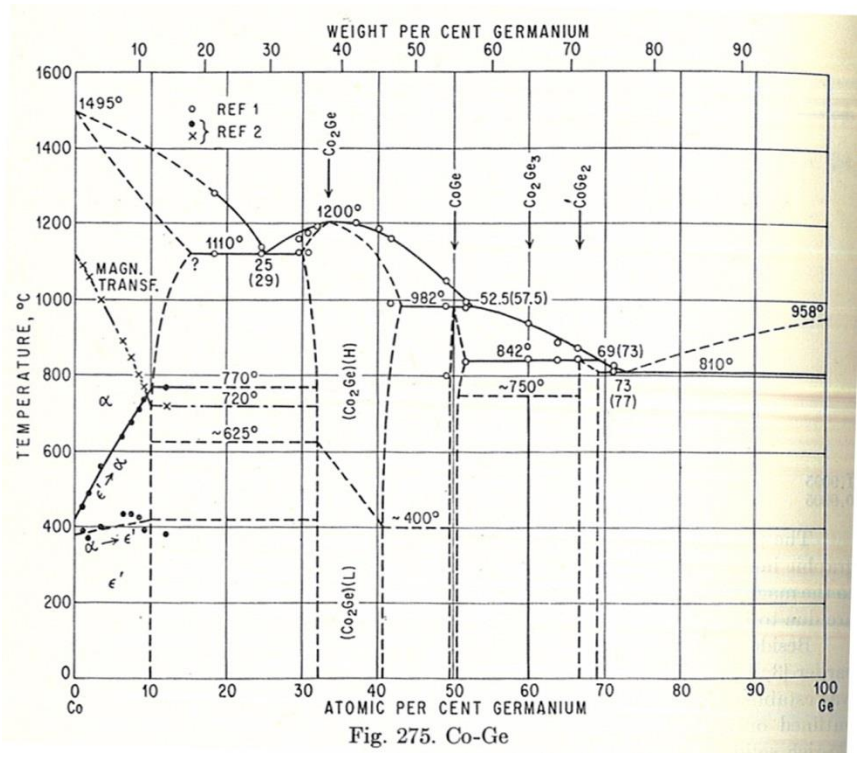

Fig. 275. Co-Ge

Figure 3: Older Phase diagram of Co-Ge binary alloy. Reprinted with permission from [89].

The known physical characteristics of cobalt germanides and some cobalt silicides are summarized in table 2. There are several gaps where no experimental data has been reported. The stability range of the phases, melting and phase change temperatures into liquid and some other solid phase were obtained based on table 1. If the germanide is on top of germanium, germanium will diffuse and react with the germanide to form new phases. Ashburn et al. [91] identified Co_2Ge as the low resistivity phase. As demonstrated in figures 2 & 3, this phase was later found to be Co_5Ge_3 [88], the first phase to form during cobalt germanidation [92]. In a later paper [93], Ashburn et al. identified the low resistivity phase as $CoGe_2$. The later work seems to have more accurate description of the phase given the XRD analysis that was performed that clearly indicated $CoGe_2$. In addition, the authors analyzed the phase that forms after RTA at 300°C and found it to be Co_5Ge_7. Therefore, it is expected that $CoGe_2$ would form at higher temperatures. The resistivity of Co_5Ge_7 was obtained based on the sheet resistance provided by Ashburn et al. [93]. $CoSi_2$ is the phase commonly used as a contact in the industry since it has the lowest resistivity which can be seen in table 2 [67]. It is expected that $CoGe_2$ would also be the lowest resistivity phase most suitable for contacts for

advanced CMOS devices. The study of the other phases has equal importance given the paradigm shift discussed in section 1. In particular, the interface contact resistance could be advantageous for any of the phases, especially if it was possible to grow any of those phases epitaxially on germanium.

Table 2: Physical properties of cobalt germanides and silicides [67]

Phase	Crystal Structure	Lattice Constant (Å)			Stability Range (°C) [88]	T_m (°C)	ρ (μΩ.cm)
		A	B	C			
Co_3Si	Hexagonal	4.976	-	4.069		1207	?
CoSi	Cubic	4.4443	-	-		1427	147
Co_2Si	Orthorhombic	4.918	3.738	7.109		1327	110
$CoSi_2$	Cubic	5.365	-	-		1327	15
α-Co_5Ge_3	Orthorhombic	5.02	3.82	7.26	<382		?
β-Co_5Ge_3 [94, 95]	Hexagonal	3.884	-	5.019	<1210	1210 [84]	?
CoGe (unstable)	Cubic	4.4637	-	-		1250	?
CoGe	Monoclinic [94, 96]	11.648	3.807	4.945	<985	985	65.7 [96]
Co_5Ge_7	Tetragonal	7.64	-	5.81	<806	806 (phase change)	80 [97]/ 91.78 [93]
Co_5Ge_2	Hexagonal	4.06 [98]	-	5.90 [98]	382-636		?
$CoGe_2$	Orthorhombic	5.681	5.681	10.818	<832	832	35.3 [91, 93]/ 40 [97] / 69 [68] / 150.0 [96]
Co_3Ge	Cubic [94]	?	-	-	650-770		?

As seen in table 2, $CoGe_2$ has multiple different values for resistivity [68, 91, 93, 96, 97]. The measurement method is similar for all cases. The difference is due to dependence of resistivity on the crystalline structure of the substrate. In Gaudet et al.'s work [68], the resistivity of $CoGe_2$ was measured on amorphous Ge. Krontiras et al. [96] used a Ge layer evaporated onto an oxidized Si wafer which is likely amorphous as well and Ashburn [91, 93] used an epitaxial Ge (001) substrate. Other groups [99, 100] have experimentally found that the crystallinity of the substrate affects the resistivity of resulting cobalt silicides, with epitaxial silicides having the lowest resistivity. Howell et al. [99] proposed that the effect of agglomeration is the cause of the dependence of silicide resistivity on crystalline structure. In an anneal experiment on single crystal silicon and polycrystalline silicon they found that at temperatures below 650°C, cobalt silicide resistivity was independent of the Si structure but after annealing at 700°C, cobalt silicide resistivity was higher on the polycrystalline Si. The increase in grain size of cobalt silicides in high temperature anneals causes agglomeration, which increases surface roughness resulting in increased resistivity. On polycrystalline substrates the agglomeration effect is increased leading to higher resistivity measurements [99]. The effects of increased resistivity caused by augmented agglomeration on polycrystalline substrates and reduced resistivity on epitaxial substrates would explain the resistivity measurements recorded for $CoGe_2$. The highest resistivity (150 μΩ.cm) corresponds to the most amorphous $CoGe_2$ [96] while the lowest resistivity (35 μΩ.cm) corresponds to $CoGe_2$ grown on an epitaxial Ge substrate [91, 93].

4- Models for Phase Formation Sequence

4.1- Nucleation of a New Phase [67]:

The driving force of the nucleation process in solid state reactions is the reduction in Gibbs free energy due to the creation of a nucleus of the new phase. In case of germanidation, this new phase is created by the interaction of two adjacent parent phases which can be metal, germanide, or germanium to form a nucleus of a new phase of germanide. The total free energy change due to the nucleation can be described using the following equation:

$$\Delta G = ar^3 \Delta g_v + br^2 \Delta\sigma \tag{4.1}$$

where ar^3 and br^2 are the volume and the surface area of the nucleus, respectively. r is the characteristic dimension (e.g. radius), a and b are two geometrical constants determined by the detailed shape of the nucleus, and Δg_v and $\Delta\sigma$ represent, respectively, the Gibbs free energy per unit volume of the new phase and the surface energy change per unit area associated with the creation of the nucleus. Δg_v is a negative quantity and $\Delta\sigma$ is a positive quantity for the formation of a stable compound phase.

The maximum ΔG, denoted ΔG^*, can be found by taking the first derivative of equation (4.1) with respect to r and equating it to zero. ΔG^* is the energy barrier height for the nucleus to overcome to grow spontaneously. ΔG^* is given by:

$$\Delta G^* = \frac{4b^3\Delta\sigma^3}{27a^2\Delta g_v^2} \tag{4.2}$$

and r^*, the minimum radius for the nucleus to grow spontaneously, is given by:

$$r^* = -\frac{2b\Delta\sigma}{3a\Delta g_v} \tag{4.3}$$

The surface energy, σ, doesn't vary significantly between solid phases. It is close to zero for epitaxial interfaces and amount to a maximum of 2 J/m^2 [67]. Δg_v is given by:

$$\Delta g_v = \Delta h_v - T\Delta s_v \tag{4.4}$$

where Δh_v and Δs_v are the enthalpy and entropy of nucleation, respectively. The growth rate of the nucleus, GR, will follow:

$$GR = Cexp\left(-\frac{\Delta G^*}{k_B T}\right) exp\left(-\frac{Q}{k_B T}\right) \tag{4.5}$$

where C is a proportionality constant, k_B is Boltzmann's constant, and Q is the activation energy of diffusion for the diffusing species during germanidation.

If the Gibbs free energy of formation per unit volume, Δg_v, is small, the energy barrier height for nucleation, ΔG^*, is high resulting in difficult nucleation. Even if diffusivity of the diffusing species was high, nucleation can be a rate-limiting step resulting in low density nucleation sites. $\Delta\sigma$ is more or less temperature independent and Δg_v is linearly dependent on temperature. Therefore, ΔG^* is inversely proportional to T^2. The higher the temperature the easier the nucleation of the new germanide phase. When the nucleation is a rate limiting step, the GR is highly temperature sensitive: $GR \propto exp\left(-\frac{1}{T^3}\right)$. No growth happens below a critical temperature. Above that critical temperature, GR of the new phase is very rapid due to the GR dependence on temperature. The resulting interface between the parent phases and the new phase is rough in the case of a nucleation rate limited reaction due to numerous low density nucleation sites which form before growth can start on one of them above the critical temperature. On the other hand, if $\Delta G^*$is low, nucleation happens easily and the resulting interface is smooth. In that case, the reaction is usually diffusion-limited by the diffusing species reaching the reaction interface.

4.2- Effective Heat of Formation Model

The main driving force for the germanidation process to take place is the change in Gibbs free energy. The change in the enthalpy is a good measure of the change in Gibbs free energy for solid state reactions since the change in entropy for such reactions is negligibly low [101]. Therefore, heat of formation can be used to predict phase formation sequence when activation or nucleation barriers do not exist. Solid state reaction is a dynamic non-equilibrium process and it is usually found that only one compound phase forms at a particular interface [101]. This is different from equilibrium systems in which formation of a mixture of phases might lead to the lowest free energy state for the system.

The effective heat of formation (EHF) model [101] is used in the following lines to predict the phase formation sequence in the cobalt germanide system. The heats of formation, ΔH^o in kJ/mol.atom, for different cobalt germanide phases which can form in the Co-Ge binary system are shown in table 3. The most negative heat of formation corresponds to CoGe. Consistent with this, *in situ* XRD measurements by Gaudet et al. [68] in their temperature ramp-up experiment showed that the first phase to form is CoGe. The effective heat of formation model

takes into account the atomic concentration of the various components in order to predict the first phase to form. The effective heat of formation, $\Delta H'$, is given by [101]:

$$\Delta H' = \Delta H^0 \frac{effective\ concentration\ of\ limiting\ element}{compound\ concentration\ limiting\ element} \quad (4.6)$$

where the limiting element is the element that is expected to be completely consumed by the reaction. The compound concentration is the concentration of that element in the compound formed, and the effective concentration is the actual concentration of the element before the reaction.

The effective concentration of interacting species at the growth interface is chosen to be that of the liquidus minimum for reasons that are explained by Pretorius et al. [101]. The limiting element for the reaction is cobalt. The effective concentration of cobalt is 27%. The temperature dependence of the heat of formation is negligible in the case of binary solid reaction so room temperature heat of formation values can be used [101].

Table 3: Heats of formation ΔH^o and effective heats of formation $\Delta H'$ for various cobalt germanides [101]. The $\Delta H'$ values have been calculated at the concentration of the liquidus minimum of the binary system. The number of atoms per unit cell is given in brackets behind each phase.

Phase	Congruency	Composition	ΔH^o (kJ (mol at.)$^{-1}$)	Limiting Element	$\Delta H'$ (kJ (mol at.)$^{-1}$)
Liquidus minimum		$Co_{0.270}Ge_{0.730}$			
Co_5Ge_2 (6)	NC	$Co_{0.714}Ge_{0.286}$	-16.8	Co	-6.35
Co_5Ge_3 (12)	C	$Co_{0.625}Ge_{0.375}$	-19.1	Co	-8.25
CoGe (8 or 16)	NC	$Co_{0.5}Ge_{0.5}$	-17.1	Co	-9.23
Co_5Ge_7 (24)	NC	$Co_{0.417}Ge_{0.583}$	-12.4	Co	-8.03
$CoGe_2$ (24)	NC	$Co_{0.333}Ge_{0.667}$	-5.8	Co	-4.70

Using the effective heat of formation, $\Delta H'$, the effective heat of formation model predicts the first phase to form to be CoGe. However, Pretorius et al. [101] have pointed out that non-congruent phases do not nucleate easily at a moving interface and are usually skipped. This suggests that β-Co_5Ge_3 should be the first phase to form despite

monoclinic CoGe having the lowest effective heat of formation. Our experimental results support this understanding [92]. The contradicting results of Gaudet et al. [68] will be discussed in the next section. If all cobalt reacted to form Co_5Ge_3, and excess Ge still exists, it will react with Co_5Ge_3 to form CoGe which is the next phase to the right of Co_5Ge_3 in the phase diagram. This will be followed by the formation of Co_5Ge_7 and finally $CoGe_2$, which is the last phase to the right in the phase diagram. The model predicts Co_5Ge_2 to form after Co_5Ge_3 formation only if Co is in excess of Ge in the system. It should pointed that the phases as we move to the right in the phase diagram have increasing Ge content and as we move to the left of the phase diagram has increasing Co content.

4.3- Walser-Bené Rule [102]

Walser and Bené postulated that the metal-semiconductor interface, upon deposition, consists of metallic glass with a composition near the lowest temperature eutectic in the binary system. This composition is the most stable in a supercooled state and, therefore; it is expected to be the concentration where a finite cluster of atoms or a thin layer may be thermodynamically stable with respect to recrystallization [102]. As the temperature increases, the atoms near the interface diffuse to form a metallic glass according to the previous postulate until the region is metastable and nucleation of the first phase starts.

Walser and Bené (WB) proposed a rule that predicts the first phase that nucleates in planar binary reaction couples. The rule states that: "*The first compound nucleated in planar binary reaction couples is the most stable congruently melting compound adjacent to the lowest-temperature eutectic on the bulk equilibrium phase diagram*" [102]. Congruently melting compounds are compounds which do not change composition when they melt into a liquid state. "Most congruently stable" refers to the adjacent solid phase with highest melting temperature. Congruently melting states are expected to be favored over noncongruent states because of: "*a higher energy barrier associated with the large rearrangement in short-range order (SRO) required to go from a liquidlike SRO to the crystalline SRO for noncongruent states at the same concentration.*" [102] In contrast, congruently melting states require much smaller change of SRO.

WB rule is purely empirical and 80-90% successful in predicting the first nucleated phase [103]. The WB rule statement mentioned above is generally valid for the metal-elemental semiconductor systems. Later, Bené extended

the WB rule to metal-metal systems by relaxing the requirement that the first phase that forms needs to be congruent [104]. As stated by Bené, the metal-metal systems rule states that: "*first phase nucleated in metal-metal thin-film reactions is the phase immediately adjacent to the low-temperature eutectic in the binary phase diagram*".

WB rule predicts that Co_5Ge_3 is the first phase to nucleate in the planar binary reaction between cobalt and germanium. Wittmer et al. [105] concluded that their experimental results support WB rule since low temperature germanidation resulted in Co_2Ge (Co_5Ge_3). Higher temperatures resulted in different phases. However, Wittmer et al. did not monitor the forming phases in-situ. Our recent in-situ experimental results support the prediction of WB rule [92] and confirm the conclusion of Wittmer et al [105].

4.4- Cobalt Germanidation Growth Kinetics Model [106]

Cobalt germanidation is expected to proceed similar to silicidation reaction due to the similarities between the two phenomena. The linear-parabolic Deal-Grove model has been used to describe silicide growth [1]. The same model can be used to describe germanide growth as well. Both WB and EHF models unambiguously predict the first phase to nucleate in binary solid reactions. They both predict the first phase to form to be Co_5Ge_3 as explained above. This was supported by our experimental results [92]. Ge is the diffusing species in the cobalt germanidation reaction [107]. The formation of Co_5Ge_3 occurs by diffusion of Ge through the forming Co_5Ge_3 and the reaction of Ge and Co at the Co_5Ge_3-Co interface to form new Co_5Ge_3 [107]. In the presence of excess Ge, the next phase to form according to the EHF model is CoGe. This phase starts to nucleate when all the Co is consumed or the Co_5Ge_3 layer causes germanidation to become diffusion limited. CoGe and Co_5Ge_3 coexist in this binary system until all the Co is consumed and the remaining Co_5Ge_3 is converted to CoGe which is then converted to Co_5Ge_7 and $CoGe_2$ in further reactions if the temperature is high enough to activate such reactions. The cobalt germanidation process as we have described it here is illustrated in figure 4. Figure 4 omits the effect of ambient on the germandiation reaction. In air ambient, Co undergoes an oxidation reaction at the air exposed surface leading to premature formation of CoGe due to consumption of Co by the formation of both oxide and Co_5Ge_3.

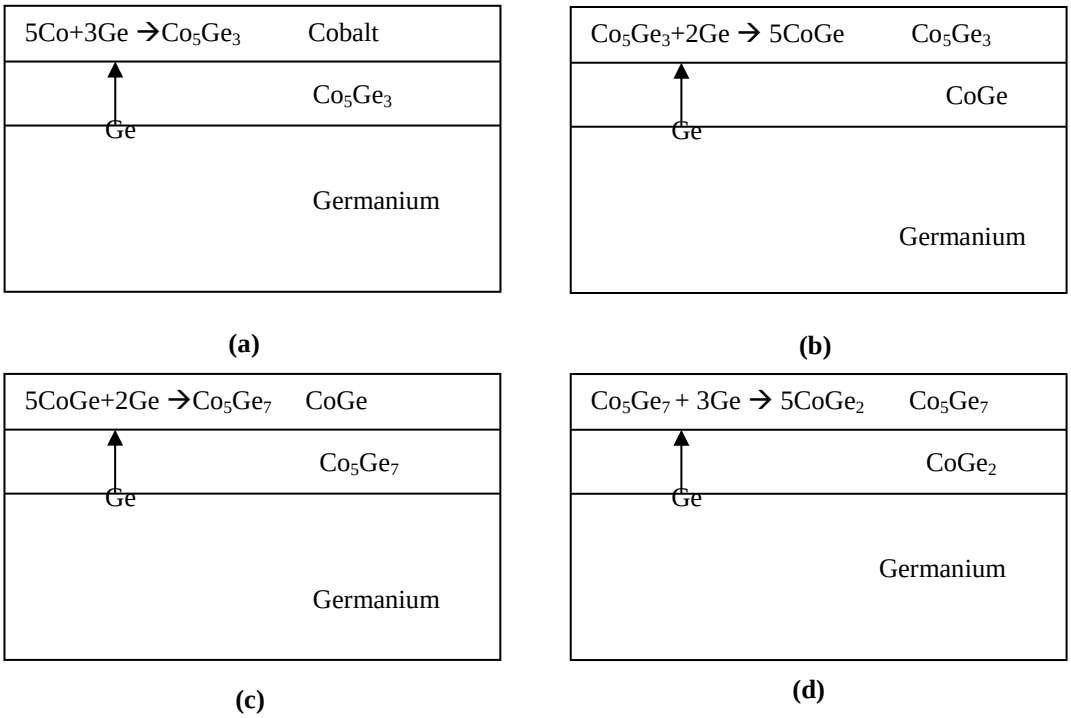

Figure 4: Illustration of cobalt germanidation: (a) first phase to form is Co_5Ge_3. It forms by diffusion of germanium through germanide forming new germanide through a reaction at the CoGe/Co interface. (b) Second phase to form is CoGe. It forms when Co_5Ge_3 is consumed. CoGe results from the reaction of Co_5Ge_3 and Ge at the reaction interface. (c) Third phase to form is Co_5Ge_7. It forms when CoGe is consumed. Co_5Ge_7 results from the reaction of CoGe with Ge. (d) Fourth phase to form is $CoGe_2$. It forms when Co_5Ge_7 is consumed. $CoGe_2$ results from the reaction of Co_5Ge_7 with Ge.

Four reactions take place during cobalt germanidation [106]:

$$\frac{5}{3}Co + Ge \xrightarrow{k_1} \frac{1}{3}Co_5Ge_3 \tag{4.7}$$

$$\frac{1}{2}Co_5Ge_3 + Ge \xrightarrow{k_2} \frac{5}{2}CoGe \tag{4.8}$$

$$\frac{5}{2}CoGe + Ge \xrightarrow{k_3} \frac{1}{2}Co_5Ge_7 \tag{4.9}$$

$$\frac{1}{3}Co_5Ge_7 + Ge \xrightarrow{k_4} \frac{5}{3}CoGe_2 \tag{4.10}$$

This leads to a system of diffusion-reaction equations [106]:

$$\frac{\partial C_{Co}}{\partial t} = -\frac{5}{3} k_1 \frac{C_{Co}}{C_{Co0}} C_{Ge} \tag{4.11}$$

$$\frac{\partial C_{Ge}}{\partial t} = \nabla.(D_{Ge} \nabla C_{Ge}) - k_1 \frac{C_{Co}}{C_{Co0}} C_{Ge} - k_2 \frac{C_{Co_5Ge_3}}{C_{Co_5Ge_3 0}} C_{Ge} - k_3 \frac{C_{CoGe}}{C_{CoGe0}} C_{Ge} - k_4 \frac{C_{Co_5Ge_7}}{C_{Co_5Ge_7 0}} C_{Ge} \tag{4.12}$$

$$\frac{\partial C_{Co_5Ge_3}}{\partial t} = \frac{1}{3} k_1 \frac{C_{Co}}{C_{Co0}} C_{Ge} - \frac{1}{2} k_2 \frac{C_{Co_5Ge_3}}{C_{Co_5Ge_3 0}} C_{Ge} \tag{4.13}$$

$$\frac{\partial C_{CoGe}}{\partial t} = \frac{5}{2} k_2 \frac{C_{Co_5Ge_3}}{C_{Co_5Ge_3 0}} C_{Ge} - \frac{5}{2} k_3 \frac{C_{CoGe}}{C_{CoGe0}} C_{Ge} \tag{4.14}$$

$$\frac{\partial C_{Co_5Ge_7}}{\partial t} = \frac{1}{2} k_3 \frac{C_{CoGe}}{C_{CoGe0}} C_{Ge} - \frac{1}{3} k_4 \frac{C_{Co_5Ge_7}}{C_{Co_5Ge_7 0}} C_{Ge} \tag{4.15}$$

$$\frac{\partial C_{CoGe_2}}{\partial t} = \frac{5}{3} k_4 \frac{C_{Co_5Ge_7}}{C_{Co_5Ge_7 0}} C_{Ge} \tag{4.16}$$

where C_{Co0} is the number of atoms per unit volume in cobalt, C_{i0} is the number of molecules per unit volume in the pure phase i, i = Co_5Ge_3, CoGe, Co_5Ge_7, C_i is the actual instantaneous concentration of a given material (Co, Ge, or one of the germanide phases) and these are the solution variable, and k_1-k_4 are the reaction rates, which have an Arrhenius dependence on temperature:

$$k_x = k_{x0} e^{\frac{-E_A}{k_B T}} \tag{4.17}$$

where E_A is the activation energy for interface reaction, and k_{x0} is the pre-exponential reaction rate constant.

The system of equations (4.11)-(4.16) could be solved by considering the appropriate boundary conditions as well as the cobalt volume consumed as discussed elsewhere [106]. The model has been calibrated to experimental data and the reaction rates were obtained as shown in figure 5. After calibration, the model was successfully able to predict the phase formed in a number of different experimental conditions [106].

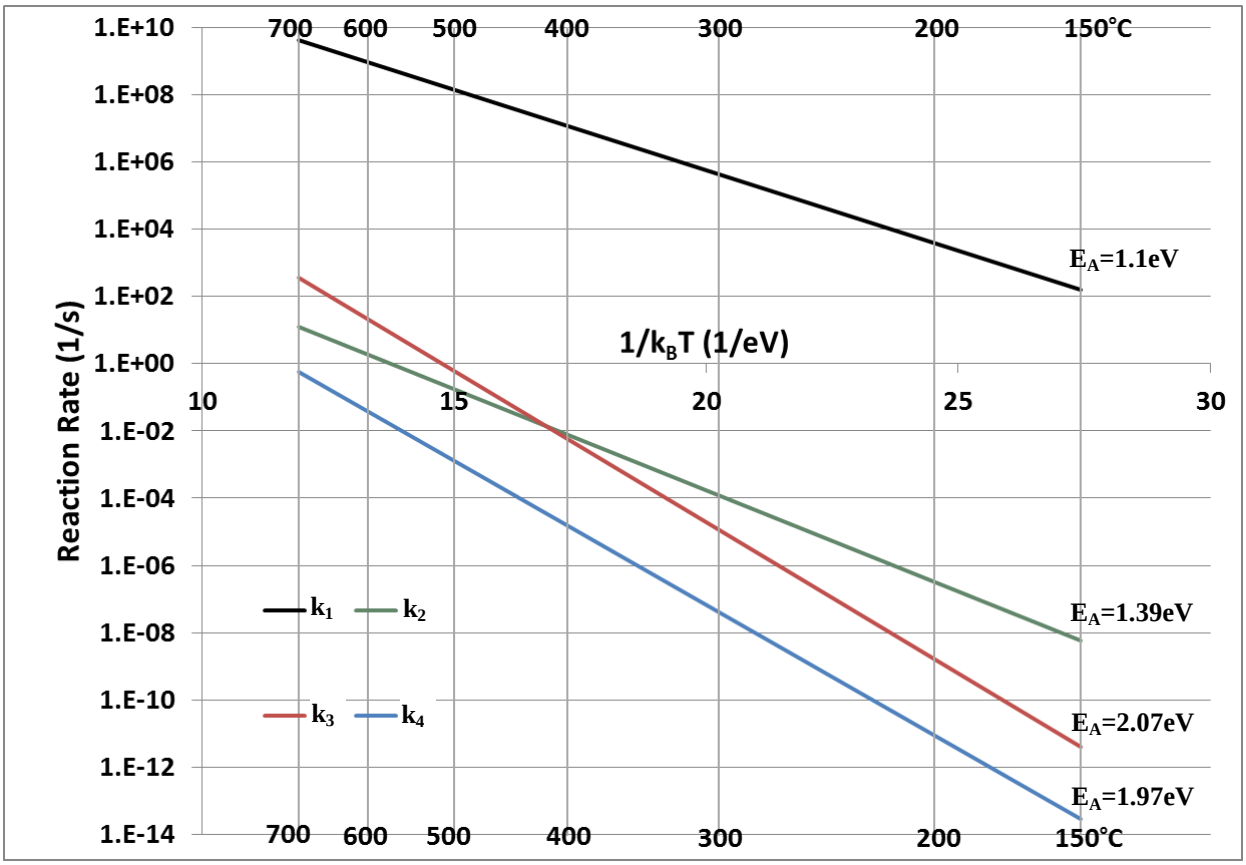

Figure 5: Reaction rate constants Arrhenius dependence

5- Experimental Phase Formation Sequence of Cobalt Germanides

In this section, we survey experimental work on the identification of phases that result from thermal cobalt germanidation. Identification of phase transformation requires in-situ observation of phases forming during the germanidation process. An accurate design for a germanide contact requires a thorough understanding of the phases that form and their transformation during the germanidation process.

Table 4: Cobalt germanide phases forming by reactive deposition at constant temperature.

#	Temp. (°C)	Pressure and Method	Time and Method	Cobalt Thickness (nm)	Germanium Orientation	Germanide Phase	Ref.
1	RT	$<10^{-9}$ Torr	0.005 A/s MBE	0.7, 1.5 ML	111	$CoGe_2$ and Co_5Ge_7 (possibly)	[108]
2	RT	$<10^{-9}$ Torr	0.005 A/s MBE	5, 10 ML	111	$CoGe_2$ and bcc-Co	[108]
3	RT	$4X10^{-9}$ Torr	E Beam Evaporation	3 ML	111	Possible CoGe	[109]
4	300	10^{-5} Pa	e-beam, Ge and Co sequential deposition at HT	N/A	(100)-Ge epitaxial layer on top of (100)-GaAs	CoGe	[110]
5	300-400	4.2 Torr in N_2 ambient	CVD (GeH_4 reacted with Co layer)	3.5	50nm SiO_2 on Si(100)	$CoGe_2$	[111]
6	350	$<10^{-9}$ Torr.	3h	Reactive Deposition	100	Co_5Ge_7	[112]
7	350-500	4.2 Torr in N_2 + GeH_4	CVD (GeH_4 reacted with Co	7	50nm SiO_2 on Si(100)	$CoGe_2$	[111]

			layer)				
8	400	10^{-5}Pa	e-beam, Ge and Co sequential deposition at HT	Ge:Co=2:1	(100)-Ge epitaxial layer on top of (100)-GaAs	Co_5Ge_7	[110]
9	500	10^{-5}Pa	e-beam, Ge and Co sequential deposition at HT	Ge:Co=2:1	(100)-Ge epitaxial layer on top of (100)-GaAs	Co_5Ge_7	[110]
10	500	$<10^{-7}$ Pa	Reactive Deposition (e-beam)	<1ML	7ML Ge on Si(100)	$CoGe_2$	[113]
11	600	10^{-5}Pa	e-beam, Ge and Co sequential deposition at HT		(100)-Ge epitaxial layer on top of (100)-GaAs	$CoGe_2$	[110]
12	670	Vacuum	Reactive Deposition (e-beam)	2	100	$CoGe_2$ and CoGe	[114]
13	670	Vacuum	Reactive Deposition (e-beam)	2	5 um Ge on Si (100)	$CoGe_2$, CoGe and Co_5Ge_7 (this one seems to be induced by defects)	[114]

Table 4 provides data on reactive deposition experiments. Tsuruta et al. [108] have observed interfacial cobalt germanide at room temperature on (111) germanium. In this specific experiment slower deposition rate MBE was used for Co deposition rather than sputtering. The germanide is only found at the Co/Ge interface. MBE is a controlled deposition technique that is very slow compared to sputtering. The deposited Co atoms react with Ge and form an interfacial germanide layer before more Co atoms are deposited. Subsequent to the formation of the interfacial layer there is no further germanide growth because at room temperature there would be almost no diffusion of Ge through the germanide to react with Co. The germanide phase reported was $CoGe_2$. This is the final stable phase predicted by the EHF model as discussed in section 4. Given the very slow deposition rate, Co atoms are consumed in germanidation and germanium abundance causes the formation of a Ge rich phase. This might be happening through multiple sequential reactions as predicted by the EHF model. This theory is supported by the existence of traces of Co_5Ge_7 phase [108] that have not fully reacted to form the final stable phase, $CoGe_2$. A different group used e-beam evaporation which has a deposition rate faster than MBE but slower than Sputtering. They observed interfacial CoGe [109] at room temperature. This continued to be the dominant phase for e-beam evaporation up to 300°C [110]. Given the faster rate of deposition compared to MBE, more Co is available to react with Ge and the CoGe phase does not react further with the interfacial Ge forming the next phases.

A low deposition rate reactive deposition epitaxy of a metal on germanium or silicon yields a semiconductor-rich phase rather than a metal-rich phase [115, 116]. Similar to the room temperature results reported above, high temperature reactive deposition also results in Ge-rich phases. Co_5Ge_7 is the dominant phase in reactive deposition experiments conducted at 350°C [112]. Co_5Ge_7 continues to be the dominant phase for temperature as high as 500°C [110]. In a different experiment, $CoGe_2$ was the resulting phase at 500°C [113]. Although both groups: [110] and [113] performed their experiment at 500°C, the experimental setup was quite different. Shi et al. [110] performed co-deposited both Co and Ge using e-beam evaporation on a GaAs wafer. On the other hand, Goldfarb et al. [113] deposited Co on a strained 7 monolayers of Ge on top of a Si substrate using e-beam evaporation as well. One possibility could be that the compressive strain in the Ge layer enhanced the germanidation rate resulting in the final phase of $CoGe_2$ instead of Co_5Ge_7 in case of Goldfarb et al. [113]. A more careful study is needed to understand the effect of strain in the Ge on the germanidation rate. $CoGe_2$ is the dominant phase at higher temperatures of 600°C

and above. Ewert et al. [114] observed through in-situ micro-LEED (Low Energy Electron Diffraction) that traces of CoGe and Co_5Ge_7 continue to exist even at temperatures as high as 670°C. This indicates that reactive deposition might not be the optimum technique for forming a stable single-phase contact. Solid state anneal is needed to achieve a single-phase high quality contact. In case of GeH_4 gas reacting with a deposited film of Co, the resulting phase was $CoGe_2$ [111]. This can be attributed to the abundance of Ge at the reacting interface without any diffusion requirements causing the direct formation of the Ge rich phase $CoGe_2$ even at temperatures as low as 300°C. $CoGe_2$ was the resultant phase for thicker cobalt layer of 7 nm reacting with GeH_4 gas up to a temperature of 500°C. $CoGe_2$ is the expected phase to form at higher temperatures (>500°C) in such setup in which GeH_4 is reacted with a Co film.

Deposition of a Co film followed by thermal annealing is different from reactive deposition. Table 5 provides data on solid state anneals under constant temperature whereas table 6 provides the same data for ramped anneals.

Table 5: Cobalt germanide phases forming by solid state anneals at constant temperature.

#	Temp. (°C)	Pressure	Time	Cobalt Thickness (nm)	Germanium Orientation	Germanide Phase	Ref.
1	150	Ultrahigh Vacuum (UHV)	60 min	4 ML (~1.7 nm)	100	No germanide	[117]
2	≤200	Atm.	20 hr	100-150	100	No germanide	[105]
3	≤200	10^{-6} Torr.	1 hr	30	111	No germanide	[33]
4	≤200	Vacuum: 10^{-3} Torr.	48 hr	30	100	No germanide	[92]
5	220	10^{-6} Torr.	1 hr	30	111	Weak XRD signals of CoGe or Co_5Ge_3	[33]
6	227	Vacuum: 10^{-3} Torr.	24 hr	30	100	β-Co_5Ge_3	[92]

7	227	Vacuum: 10^{-3} Torr.	48 hr	30	100	β-Co_5Ge_3	[92]
8	227	Atm.	48 hr	30	100	Monoclinic CoGe	[92]
9	250-400	UHV	1 hr	4 ML (~1.7 nm)	100	CoGe or Co_5Ge_3 (probable)	[117]
10	250	Atm.	1-20 hr	100-150	100	Co_5Ge_3 (Reported Co_2Ge shown in a later phase diagram study [16] to be Co_5Ge_3)	[105]
11	280-500	10^{-6} Torr.	1 hr	30	111	Co_5Ge_7	[33]
12	300-350	Atm.	1-20 hr	100-150	100	Co_5Ge_3 (Co_2Ge) + CoGe	[105]
13	300-400	UHV	10 sec	30	100	Co_5Ge_7	[93]
14	300-425	Atm Ar ambient	30 min	30nm	100	Co_5Ge_7 (probable)	[118]
15	300	UHV	26.5 hr	6nm	Ge (100)	Co_5Ge_7	[119]
16	350	Atm. H_2-N_2 ambient	30 min	50	100 nm Ge on GaAs	CoGe (confirmed) and Co_5Ge_7 (Possible based on XRD profile)	[81]
17	350	UHV	0.5 hr after 47 hr anneal at 325	6	Ge (100)	Co_5Ge_7	[119]
18	350	Atm N_2	3 hr	4	50nm Ge	CoGe or Co_5Ge_7	[120]

		ambient			evaporated onto 400nm of SiO2 on Si	(probable)	
19	375	Atm N_2 ambient	3 hrs	4	50nm Ge evaporated onto 400nm of SiO_2 on Si	$CoGe_2$ (probable)	[120]
20	400	$<10^{-7}$ Pa	1 hr	2-3 ML	7 ML Ge on Si(100)	Co_5Ge_7	[113]
21	400	$<10^{-7}$ Pa	10 hr	2-3 ML	7 ML Ge on Si(100)	Co_5Ge_7 and $CoGe_2$	[113]
22	400-600	Atm.	1 hr	4 ML (~1.7nm)	100	Co_5Ge_7 (probable)	[117]
23	400-450	Atm., $8X10^{-7}$ Torr.	1-20 hr, 30 min	100-150, 70	Likely amorphous	CoGe	[96], [105]
24	425	Atm. H_2-N_2 ambient	30 min	50	100 nm Ge on 50 nm Co on GaAs	CoGe and Co_5Ge_7 (XRD confirmed)	[81]
25	425	Atm. H_2-N_2 ambient	30 min	50	150 nm Ge on GaAs	$CoGe_2$	[81]
26	425-500	UHV	10 sec	30	100	Co_5Ge_7 + $CoGe_2$	[91, 93]
27	425-600	Atm. Ar ambient	10 sec	30	200 nm Ge deposited on Si 100	$CoGe_2$	[93]
28	425-600	Atm Ar	30 min	30 nm	100	$CoGe_2$ (probable)	[118]

		ambient					
29	427	$5x10^{-10}$ Torr	Deposited at 427°C then post annealed at 427°C for 10 min	90 ML	100	$CoGe_2$	[115]
30	450	Atm N_2 ambient	60 sec	30	100	$CoGe + Co_5Ge_7$	[97]
31	500	Vacuum	1 min	30	100	Co_5Ge_7	[92]
32	500-600	Atm.	1-20 h	100-150	100	$CoGe_2 + CoGe$	[105]
33	550	Atm. N_2 ambient	1 min	30	100	Co_5Ge_7	[97]
34	600	UHV	10 sec	30	100	$CoGe_2$	[91, 93]
35	600	Atm.	1 hr	4 ML (~1.7 nm)	100	$CoGe_2$	[117]
36	600-700	10^{-6} Torr.	1 hr	30	111	$CoGe_2$	[33]
37	600-750	Atm., Vacuum	10 sec – 1 hr	30-70	100, 111	$CoGe_2$	[33]
38	650-750	$8X10^{-7}$ Torr.	1 hr	70	400 nm of Ge evaporated onto Si wafer.	$CoGe_2$	[96]
39	700	10^{-8} Torr	40 min	22-25	(100) cleaned at 700C for 1 hr before	$Co_5Ge_7 + CoGe2$	[121]

					deposition		
40	700	Atm. N_2 ambient	1 min	30	100	$CoGe_2$	[97]
41	700	10^{-7} Torr	40 min	22	100	$CoGe_2$: Degrades due Co in-diffusion	[72]
42	700	10^{-7} Torr	120 min	22	100	$CoGe_2$: Concentration decreases with anneal time	[72]

Table 6: Cobalt germanide phases forming in different experimental conditions during temperature ramp anneals.

#	Temp. (°C)	Pressure	Time	Cobalt Thickness (nm)	Germanium Orientation	Germanide Phase	Reference
1	100-400	Atm. He flow	3°C/s ramp	30	Poly-Ge	No germanide	[122]
2	100-400	Atm. He flow	3°C/s ramp	30	Amorphous	No germanide	[122]
3	100-310	Atm. He flow	3°C/s ramp	30	Amorphous	No germanide	[68]
4	100-395	Atm. He flow	3°C/s ramp	30	100	No germanide	[68]
5	100-411	Atm. He flow	3°C/s ramp	30	100	No germanide	[122]
6	310-410	Atm. He flow	3°C/s ramp	30	Amorphous	CoGe	[68]
7	340-450	Atm. He flow	3°C/s ramp	30	100	CoGe	[123]
8	395-450	Atm. He flow	3°C/s ramp	30	100	CoGe	[68]

9	400-439	Atm. He flow	3°C/s ramp	30	Amorphous	CoGe	[122]
10	400-451	Atm. He flow	3°C/s ramp	30	Poly-Ge	CoGe	[122]
11	410-575	Atm.	3°C/s ramp	30	Amorphous	Co_5Ge_7	[68]
12	411-462	Atm. He flow	3°C/s ramp	30	100	CoGe	[122]
13	439-825	Atm. He flow	3°C/s ramp	30	Amorphous	$CoGe_2$	[122]
14	450-650	Atm. He flow	3°C/s ramp	30	100	Co_5Ge_7	[123]
15	450-655	Atm. He flow	3°C/s ramp	30	100	Co_5Ge_7	[68]
16	451-575	Atm. He flow	3°C/s ramp	30	Poly-Ge	Co_5Ge_7	[122]
17	462-684	Atm. He flow	3°C/s ramp	30	100	Co_5Ge_7	[122]
18	575-825	Atm.	3°C/s ramp	30	Amorphous alpha phase	$CoGe_2$	[68]
19	575-825	Atm. He flow	3°C/s ramp	30	Poly-Ge	$CoGe_2$	[122]
20	650-820	Atm. He flow	3°C/s ramp	30	100	$CoGe_2$	[123]
21	655-825	Atm.	3°C/s ramp	30	100	$CoGe_2$	[68]
22	680-820	Atm. He flow	3°C/s ramp	30	111	$CoGe_2$	[123]
23	684-806 (Melting)	Atm. He flow	3°C/s ramp	30	100	$CoGe_2$	[122]

Tables 5 and 6 show the large volume of work that has been done in this area and the wide range of results that have been obtained for different experimental conditions. Analysis of these data yields a number of key observations.

The onset temperature of inward diffusion of cobalt into the underlying bulk Ge(100) is 150°C compared to 350°C for diffusion of cobalt into bulk Si(100) [124]. Therefore, it is expected that the formation temperatures of cobalt germanides are lower than the formation temperatures of the corresponding cobalt silicides. No bulk germanide formation is expected for solid state anneals below 150°C. In addition, the equilibrium concentrations of interstitials and vacancies are higher in Ge than in Si at the same temperature [124]. Cobalt has been shown to

diffuse faster in Ge(100) than in Si(100) up to 750°C. While Ge is the dominant diffusing species in the cobalt germanidation reaction [107], the reaction starts by Co diffusing into Ge [97]. Further germanide growth happens with Ge diffusing through the germanide layer to react with Co forming new layers of the germanide.

No bulk germanide formation has been detected experimentally at or below 200°C [33, 92, 105, 117]. This is true for both (100) and (111) germanium and it is also true for atmospheric and low pressure. To confirm this, we conducted long time anneal experiments for 48 hours and confirmed that no germanide forms at or below 200°C for (100) germanium even for such long time anneal [92]. No experiments have been reported for (110) germanium. Also, no experiments have been done for poly-Ge or amorphous-Ge at constant temperature to obtain the formation temperature of the first germanide.

Interfacial reactions were found to start to occur between cobalt and (111) germanium at 220°C [33] and between cobalt and (100) germanium at 225°C [119]. Hsieh et al. [33] reported weak XRD signals of a germanide after one hour anneal at 220°C in low pressure vacuum. The authors indicated that the forming phase likely matches CoGe or Co_5Ge_3. The phase was not confirmed since the XRD signal was weak. Grzela et al. [117] observed the nucleation of ordered nanocrystals after annealing 4 monolayers deposited on (100) Ge for one hour at 250°C. Those ordered nanocrystals start to form islands of rectangular shape and grow at random places of the surface. In addition, Ge terrace structure morphology, which was initially visible, disappears after anneal. Those results indicate the onset of Co-Ge reaction. The authors pointed that the probable phase that formed at this annealing temperature was CoGe [113] based on Gaudet et al. experiment [68].

Our group conducted in-situ long-time anneal study [92] to find the first phase to form during cobalt germanidation. The experimental results confirmed the models' prediction: first phase to form was Co_5Ge_3. This phase was confirmed at temperatures as low as 227°C. Those results are in agreement with previous constant temperature anneal experiments [105]. Our experimental results also indicate the formation of CoGe in case of annealing in atmospheric environment in the same temperature range. CoGe forms when Co is consumed in germanidation and Ge is available to react with Co_5Ge_3. Those results show that the temperature range at which CoGe forms is similar to that of Co_5Ge_3. CoGe was also the second phase observed by Wittmer et al. [105] in their

long time anneal experiments at temperatures as high as 350°C. CoGe was also detected at 350°C with Co thickness of 50 nm on a limited Ge thickness of 100 nm [81]. Co_5Ge_7 couldn't be ruled out in this case. Co_5Ge_7 is the most stable phase at this temperature (350°C) as will be discussed later. However, Co rich phase is more likely with the limited Ge presence. N_2 ambient seems to slow down the germanidation reaction [81, 97]. Park et al. [97] claimed the phase forming at 300°C to be CoGe despite presence of Co as indicated by TEM. This claim was only supported by referring to previous ramp-up experiments and has no support from XRD spectra as reported by the researchers.

For ramp-up experiments, the first phase detected is monoclinic CoGe [68, 122]. The authors ramped up the temperature at a rate of 3°C/sec. This fast rate doesn't allow the reaction to stabilize and, therefore, resulted in not detecting the Co_5Ge_3 phase as well as higher nucleation temperatures than those of constant temperature experiments. The nucleation/formation temperature for monoclinic CoGe was 400°C on poly-Ge. Two nucleation/formation temperatures were reported for amorphous-Ge: 400°C [122] and 310°C [68]. Opsomer et al. [122] attributed the discrepancy between the two works in the nucleation temperature to the method of preparation of the amorphous germanium substrates. Opsomer et al. thermally evaporated germanium, while Gaudet et al. [68] sputtered the Ge. The different amorphous-Ge preparation techniques can lead to differences in the microstructures of the Ge layers: density, porosity, and impurity content [122]. Such differences in the microstructures may have also contributed to the bypassing of the Co_5Ge_7 phase in case of Opsomer et al.'s experiment as suggested by the authors. It is possible that Co_5Ge_7 had formed but wasn't detected due to a small temperature window before its transformation to $CoGe_2$.

The EHF model predicts Co_5Ge_7 to be the third phase to form after CoGe. Those 2 phases: CoGe and Co_5Ge_7 coexist if the germanium content was not high enough to react with CoGe forming Co_5Ge_7. This was the case observed by Koltin et al.[81] with a limited Co content that also reacted with GaAs at 425°C. Another possibility for slowing down the reaction would be the N_2 ambient which was used by Koltin et al. [81] as well as Park et al. [97]. The two phases CoGe and Co_5Ge_7 also coexisted in case of N_2 atmospheric anneal for 60s at 450°C [97]. Co_5Ge_7 starts to form at 280°C on (111) Ge [33] after 1 hour anneal and starts to form on (100) Ge [93] after a very short anneal of 10 seconds at 300°C and continues to be the dominant phase after a 26.5 hrs anneal at 300°C [119]. We can conclude that Co_5Ge_7 is the most stable phase in this temperature range 280-300°C. Co_5Ge_7 continues to be the

dominant phase up to 500°C on (111) Ge [33] and 425°C on (100) Ge [93, 118]. Co_5Ge_7 is a Ge rich phase. Co_5Ge_7 is also the only phase seen after 1 minute anneal in atmospheric N_2 ambient [97]. It forms more favorably at lower temperatures on (111) Ge given the higher surface density of Ge atoms in that crystal orientation.

$CoGe_2$ is the final and most stable phase to form during cobalt germanidation. It starts to form in a solid state anneal reaction at 400°C [113] on (100) Ge for long time anneals and more commonly seen for short time anneals at 425°C [81, 91, 93, 118]. It initially coexists with Co_5Ge_7 at lower temperatures [91, 93]. It continues to be the dominant phase for temperatures as high as 825°C [68]. Co_5Ge_7 is expected to be seen in vacuum for short time anneals on (100) Ge for temperatures as high as 500°C [92] and it continues to exist at 700°C when very low pressure is used (10^{-8} Torr) [121]. Wittmer et al. [105] reported CoGe to coexist with $CoGe_2$ for temperatures as high as 600°C. However, it is more likely that the phase observed was actually Co_5Ge_7 since they didn't report the Co_5Ge_7 in their study and given that the XRD spikes of both phases are close and may have not been considered by the authors. Prolonged anneal at temperatures as high as 700°C results in decomposition of $CoGe_2$ and indiffusion of Co into Ge degrading the quality of Ge [72]. Similar decomposition of $CoGe_2$ and indiffusion of Co has been confirmed by DLTS measurements for RTA anneal at 750°C [85]. Indiffusion of Co has also been seen in RTA germanidation experiments conducted at 600°C [71]. Substitutional Co introduces an acceptor peak at E_c-0.33eV [71]. Those deep level defects might form an inversion layer near the germanide-germanium interface [125] affecting the SBH as will be discussed later. DLTS measurements didn't show any interstitial Co in RTA experiments at temperatures below or equal to 500°C [85]. The concentration of substitutional Co was higher than the expected vacancy concentration and well lower than the solid solubility of Co in Ge [71]. Since substitutional Co mainly diffuses by a vacancy assisted mechanism, the Co traps concentration indicates that vacancies are injected into Ge during the germanidation process [71]. This is consistent with the fact that Ge is the main diffusing species during cobalt germanidation. For RTA ramp-up germanidation, minority carrier introduced due to Co metal defects peaks at 650°C [87]. Another effect that takes place at higher temperature (>=750°C) is agglomeration of $CoGe_2$ [97] which is expected to increase the resistivity of the germanide as well as the leakage current.

The phase sequence in cobalt germanidation in ramp-up experiments follows the expectations of the EHF model. CoGe is the first phase detected followed by Co_5Ge_7 and finally $CoGe_2$. As explained previously the Co_5Ge_3

phase was likely skipped because of the fast ramp-up rate which doesn't help the reaction to stabilize. The fast ramp-up rate also has the effect of increasing the germanide formation temperature as noted in table 7. The temperature range for each of those phases depends on the crystalline structure of Ge as well as its forming methodology. The transformation temperatures for cobalt germanides are lowest for amorphous germanium, then poly-crystalline germanium, and then single crystalline germanium with the exception of CoGe on poly-Ge. The temperature ranges are different for different groups even when the crystalline structure of Ge was the same. The transformation temperatures were higher for (100) Ge prepared by Opsomer et al.'s group [122] compared to that prepared by De Keyser et al.'s group [123]. Opsomer et al. used Ge-on-insulator (GOI) for the single crystalline Ge, while De Keyser et al. used single crystalline (100) and (111) Ge. Opsomer et al.'s group didn't give the details of their wafer. It is possible that Ge was thin enough to have tensile strain [126] which affected the transformation temperatures by retarding the reaction similar to the effect of strain on silicidation. The effect of strain in the Ge wafer on the formation of the germanide has not been studied and will need further investigation. However, strain is expected to have some effect on the reaction rates and transformation temperatures as in the case of silicidation [127]. The differences between the transformation temperatures in case of amorphous Ge have been discussed previously. The temperatures ranges for each phase are summarized in table 7. Table 7 could help to design the process to obtain a specific phase using ramp-up anneal.

Table 7: Formation temperature ranges reported for each cobalt germanide phase on different germanium crystal orientations formed by ramp up anneal temperature experiments.

Crystal Orientation	Germanide Phase	Temperature Range of phase (°C)
(100)	CoGe	340 [123] - 462 [122]
(100)	Co_5Ge_7	450 [123] - 684 [122]
(100)	$CoGe_2$	650 [123] - 825 [68]
(110)	No Data	
(111)	CoGe	No Data
(111)	Co_5Ge_7	No Data
(111)	$CoGe_2$	680-820 [123]
Poly-Ge	CoGe	400-451 [122]
Poly-Ge	Co_5Ge_7	451-575 [122]
Poly-Ge	$CoGe_2$	575-825 [122]
Amorphous Ge	CoGe	310 [68] - 439 [122]
Amorphous Ge	Co_5Ge_7	410 [68] - 575 [68]
Amorphous Ge	$CoGe_2$	439 [122] - 825 [68]

The experimental results discussed in this section give some guidance in the process design of the contact formation. Three methods have been discussed: a) reactive deposition, b) solid-state anneal at a constant temperature, and c) ramp-up solid state anneal. $CoGe_2$ is assumed to be the low resistivity phase by the industry analogous to $CoSi_2$. Co_5Ge_3 and CoGe couldn't be excluded as possible low resistivity phases since both phases are highly ordered polycrystalline phases [92]. Co_5Ge_3 forms only two in-plane orientations with the principal axis [0 -1 0] and CoGe forms four in-plane orientations with principal axis [-1 1 1] during germanidation [92]. Further studies are needed to understand the resistivities of those phases. Reactive deposition can be used to obtain the low resistivity phase even at room temperature using slow deposition techniques like MBE. The forming germanide in that case is only interfacial. The thickness of liner germanide couldn't be controlled using RT reactive deposition. The thickness

could be controlled using reactive deposition at higher temperatures. Careful examination of the phases forming using reactive deposition indicated that mixed phases exist [114] even at temperatures as high as 670°C temperature degrading the quality of the germanide. Solid state anneal could be used to obtain the low resistivity phase at temperatures as low as 425°C. The low resistivity phase forms at rather high temperatures in case of ramp-up anneals: 650°C and above. Solid state anneal seems, therefore, to be the optimum choice for contact formation. It has to be emphasized that such low formation temperature: 425°C is advantageous for cobalt germanides, if they were to be used in state-of-art FinFETs, since it lies within the typical range of RTA temperatures for MOL process. In addition to temperature, multiple factors affect the forming phase and the quality of the germanide. Those factors include the ambient, crystallinity, microstructure, and strain. N_2 as an ambient slows down the reaction. As the crystallinity of Ge increases, higher temperatures are needed to form $CoGe_2$. The crystalline structures ordered from low to high germanide formation temperatures are: amorphous, polycrystalline, (100) and finally (111)-Ge. Higher temperature germanidation should be avoided to eliminate the possibility of Co in-diffusion into the Ge substrates. Such behavior has been seen at 600°C and above [71]. Compressive strain appears to enhance the germanidation reaction and tensile strain appears to retard the reaction.

6- Electrical properties of the contact

Metal/semiconductor contacts can be classified into two main types based on their electrical behavior: Ohmic and Schottky contacts. In semiconductor devices, Ohmic contacts represent the link between the semiconductor and the outside world. Schottky or rectifying contacts are found in a number of semiconductor device structures and they are important devices on their own. The electron affinity of Ge is 4.0 eV, its bandgap is 0.66 eV, and its intrinsic carrier concentration is $2x10^{13}$ cm^{-3}. The metal workfunction for cobalt is 5 eV. Figure 6 and table 8 show the conditions in which the metal semiconductor contact could become ohmic or Schottky contact.

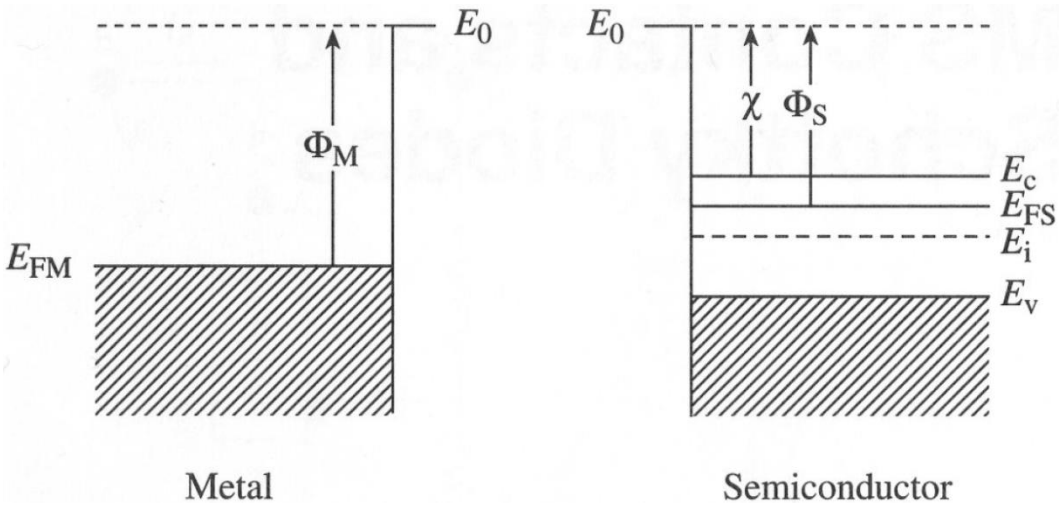

Figure 6: Energy band diagrams for a metal (left) and n-type semiconductor (right). Reprinted with permission from [128].

Table 8: Electrical nature of ideal MS contacts [128].

	n-type Semiconductor	p-type Semiconductor
$\Phi_M > \Phi_S$	Schottky	Ohmic
$\Phi_M < \Phi_S$	Ohmic	Schottky

The fabrication of low resistance contacts on semiconductors is, theoretically based on selecting a metal with a low workfunction for n-type semiconductors and a high workfunction for p-type semiconductors to obtain ohmic behavior. It is common for the interface states to pin the Fermi level and make the barrier height independent of the metal workfunction. The ohmic behavior could be obtained by heavily doping the layer of semiconductor interfacing with the metal [129] as will be detailed later. Carriers would then tunnel through the very thin depletion region created by such heavily doped layer.

Parasitic source/drain resistance is becoming a significant limiting factor in the scaling down of CMOS devices. This resistance is composed of four components [130]: 1- R_{ov}: source/drain extension to gate resistance, 2- R_{ext}: S/D extension resistance, 3- R_{dp}: deep S/D resistance, and 4- R_{csd}: silicide-diffusion contact resistance. Sub-100nm short

channel ultra-shallow S/D modelling of the series resistance reveals that the contact resistance (R_{csd}) is the dominant contributor to the series resistance as the devices are scaled down. R_{csd} is directly proportional to the interface contact resistivity given by [48, 131]:

$$\rho_c = \frac{k}{qA^*T} e^{q\varphi_B/kT} = \rho_{c0} exp\left(\frac{4pi\varphi_B}{qh}\sqrt{\frac{\epsilon_s m*}{N}}\right) ohm.cm^2 \quad (6.1)$$

where $\Phi_B = \Phi_M - \chi$, N is the net doping concentration at the metal-semiconductor interface, A^* is Richardson's constant for thermionic emission given by 143 $A.cm^{-2}.K^{-2}$ for n-(001)Ge [125], T is the temperature, q is the electronic charge, and k is Boltzmann's constant.

6.1- Ohmic and Schottky Properties of the Metal-Germanium contact

Researchers attempted forming ohmic contacts on both n-type and p-type Ge. It has been experimentally reported that a number of metals form Schottky contacts due to Fermi Level Pinning (FLP) on n-type (100)Ge [132-135]. Fermi Level Pinning (FLP) at the metal/n-type Ge interface is in close proximity to the charge neutrality level which lies only 0.09 (±0.07) eV above the valence band maximum [132, 133]. FLP is an obstacle in the development of high performing Ge MOSFETs since an ohmic contact to n-type Ge source and drain is not possible without Fermi depinning techniques. Schottky Barrier Height (SBH) has been experimentally measured for a number of metal/(100)n-Ge interfaces and it has been observed to be in the range of 0.49-0.65 eV [132-134]. The various SBH's measured for Co/n-type (100)Ge interface are summarized in table 9. On the other hand, p-type Ge (100) has ohmic characteristics for metal/(100)p-Ge interfaces including Co/(100)p-Ge interface [135].

The metal germanide/n-type Ge (100) interface has been studied by a number of researchers [118, 134, 136, 137]. Han et al. [136] observed that the Ni germanides/n-Ge interface is pinned at SBH of ~0.4 eV. Despite two crystallographic orientations of NiGe: (111) and (210), the SBH didn't change much. This has attributed to FLP. Nishimura et al. [134] also formed NiGe and observed the FLP in their case to cause the SBH to be in the range of 0.52-0.55 eV. Similar results were obtained by Chawanda et al. [137] in which an SBH of 0.532 eV was reported. They also did form $ErGe_x$ and observed FLP in that case as well. The SBH was different for $ErGe_{1.5}$ and $ErGe_{1.8}$: 0.47 eV and 0.52 eV respectively. The difference of the SBH between the NiGe in case of Han et al. [136] and that

for Nishimura et al. [134] and Chawanda et al. [137] couldn't be attributed to the difference in the doping concentration of the n-type Ge. Han et al. reported the resistivity of the n-Ge to be 0.4 ohm.cm corresponding to $4x10^{15}cm^{-3}$ and Chawanda et al. reported a similar doping concentration of $(2\text{-}3)x10^{15}cm^{-3}$.

Some germanides showed ohmic behavior or low SBH values after thermal annealing. Titanium germanide phases showed dependence of the SBH on the germanide phase as well as the anneal temperature [136]. Ti_6Ge_5 formed at 300°C and it showed the lowest SBH of 0.34 eV. Chawanda et al. [137] observed the I-V characteristics of Ti Schottky contacts severely deteriorated and became nearly ohmic as the temperature increased above 425°C. Pt germanides showed also variation of the SBH with temperature in case of Chawanda et al. [137]. This change in the germanide behavior with the temperature seems to be phase independent since Yao et al. [138] found that the barrier height for three different phases of Pt-germanides is identical. Janardhanam et al. [78] observed both Ti_6Ge_5 and Ti_5Ge_3 phases forming when deposited Ti was annealed at temperatures in the range of 500-600°C. In addition to those two phases a third phase: $TiGe_2$ was observed when annealing was performed at 700°C. $TiGe_2$ is a high conductivity phase. $PtGe_2$ was the only phase observed forming at all annealing temperatures (500-700°C) for the case of the Pt. Schottky behavior was observed for both Ti and Pt germanides forming at temperatures in the range of 500-600°C. FLP was also observed since the SBH was in the range of 0.58-0.62 eV for the case of Ti-germanide and it was in the range of 0.5-0.55 eV for the case of Pt-germanide independent of annealing temperatures. The germanides forming at 700°C exhibited ohmic behavior. Janardhanam et al. didn't attribute this to Fermi Level depinning. They rather attributed it to a drastic increase in the leakage current under reverse bias. After annealing at the temperature of 700°C, the sheet resistances increase due to the agglomeration of Ti- and Pt- germanides, surface and interface morphologies of both Ti- and Pt- germanides are degraded, which lead to the formation of defects such as voids and thermal grooves in Ti- and Pt- germanide films. The structural degradation results in additional current paths causing the ohmic behavior of such contacts. The quality of the interface is deteriorated at high annealing temperatures. A similar argument could be made for the difference in the SBH of NiGe/Ge between Han et al. [136] and Chawanda et al. [137]. While Chawanda et al. reported their annealing time of 30 minutes, Han et al. didn't report the annealing time. It is possible that Han et al. annealing time was much longer resulting in structural degradation of the interface resulting in effective lowering of the SBH due to increase in leakage current.

The behavior of metal/(111) n-Ge is different from that on (100) n-Ge. The Schottky barrier height is highly dependent on the metal workfunction and is independent on the Charge Neutrality Level (CNL) caused by FLP as discussed above [139]. SBH in the range of 0.34-0.54 eV was obtained depending on the metal [139]. There are no signs of FLP in case of metal (111) n-Ge surface. The SBH of Ni was found to be 0.44eV on (111) n-Ge compared to 0.58 eV (100) n-Ge. For metal/(111) n-Ge with a dopant concentration of $3x10^{14}$ cm^{-3} Schottky behavior was observed for Fe_3Si/(111)n-Ge [140]. Fe_3Si formed an epitaxial contact with (111)Ge given the close lattice constant: 0.564-0.566 nm for Fe_3Si compared to 0.565 nm for Ge. The Schottky barrier height was calculated to be 0.46 eV which is not within the expected range for FLP as indicated above. This Schottky behavior might be attributed to the difference between the workfunction of the iron silicide and the effective workfunction of (111)n-Ge. Similarly for Pt as well as Pt germanides forming at different annealing temperatures on (111)n-Ge, the SBH was phase dependent and no FLP was observed [141]. The only results claiming pinning at all different crystal orientations including (100), (110), and (111) were those obtained by Nishimura et al. [134]. Both Al and Au showed little variation with the change in the crystal orientation. It is possible that this pinning is connected to a very low dopant concentration in the n-Ge. Nishimura et al. don't report the doping concentration in their samples.

Fe_3Si metal on (111) p-Ge surface showed Schottky behavior which is in contrary to (100) p-Ge which shows ohmic behavior [140]. The authors attributed this behavior to Fermi level depinnning due to lattice constant matching between Fe_3Si and (111) Ge. This was the first rectifying data reported for the metal directly on p-Ge and the only reported results for (111)p-Ge. More experiments are needed to verify the behavior of the metal on (111) p-Ge.

Chawanda et al. [118] measured the Schottky barrier height between cobalt-based germanides formed at different annealing temperatures and germanium. They used n-type (100) Ge for their experiment. The doping level was $2.5x10^{15}cm^{-3}$. Chawanda et al. [118] experimentally determined that the Schottky barrier height of the Co-Ge contact is 0.513 eV at room temperature. The difference in the SBH between Chawanda et al. and Zhou et al. [135] could be attributed to the difference in doping concentration. The resistivity of Ge used by Zhou et al. corresponds to a doping concentration of ~$9x10^{13}cm^{-3}$ compared to $2.5x10^{15}$ used by Chawanda et al. By annealing the sample from 30°C-600°C for 30 minutes in argon ambient, they quantified how the Schottky barrier height changes as the nature

of the interface changes. The authors used Sun et al.'s [112] experiment to guide their expectations for the germanide phases. This is rather inaccurate given that Sun et el. used reactive deposition in their study which is expected to yield different phases compared to solid state anneals as explained in the previous section. Chawanda et al. also expected a germanide phase to be present at 100°C. That is not supported by past experimental data, detailed in table 5, which shows that no germanide is expected to form below 200°C. Our data indicates that Co_5Ge_3 forms in the range between 220°C and 250°C with the expectation that not all the cobalt will react at lower temperatures [92]. Both cobalt and its germanide will be present at such temperatures. This is also supported by the weak XRD signals observed by Hsieh et al. [33] suggesting a mixture of cobalt and its germanide. Therefore, the data point at 250°C can be used to obtain the Schottky barrier for Co_5Ge_3 which is 0.53eV. At higher temperature CoGe is expected. The data point at 280°C can be used for CoGe resulting in a Schottky barrier of 0.544 eV. This value is in agreement with that reported by Park et al. [97]. Simoen et al. reported SBH to be 0.417 eV for CoGe [71]. This difference is possibly related to variability in crystallinity of the germanide which has not been reported in Simoen et al.'s work. Germanides were formed using ramp-up anneal in case of Simoen et al. compared to constant temperature anneal for the other two works [97, 118]. The annealing method is likely to affect the germanide crystallinity. Co_5Ge_7 is dominant between 300°C and 380°C. The Schottky barrier for Co_5Ge_7 can be obtained by averaging the data points between those temperatures which results in 0.554 eV. A mixture of Co_5Ge_7 and $CoGe_2$ is expected above this temperature until 550°C where only $CoGe_2$ is likely to be present. Therefore, it can be concluded that the Schottky barrier for $CoGe_2$ is 0.524eV. The germanide phases suggested above are also based on our model explained in section 4.4 [106].

In a different experiment, Lajaunie et al. [72, 121] pretreated the surface of Ge before Co deposition by an anneal at 400°C and 700°C for an hour in two separate experiments. They measured the SBH after Co deposition for the three different samples: without pretreatment and with the 2 different pretreatment. The lowest barrier height corresponds to the case where the sample was not pretreated: 0.28eV [72] or 0.33eV [121] followed by the 400°C pretreatment and finally the 700°C pretreatment as shown in table 9. Similar pretreatment experiments have been conducted by Lajaunie et al. [125] but for shorter time of 40 minutes in addition to the ramp up time of 20 minutes. The SBH results are reported in table 9 and they are different from the other experiment of Lajaunie et al. [72, 121].

The surface was not cleaned for the first experiment resulting in SBH of 0.3 [125]. The HF was (1:20) in the second experiment resulting in an SBH of 0.38 eV. Lajaunie et al. [125] point another factor that contributes to the fermi level depinning that is the quality of the oxide forming between Ge and the deposited Co. GeO_2 results in the best depinning compared to other Ge sub oxides (GeO_x, $x \neq 2$). Chawanda et al. [118] cleaned the surface with H_2O_2:H_2O (1:5). The doping concentration in case of Lajaunie et al. was $1x10^{14}cm^{-3}$ similar to that used by Zhou et al. [135] and their deposition technique of Co was similar to that of Chawanda et al. and Zhou et al.: e-beam evaporation. The surface pretreatment was different for Zhou et al. They used diluted HF (1:50) to clean the sample. The SBH after the formation of $CoGe_2$, in case of Lajaunie et al. [72], was higher than that of Co: 0.41 eV compared to 0.28 eV. This value is lower than that obtained by Chawanda et al. as shown in table 9. Ohmic behavior was observed for $CoGe_2$ on n-Ge in the experiment conducted by Park et al. [97]. The authors attributed the ohmic behavior to possible metal defects in Ge due to Co indiffusion. This is not a likely scenario since such ohmic behavior wasn't seen by Lajaunie et al. despite much longer anneal (40 min compared to 1 min) at the same temperature: 700°C. Two differences in case of Park et al. are the surface cleaning and the Co deposition method. The surface was cleaned using (H_2O:HF=100:1) solution and Co was deposited by dc magnetron sputtering.

Surface pretreatment before Co deposition is detrimental in the SBH [125]. The two common methods for surface pretreatment as discussed above are HF cleaning and heating the sample at high temperatures. The roughness of the Ge surface increases by a factor of two during HF cleaning [142]. As a result, the spatial inhomogeneity of the Ge surface increases resulting in altering the SBH. In addition, this cleaning method doesn't completely remove the metal impurities [142] which is another factor affecting the SBH. Annealing Ge before metal deposition is another way to clean the surface. GeO_x desorption occurs at 430°C in high vacuum [143] or 360°C in UHV if the wafer is annealed for 15 minutes [133]. The metal deposition method also affects the SBH since implantation defects created as a side effect of the deposition technique especially the energetic particles during sputtering alter the SBH [144, 145]. Predictions of Shockley-Read-Hall model and recombination lifetime measurements have confirmed Co to be an efficient carrier lifetime killer [71, 146, 147]. Therefore, implanted Co defects are expected to affect the SBH as well as the related IV and CV characteristics of the germanide contact [148]. The results for all SBH experimental measurements are summarized in table 9. It has to be noted that all the

results in table 9 are for (100) n-Ge with variable doping concentrations. Doping concentration is another factor that could contribute to the variation in the SBH.

Table 9: Experimental Schottky Barrier Height calculated based on the results of [118] and other references mentioned in the table. A is taken from [125].*

Metal in contact with (100) n-type Ge	Experimental Schottky Barrier Height (eV)	Interface contact resistivity ($ohm - cm^2$)
Co	0.513 [118], 0.62 [135], (0.33, 0.45, 0.49) [121, 125], 0.28 [72], (0.53, 0.55) [97] (0.3, 0.38, 0.44) [125]	1.61, 98.8, $7.029x10^{-4}$, 0.0729, 0.3424, $1.016x10^{-4}$, 1.609, 3.488, $2.2x10^{-4}$, $4.86x10^{-3}$, $4.95x10^{-2}$
Co_5Ge_3	0.53	3.1
CoGe	0.544 [118, 97], 0.417 [71]	5.3, 0.0203
Co_5Ge_7	0.554 [118], 0.54 [97], 0.485 [71]	7.8, 2.3689, 0.2822
$CoGe_2$	0.524 [118], 0.41 [72], Ohmic [97], (0.474, 0.37, 0.448, 0.4, 0.432) [71]	2.46, 0.0155, 0, 0.1844, 0.0033, 0.0675, 0.0105, 0.0363

The workfunction of Co is 5.0 eV. Chawanda et al. [118] used n-type (100) Ge with a doping level of $2.5x10^{15}cm^{-3}$ for their experiment [118] resulting in a Φ_S of 4.2 eV. The expected Φ_{MS} of Co-Ge contact if no FLP is taking place is 0.8 V. Theoretically, Co and the n-type Ge used by the authors will result in a Schottky barrier ($\Phi_B=\Phi_M-\chi_{Ge}$) of 1 eV. Similar calculation could be conducted for other experiments summarized in table 9. The values of SBH reported in table 9 indicate that FLP is taking place.

The values of the interface contact resistivities presented in table 9 are quite high. It has to be noted that those resistivities have exponential dependence on SBH. In order for Co and its germanides to serve as good S/D contacts materials in the current FinFET technology, those resistivities have to be brought down to the $1.0x10^{-9}$ ohm.cm^2 range. FLP is the main contributing factor to those large Schottky barrier heights. FLP could be eliminated or reduced with the growth of epitaxial germanides. Despite multiple attempts to grow epitaxial cobalt germanides, as will be detailed in section 6.4, there are no reports in the literature for the SBH of a single phase epitaxial cobalt

germanides. More work is needed to evaluate quality of single phase epitaxial cobalt germanide contacts. The values reported in table 9 could not be compared to the extremely low resistivities reported for titanium germanides, discussed in section 2, since none of the experiments in table 9 used heavy doping fermi level depinning techniques. FLP and its depinning mechanisms are presented in the next subsections.

6.2- Fermi Level Pinning Mechanisms:

Fermi level pinning reduces dependence of Schottky barrier height on metal work function. Three theories have been proposed to explain the origin of FLP [149]. The first theory proposed by Tsipas and Dimoulas is that FLP is a result of native defects, e.g. dangling bonds [150]. Those dangling bonds form when the clean surface of Ge is exposed to oxygen and they remain unpassivated in presence of native oxide or a dielectric. Dangling Bonds (DBs) continue to exist after the metal deposition to form a metal contact. Even with an atomically matching metal, there are still some dangling bonds causing partial FLP [151]. Nishimura et al. [134] observed little change in the SBH with metal germanidation. They suggested that this indicates that the FLP is caused by bulk properties of Ge. This suggestion is not necessarily valid since the interface might have not been changed much by germanidation. The DBs are expected to remain in case of metal germanidation since Ge is the diffusing species and not the metal. Therefore, the metal-Ge interface is not consumed since the reaction doesn't occur at the metal-Ge interface. Passivation of the dangling bonds using hydrogen was found to be ineffective [152] unlike silicon interface [153]. This has been shown experimentally [154] and it was theoretically attributed to the negatively charged hydrogen atom which has a similar energy level to the DBs [152]. Afanas'ev et al. [154] conducted electron spin resonance analysis and indicated that the DBs are below the experimental detectability limit. Two later studies [155, 156] calculated the energy states of the DBs using ab initio methods. Broqvist et al. found the energy states of the charge transition levels of the DBs to be 0.05 and 0.11 eV above the valence band edge for the donor and acceptor DB states, respectively [155]. Their model explained the lack of ESR signal observed in [154] is due to the proximity of the charge transition levels to each other as opposed to their large separation in (100)Si. Houssa et al. [156] used density functional theory to calculate the energy state of interfacial Ge dangling bonds. They found that the energy state was close to the mid-gap energy level for neutral DB state. They explained that the ESR signal was not observable in [154] due to the lower Young's modulus in GeO_2 compared to SiO_2 resulting in lower DB density in

Ge below the detectability limit of ESR. The DBs have been experimentally detected at the Ge-dielectric interface by using a different technique: electrically detected magnetic resonance (EDMR) spectroscopy [157, 158]. Those results confirm the existence of DBs and support this theory. Those DBs could be modeled as negatively charged states. Their density could be derived from the threshold voltage of a Metal-Insulator-Germanium capacitor that could be measured experimentally [150].

The second theory attributes FLP to Metal Induced Gap States (MIGS) [159] which exist in *"an energy range where the conduction band of the metal overlaps the semiconductor band gap"*. MIGS is caused by the decay of the travelling wave function of the electrons from the metal electrode into the bandgap of Ge. Self-consistent pseudopotential calculations of the electronic structure of the metal-semiconductor interface predicted the existence of metal-induced gap states [160]. MIGS have also been experimentally observed using electron energy loss spectroscopy [161]. Near the conduction band the states are acceptor-like and near the valence band they are donor-like. The energy level in the band gap at which the dominant character of the interface states changes from donor-like to acceptor-like is called the charge neutrality level E_{cnl}. This energy level is shown in figure 7. Charge transfer generally occurs across the interface due to the presence of intrinsic interface states. Charging of these interface states creates a dipole that tends to drive the band lineup toward a position that would give zero dipole charge. This property causes the metal fermi level to move to towards the E_{cnl} to give a zero dipole, making the new metal work function differ from the vacuum metal work function. Nishimura et al. [134] performed an experiment in which they studied the Fermi level pinning for multiple Ge orientations: (100), (110), and (111). They found that the FLP is independent of the surface orientation as well as annealing and they concluded that this proves that the MIGS theory is correct in explaining FLP since surface orientation and annealing are expected to affect dangling bonds. This is in contrary to other researchers detailed in section 6.1 who have seen an effect for the Ge surface orientation on the FLP.

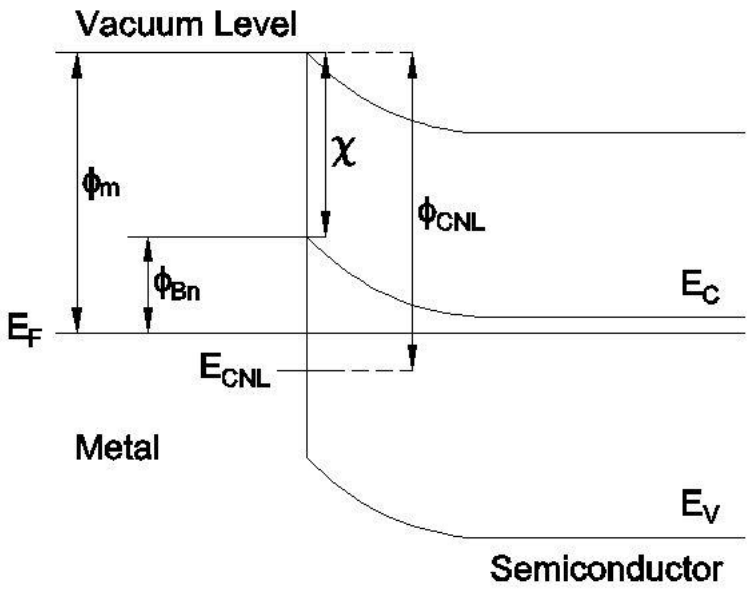

Figure 7: Energy band diagram showing Charge Neutrality Level (CNL) at the metal-semiconductor interface.

The pinned barrier height is given by:

$$\emptyset_{Bn} = S(\emptyset_m - \emptyset_{CNL}) + (\emptyset_{CNL} - \chi) \tag{6.2}$$

where *S* is a pinning factor given by:

$$S = \frac{d\emptyset_{Bn}}{d\emptyset_m} = \left[1 + \frac{D_{is} q^2 \delta}{\varepsilon}\right]^{-1} \tag{6.3}$$

where D_{is} is the density of interface states per unit energy, δ is the distance extent of the interface states in the semiconductor, q is the electron charge, and ε is the permittivity of the semiconductor.

The third theory relates FLP to bulk evanescent states of Ge [149]. To understand evanescent states, it is important to note that the physics of bulk semiconductors relies heavily on the concept of an ideal periodic structure of the crystal lattice. Surfaces and interfaces represent a terminal disruption of periodicity. The surfaces and interfaces properties are quite distinct from the bulk of the semiconductor. Evanescent states are states with complex wave vectors that have real energy levels that lie in the forbidden bandgap of the semiconductor. Kuzmin et al. [149]

attributed the FLP to the evanescent states of the bulk of Ge and supported their theory with experiments and theoretical calculations. The three theories go hand in hand and each of them has supporting experimental and theoretical results. Therefore, all three of them should be considered when explaining the FLP at the metal-Ge interface.

6.3- Fermi Level Depinning

Four different methods have been effective in depinning the Fermi level at the metal/Ge interface: a) heavy doping technique, b) surface cleaning and passivation using sulfur or similar elements, c) depositing an ultrathin interfacial layer of a dielectric between Ge and the contact metal, d) changing the composition of the metal by introducing nitrogen to achieve a dipole at the interface to depin the Fermi level.

The first method is the heavy dopant technique in which a heavily doped germanium layer is formed near the germanium/germanide interface resulting in a strong conduction/valence band bending near the interface and a very thin potential barrier caused by the carrier depletion as shown in figure 8. When an electric field is applied to the structure, carriers tunnel through the potential barrier resulting in ohmic behavior. This heavy doping technique was early reported and adopted for silicon [162]. It is also the preferred technique used by the industry to resolve the FLP issue [79, 163]. The heavy doping is achieved through dopant segregation. Two different methods have been adopted for dopant segregation: Implantation Before Germanidation (IBG) and Implantation After Germanidation (IAG) [164]. In case of IBG, the dopant is implanted at low energy below 42 KeV into bare Ge wafer. This is followed by metal deposition and finally, an RTA (Rapid Thermal Anneal) to form the germanide at a temperature ranging from 350-500°C. In case of IAG, the metal is first sputtered and annealed to form the germanide and then the dopant is implanted at higher energies ranging from 33-60 KeV after the germanidation. Finally, the dopant is activated using a second anneal at temperatures ranging from 350-550°C. Schematic diagrams are shown for both methods in figures 9 and 10.

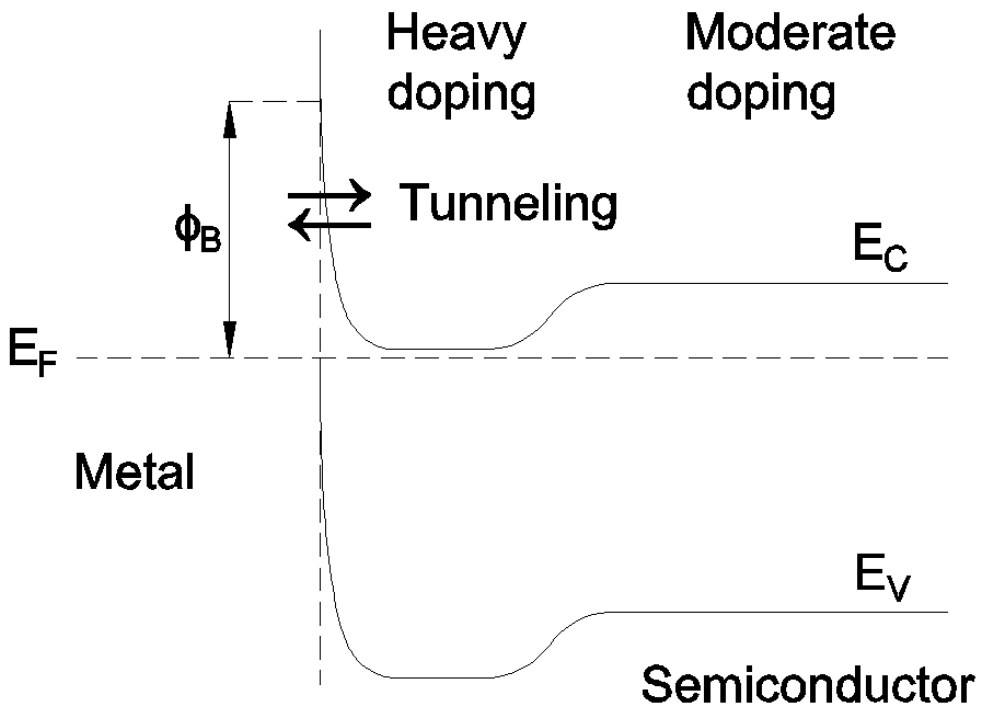

Figure8: Ohmic behavior achieved by tunneling through a thin potential barrier.

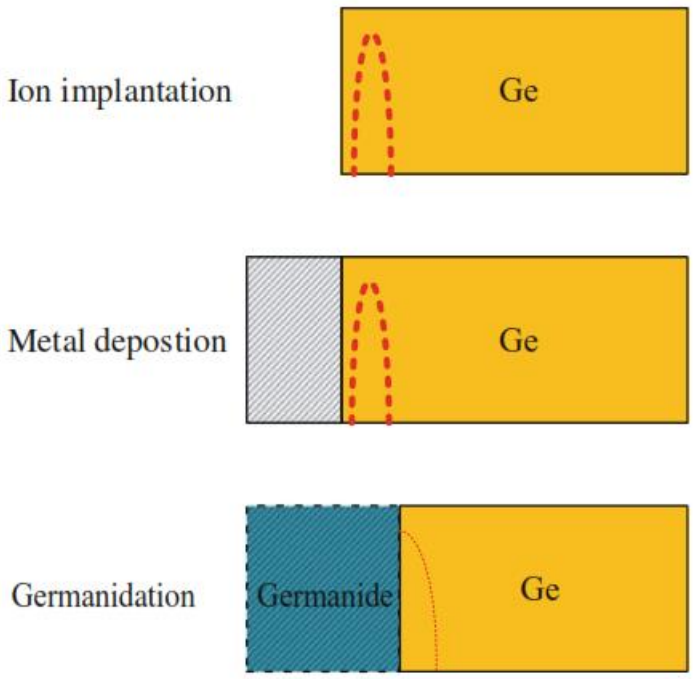

Figure 9: Illustration of Implantation Before Germanidation (IBG) technique adopted from [164].

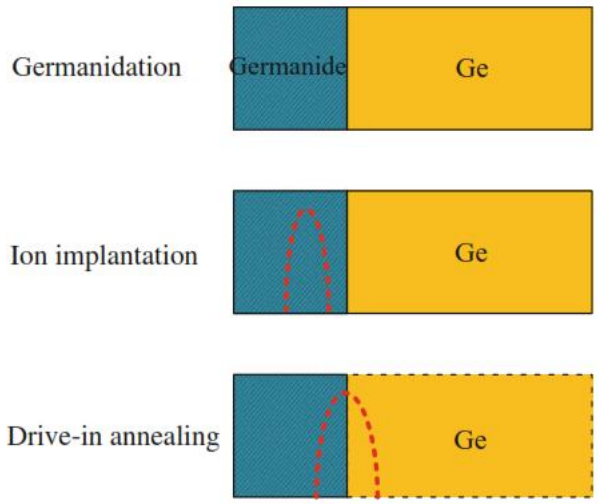

Figure 10: Illustration of Implantation After Germanidation (IAG) technique adopted from [164].

SBH of 0.38 and 0.19 eV are achieved for the NiGe/Ge interface by the pre-germanide implant of P and As, respectively [165] using the IBG technique. The SBH obtained using P and As implant using IAG technique was lower: 0.1 eV and 0.14 eV respectively [164]. Those results show that the IAG technique gives better results than the IBG technique for the following reasons. IBG results in more diffusion and less dopant at the interface given the higher thermal budget needed for germanidation. In addition, the implantation damage will increase the dopant diffusion. Lastly, the implanted dopants will damage the surface hindering the formation of the germanides.

Chalcogens like sulfur and selenium have also been used in fermi level depinning. Unlike P and As, those dopants are deep level dopants and they introduce double-donor states in germanium [166]. Tong et al. [167] investigated the effect of Se and S implant into Ge before Ni germanidation. They used As-doped ($7–13x10^{16}$ cm^{-3}) n-type (100) Ge wafers. For Se: the implantation energy was selected so that the peak Se concentration is within the top 20 nm of Ge which will later be consumed during NiGe formation. 14 nm of Ni was then deposited by e-beam evaporation, followed by a 350°C 30 s anneal in N_2 ambient to form nickel germanide. S and Se were very effective in fermi level depinning. The SBH was reduced from an original value of 0.61 eV to 0.13 eV in case of Se and 0.1 eV in case of S. XRD signals and high-resolution TEM (transmission electron microscopy) images confirmed that the reduction of SBH is not due to the phase change of nickel germanide. Using SIMS (secondary ion mass

spectrometry) technique, Se and S segregation peaks were found at NiGe/n-Ge interfaces. Se and S atoms were pushed to the interface due to the snowplow effect. Therefore, SBH reduction is related to Se or S segregation. Se is known to act as a donor impurity in Ge and introduces a shallow donor-like trap level at 0.14 eV below the conduction band of Ge. The traps could lead to sharp upward band bending of Ge, reducing the electron barrier width for tunneling, and increase the probability of trap-assisted tunneling (TAT) of electrons through the barrier region. It results in a larger reverse bias current which is represented as a smaller effective electron SBH. S also acts as a donor impurity in Ge with a trap level of 0.18 eV below the conduction band of Ge, and same mechanism as above.

Similar results were obtained by Ikeda et al. [168]. In their experiments, sulfur is ion implanted with energy of 10 KeV in germanium before nickel deposition [168]. Nickel was then deposited and the structure was annealed. During germanidation sulfur snowplowed with high concentration in Ge near the NiGe/Ge interface. Higher concentration of sulfur was shown to lead to lower SBH. The authors [168] were able to achieve an SBH of 0.15 eV at a concentration of $1x10^{15}/cm^2$ instead 0.61eV without sulfur.

The second method for fermi level depinning is surface cleaning using sulfur or similar elements instead of ion implantations. Thathachary et al. [169] obtained Al and Zr ohmic contact to n-type Ge by passivating the Ge surface using sulfur. Unlike Ikeda et al. [168], sulfur was not implanted. The wafer was exposed to 40% aqueous ammonium sulfide solution $(NH_4)_2S$ for 5 minutes at $50^{\circ}C$ before sputtering the metal contacts. No germanides were formed in this case. The drawback of this method is that if germanides form at a later point during the BEoL process due to a high temperature anneal, that might be required, the forming germanide might again cause Schottky behavior. The depinned interface using the sulfur passivation technique agrees with the Schottky-Mott theory. An extension to this method was presented by Kasahara et al. [151] in which the atomic-arrangement matching between the deposited metal and Ge results in high quality interfaces. Atomic-arrangement matching minimizes the dangling bonds at the interface. Further sulfur treatment almost gets rid of dangling bonds and, consequently, gets rid of FLP.

The third method to depin the Fermi level is to introduce an ultrathin interfacial dielectric layer between Ge and the contact metal. The function of this ultrathin layer is to block the free electron wave function from penetrating

from the metal into the semiconductor reducing MIGS [170]. This method was first suggested by Connelly et al. to resolve the FLP in case of silicon [171]. Kobayashi et al. [170] used this method for Ge. They deposited an interfacial SiN by well-controlled sputter system and they fabricated an Al/SiN/Ge Schottky diode. The thickness of the SiN layer was carefully optimized. As the thickness increases initially from 0 to 2 nm, the MIGS density was reduced and the contact resistance was also reduced to a specific minimum ~0.1 ohm.cm^2. As the SiN gets thicker the contact resistance increased again due to the increase in the tunnel resistance resulting from the thick dielectric and the behavior turns to be non-ohmic. A 2 nm SiN results in purely ohmic behavior on the Ge/SiN/Al contact. Thicker SiN is needed to depin the Fermi level compared to Si which needs an SiN layer that is less than 1nm in thickness. Optimum thickness of SiN was ~2.5 nm for Ti and 3 nm for Er. The lowest contact resistance corresponds to Er. It is notable that Pt was unpinned without the SiN layer. After using the SiN barrier, Schottky barrier had linear dependence on metal workfunction for the following metals: Al, Ti, W, Ni, and Pt. Er has zero Schottky barrier height given its low workfunction.

A different stack was suggested by Kim et al. [172] in which they used two interfacial layers between the Ti metal and Ge. The stack that gave ohmic behavior was made of 1 nm of TiO_2 and 1.5 nm of GeO_2. The authors experimented with other thicknesses but none of them resulted in ohmic behavior. The authors suggested that the function of TiO_2 is to reduce the MIGS states and the function of GeO_2 is to reduce the interfacial trap states generated by dangling bonds. Many other interfacial layers have been adopted in the literature such as Al_2O_3 [135], Y_2O_3 [173], MgO [174], Ge_3N_4 [129], and Si_3N_4 [175]. The method of interfacial layers used to depin the Fermi level is very sensitive to the thicknesses of the interfacial layers used for that purpose. If the layer is too thin, it won't passivate the MIGS enough and it results in Schottky behavior and if is too thick, it introduces tunneling resistance and results in non ohmic behavior again. Therefore, it might represent an industrial challenge to control the thickness of the interfacial layer in practice especially in case of mass production.

The forth method is to deposit metallic nitrides onto Ge without mixing or reaction between metallic nitrides and Ge. N-Ge bonds, which are at the interface between metallic nitrides and germanium, form a dipoles layer due to the significant difference of electron negativities between N (3.04) and Ge (2.01). The electrical potential of the dipoles layer generates an energy band drop as shown in figure 11. The energy band drop offsets partial value of

SBH [176]. Wu et al. [176] sputtered tungsten onto the n-type (100)Ge wafer with different Ar/N_2 gas flow rate, in order to form different composition of WN_x.

Five experiments were designed where Ar/N_2 ratio was used to control the composition of the metal. Ar/N_2 = 50/0 (pure tungsten), 50/1, 50/2, 50/3, 50/5 gas mixtures were used. The SBH_s of WN_x/n-Ge are 0.52, 0.47, 0.42, 0.39 and less than 0.3, respectively. It represents that SBH decreases when increasing the amount of N_2. In addition, ohmic contact appeared at Ar/N_2 = 50/5. The x values for each sample were determined as 0, 0.06, 0.09, 0.15, 0.19 by integrating the X-ray photoelectron spectroscopy peaks. It shows the growth of N in WN_x with the change of Ar/N_2 flow rate. Moreover, no interlayer is detected by Transmission electron microscopy. SBH modulation (band energy drop) has positive-linear relationship with nitrogen component x. It indicates that SBH is inversely proportional to nitrogen component x. Thus, the N-Ge dipoles control the SBH and achieve the fermi level depinning.

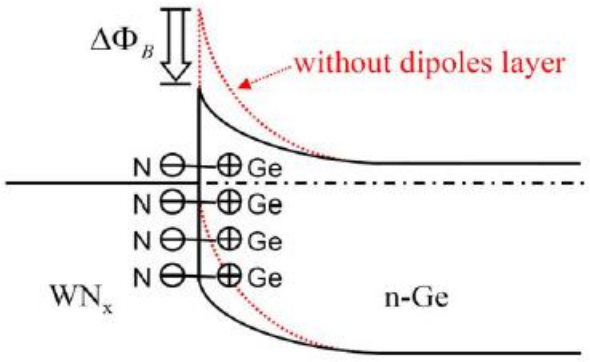

Figure 11: Effect of N-Ge dipoles on the energy band at the metal-Ge interface. Reprinted with permission [176].

6.4- Effect of metal crystallinity on Schottky Barrier Height

The metal work function of the crystalline contact is higher than that of its amorphous counterpart [177]. This is because, in general, densely packed crystallographic surfaces have high work functions since these surfaces are relatively inert with fewer broken atomic bonds, while open crystallographic surfaces display lower work functions

due to a greater number of broken bonds [178]. As a result, the Schottky barrier height of amorphous contacts displays a higher value than that of their crystalline counterparts [179]. It is, therefore, desirable to have a crystalline metal contact to reduce the Schottky barrier height and obtain a low resistivity ohmic contact. Careful phase control might be required to obtain such contacts. The variable SBHs reported in section 6.1 might be connected to the difference in the grain size of the forming cobalt germanides. The resistivity of the germanide phase is also affected by its crystalline state. The lowest resistivity corresponds to the single crystalline phase and the resistivity increases as the amorphousness increases as was shown and explained in section 3.

The lattice constant of silicon is 5.431 Å and that of germanium is 5.658 Å. Looking back at table 2, it is clear that 2 phases of cobalt germanides have lattice constant close to that of Ge: Co_5Ge_7 (2.7% lattice mismatch) and $CoGe_2$ (0.4% lattice mismatch). The match in the lattice constants between cobalt germanides and germanium increases the possibility of growing epitaxial crystalline cobalt germanide phases on germanium. On the other hand, the titanium germanide phase with the closest lattice constant to Ge is TiGe with a lattice mismatch of 7.5% [67]. Therefore, cobalt germanides have an advantage over titanium germanide in matching the lattice constant of Ge and it is easier to grow epitaxial or partial epitaxial cobalt germanides on top of Ge. Theoretically, it should be possible to achieve lower interface contact resistivity of cobalt germanides compared to titanium germanides. The lattice mismatch between $CoSi_2$ and Si is 1.2%. No titanium silicide have lattice mismatch to Si as close as the cobalt silicide has to Si.

Several attempts have taken place to grow crystalline cobalt germanides on Ge. Partial epitaxial polycrystalline Co_5Ge_7 is the phase that formed at 280˚C up to 500˚C on (111) Ge [33]. At 500˚C, the grain size of Co_5Ge_7 was 0.5um compared to 80nm grain size for the grains formed at 220˚C. Hsieh et al. [33] attributed the lack of single crystalline phases to the larger calculated lattice mismatch between Co_5Ge_7 and $CoGe_2$ and (111) Ge compared to the case of $CoSi_2$ and Si in which they observed single crystalline phase. However, the difference in crystalline structure might be another cause. Co_5Ge_7 and $CoGe_2$ are tetragonal and orthorhombic, respectively, compared to cubic diamond lattice for Ge. On the other hand, both Si and $CoSi_2$ are cubic in nature. The authors didn't measure the SBH. Similar epitaxial polycrystalline Co_5Ge_7 layer was reported by Sun et al. [112] in their reactive deposition experiment discussed in section 5. Two orientations were reported: Co_5Ge_7 (001) and Co_5Ge_7 (110).

Lajaunie et al. [121] also obtained a layer of polycrystalline Co_5Ge_7 on top of a layer made of both Co_5Ge_7 and $CoGe_2$ both polycrystalline. The orientation of both Co_5Ge_7 and $CoGe_2$ was (001) on top of (001)Ge. This result was obtained for the sample that was pretreated by heating before Co deposition at a temperature of 700˚C for 1 hour. The sample was, then, annealed after Co deposition at 700˚C for 40 minutes. The resulting germanide stack confirms the physical model for germanidation that was presented in section 4.4. The SBH obtained [72] was lower than that obtained by other researchers [118] as was presented in section 6.1 but this cannot be attributed only to the crystalline nature of the structure since the initial cobalt SBH was also different than [118]. The surface pretreatment might have contributed to the different SBH value. Single crystalline $CoGe_2$ islands were grown on Ge by Choi et al. [115]. The orientation of $CoGe_2$ was (001). The experiment parameters are detailed in section 5. Ge substrate was kept at 427˚C during Co deposition from a high purity Co source using e-beam evaporation resulting in high quality of the germanide after the reaction was complete. The time of the anneal was 10 minutes at 427˚C. At such relatively low temperature, more time might have been needed for all Co to transform into the low resistivity phase. As pointed earlier, only islands of $CoGe_2$ were observed. No SBH was reported by Choi et al. The temperature of the substrate and the quality of the deposited Co seem to be key parameters in obtaining epitaxial germanide [112, 115]. More carefully designed experiments are needed to obtain uniform films of epitaxial $CoGe_2$ on Ge, rather than islands, and measure the SBH of the interface.

7- Challenges and Future Trends

Cobalt germanides are potential electric contacts to advanced CMOS devices, solar cells, and GaAs devices. Little attention has been given to cobalt silicides and germanides as contacts for advanced CMOS technology nodes in recent years. Cobalt silicides and germanides could be a viable candidate to contact the source and drain regions in 3D devices. More research and contact resistivity optimization is needed to understand the capabilities of cobalt silicides as liner contacts as compared to titanium silicides. Cobalt silicides grow epitaxially on silicon and that gives them by default an advantage over titanium silicides. However, no recent attempts have been made to lower the contact resistivity of cobalt silicides. Cobalt germanides have shown variability in the Schottky and Ohmic

behaviors as discussed in the paper. Multiple factors contribute to the variation in SBH's including the phase of the germanide, the crystallinity of Ge and the germanide, the surface pretreatment before Co deposition, the deposition method of Co, and the doping profile in Ge. While multiple researchers indicated those factors, a systematic study is still lacking to quantify the contributions of each of those parameters to the behavior of the contact and the SBH. The understanding of the electric behavior of Co germanides on (111) Ge has not yet been reported both for n- and p-types. Single crystalline phases have not yet been achieved reliably. Such phases might be of great importance to the contact formation since they are expected to have very low contact resistivity without having to depin the interface by introducing heavy doping. In addition to advanced CMOS applications, such contacts will be very attractive for solar cells and junction-less transistors. Most schemes for GaAs contact metallization require alloying. The alloying process is known to introduce nonhomogeneous interface morphology and potentially spiking problem [180]. $CoGe_2$ phase as a contact has a high melting temperature with a small lattice mismatch to GaAs. High quality epitaxial $CoGe_2$ layer was grown on GaAs [180]. The electrical properties of the contact on GaAs still need to be studied in more detail.

Cobalt germanides have been recently used in memory applications [83]. They have been employed in nano-floating gate memory (NFGM) which is a type of nonvolatile memory (NVM). NVM retains data even in absence of electric power. Floating gate memory is a MOSFET with a floating gate semiconductor (poly-Si is commonly used) separated from the semiconductor by a tunneling oxide and from a top control gate by a thick oxide [181]. The floating gate stores charge which is transferred to it by impact ionization from the device when it is in its on-state. The charge is released by reverse biasing the control gate. Conventional floating gate memory devices suffer from increased leakage current due to scaling down the tunnel oxide layer. This problem is escalated when the device is repeatedly stressed. Nanocrystal NVM had been invented later in the early nineties to solve the scaling issue of the tunneling oxide. The charge is stored on a discrete, mutually isolated, crystalline nanocrystals layer, which is typically made of semiconductor material. This NVM could reduce the thickness of the tunnel oxide without affecting device nonvolatility. Thus, resulting in lower operating voltage and higher operating speeds. Also, nanocrystal memory structure allows more simplified fabrication process with shorter channel lengths. In addition, it can prevent current leakage and oxide defects [182].

Nanocrystals could, alternatively, be made of metals. Metal nanocrystals could store capacitive charge. They form deep quantum wells in the dielectric material. They also have high density of states near the Fermi level resulting in better charge trap characteristics. Cobalt germanide nanostructure has been used in the charge trap layer of nano-floating gate memory [83]. The reason for using cobalt and germanium is that cobalt has larger work function than the electron affinity of p-type silicon so it can support a higher charge storage capacity and germanium works as a nucleation center during RTA process so it could improve nanostructure aggregation. RTA was performed at very high temperature of 830°C. Nanocrystals might behave different than bulk materials in terms of phase formation. The exact phase was not reported by the authors. CoGe nanostructure after RTA showed larger opening of the memory window than individual Co or Ge after C–V measurements. The formation of Co-Ge bonds during RTA enhances the charge capacity of the nanocrystals.

Memory applications and other niche application based on cobalt germanide would benefit from an indepth understanding of the different phases of cobalt germanides, their workfunctions, formation temperatures in different processes, and other fundamental properties that are not yet well understood. Bulk and interfacial contact resistivities of low temperature forming phases, Co_5Ge_3 and CoGe, are of special interest since those phases could potentially be functional contacts to advanced CMOS devices with a very low thermal budget. No data reported in the literature, to date, about the resistivities of those phases.

References:

[1] This history is in part after: James D. Plummer, Michael Deal, Peter D. Griffin, *Silicon VLSI technology: fundamentals, practice, and modeling*, (Prentice Hall, Inc., 2000), Chapter 11, pp. 681–786.

[2] Bardeen, J., & Brattain, W. H., *Phys. Rev.*, *74*(2), 230–231 (1948) and image from: https://www.extremetech.com/extreme/175004-the-genesis-of-the-transistor-the-single-greatest-discovery-in-the-last-100-years

[3] Hall, R. N. *US2717343A*. United States, (1955)

https://patents.google.com/patent/US2717343A/en?oq=US2717343A

[4] Workman, W., *Microelectron. Rel.*, *7*(3), 257–265 (1968)

[5] Sello, H., Blech, I. A., Snow, E. H., Lawrence, J. E., Duncan, D. L. A STUDY OF FAILURE MECHANISMS IN SILICON PLANAR EPITAXIAL TRANSISTORS, https://apps.dtic.mil/docs/citations/AD0800048. Accessed Aug 1966.

[6] McCarthy, J., *Microelectron. Rel.*, *9*(2), 187–188 (1970).

[7] Chino, K., *Solid-State Electron.*, *16*(1), 119–121 (1973).

[8] Rhoderick, E. H., *IEE Proc. I - Solid-State and Electron Devices*, *129*(1), 1- (1982).

[9] Basterfield, J., Shannon, J. M., & Gill, A., *Solid-State Electron.*, *18*(3), 290 (1975).

[10] Nicolet, M.-A., *Thin Solid Films*, *52*(3), 415–443 (1978).

[11] Kittl, J. A., Opsomer, K., Torregiani, C., Demeurisse, C., Mertens, S., Brunco, D. P., Van Dal, M. J. H., Lauwers, A., *Mater. Sci. Eng., B*, *154–155*, 144–154 (2008).

[12] Kahng, D.; Lepselter, M.P., Bell Syst. Tech. J., 44: 7. pp 1525-1528 (1965).

[13] Hosack, H. h., *Appl. Phys. Lett.*, *21*(6), 256–257 (1972).

[14] Epstein, J. *US3664874A*. United States, (1972) https://patents.google.com/patent/US3664874/en

[15] Locker, L. D., & Capio, C. D., *J. Appl. Phys.*, *44*(10), 4366–4369 (1973).

[16] Lau, C. K., See, Y. C., Scott, D. B., Bridges, J. M., Perna, S. M., & Davies, R. D. *In 1982 Int. Electron Devices Meeting (IEDM)* (pp. 714–717) (1982).

[17] Lasky, J. B., Nakos, J. S., Cain, O. J., & Geiss, P. J., *IEEE Trans. Electron Devices*, *38*(2), 262–269 (1991).

[18] Kittl, J. A., Prinslow, D. A., Apte, P. P., & Pas, M. F., *Appl. Phys. Lett.*, *67*(16), 2308–2310 (1995).

[19] Niazmand, M., Friedrich, D., & Windbracke, W., *Microelectron. Eng.*, *21*(1), 427–430 (1993).

[20] Yamazaki, T., Goto, K., Fukano, T., Nara, Y., Sugii, T., & Ito, T. In *Proceedings of IEEE Int. Electron Devices Meeting (IEDM)* (pp. 906–908) (1993).

[21] Lu, J. P., Miles, D., Zhao, J., Gurba, A., Xu, Y., Lin, C., Hewson, M., Ruan, J., Tsung, L., Kuan, R., Grider, T., Mercer, D., Montgomery, C. *In Digest. Int. Electron Devices Meeting (IEDM)*, (pp. 371–374) (2002).

[22] Thompson, S., Anand, N., Armstrong, M., Auth, C., Arcot, B., Alavi, M., et al. *In Digest. Int. Electron Devices Meeting (IEDM),* (pp. 61–64) (2002).

[23] Thompson, S., Armstrong, M., Auth, C., Alavi, M., Buehler, M., Chau, R., et al., *IEEE Trans. Electron Devices*, *51*(11), 1790–1797 (2004).

[24] Patterson, O. D., Kang, H. H., Strane, J., Lavoie, C., Barth, K., Ouyang, X., & Wu, K. *In 33rd Int. Symp. for Testing and Failure Analysis, ISTFA 2007,* November 4, 2007 - November 8, 2007 (pp. 270–274). ASM International (2007).

[25] Lin, C., Greene, B., Narasimha, S., Cai, J., Bryant, A., Radens, C., et al. *In 2014 IEEE Int. Electron Devices Meeting(IEDM)* (pp. 3.8.1-3.8.3) (2014).

[26] Guo, D., Karve, G., Tsutsui, G., Lim, K., Robison, R., Hook, T., et al. *In 2016 IEEE Symp. on VLSI Technol.* (p. 14) (2016).

[27] Lavoie, C., Christian, Adusumilli, P., Carr, A. V., Sweet, J. S. J., Ozcan, A. S., Levrau, E., Breil, N., Alptekin, E., *ECS Trans.*, *77*(5), 59–79 (2017).

[28] Shioya, Y., Ikegami, K., Maeda, M., & Yanagida, K., *J. Appl. Phys.*, *61*(2), 561–566 (1987).

[29] Mann, R. W., & Clevenger, L. A., *J. Electrochem. Soc.*, *141*(5), 1347–1350 (1994).

[30] Ting, C. Y., d'Heurle, F. M., Iyer, S. S., & Fryer, P. M., *J. Electrochem. Soc.*, *133*(12), 2621–2625 (1986).

[31] Mann, R. W., Miles, G. L., Knotts, T. A., Rakowski, D. W., Clevenger, L. A., Harper, J. M. E., D'Heurle, F. M., Cabral, C., *Appl. Phys. Lett.*, *67*(25), 3729–3731 (1995).

[32] Cabral, C., Clevenger, L. A., Harper, J. M. E., d'Heurle, F. M., Roy, R. A., Lavoie, C., Saenger, K. L., Miles, G. L., Mann, R. W., Nakos, J. S., *Appl. Phys. Lett.*, *71*(24), 3531–3533 (1997).

[33] Hsieh, Y. F., Chen, L. J., Marshall, E. D., & Lau, S. S., *Appl. Phys. Lett.*, *51*(20), 1588–1590 (1987).

[34] Goto, K.-, Fushida, A., Watanabe, J., Sukegawa, T., Tada, Y., Nakamura, T., Yamazaki, T., Sugii, T., IEEE Trans. Electron Devices, *46*(1), 117–124 (1999).

[35] Lavoie, C., d'Heurle, F. M., Detavernier, C., & Cabral, C., *Microelectron. Eng.*, *70*(2), 144–157 (2003).

[36] Detavernier, C., Van Meirhaeghe, R. L., Cardon, F., & Maex, K., *Phys. Rev. B*, *62*(18), 12045–12051 (2000).

[37] Lavoie, C., Cabral, C., d'Heurle, F. M., Jordan-Sweet, J. L., & Harper, J. M. E., *J. Electron. Mater.*, *31*(6), 597–609 (2002).

[38] Wang, Z., Aldrich, D. B., Chen, Y. L., Sayers, D. E., & Nemanich, R. J., *Thin Solid Films*, *270*(1), 555–560 (1995).

[39] Deal, B. E., & Grove, A. S., *J. Appl. Phys.*, *36*(12), 3770–3778 (1965).

[40] Strane, J., Brown, D., Lavoie, C., Suenaga, J., Haran, B., Press, P., et al. *In 2007 Int. Symp. on VLSI Technol., Syst. Appl. (VLSI-TSA)* (pp. 1–2) (2007).

[41] Zhao, H. B., Pey, K. L., Choi, W. K., Chattopadhyay, S., Fitzgerald, E. A., Antoniadis, D. A., & Lee, P. S., *J. Appl. Phys.*, *92*(1), 214–217 (2002).

[42] Gas, P., & d'Heurle, F. M., Diffusion in silicides. In D. L. Beke (Ed.), Diffusion in Semiconductors and Non-metallic Solids (Vol. 33A, pp. 1–38). Berlin/Heidelberg: Springer-Verlag (1998).

[43] Tian, Y., Jiang, Y.-L., Chen, Y., Lu, F., & Li, B.-Z., *Semicond. Sci. Technol.*, *17*(1), 83 (2002).

[44] Zhang, Z., Atkin, J., Hopstaken, M., Hatzistergos, M., Ronsheim, P., Liniger, E., Laibowitz, R., Solomon, P. M., *IEEE Trans. Electron Devices*, *59*(8), 2027–2032 (2012).

[45] Zhang, Z., Pagette, F., D'Emic, C., Yang, B., Lavoie, C., Zhu, Y., et al., *IEEE Electron Device Lett.*, *31*(7), 731–733 (2010).

[46] Kittl, Jorge A., Lauwers, A., Chamirian, O., Pawlak, M. A., Dal, M. V., Akheyar, A., et al., *MRS Proceedings*, *810* (2004).

[47] Huang, X., Lee, W.-C., Kuo, C., Hisamoto, D., Chang, L., Kedzierski, J., et al., In *Int. Electron Devices Meeting 1999. Technical Digest (IEDM)*, (pp. 67–70) (1999).

[48] Chang, C. Y., Fang, Y. K., & Sze, S. M., *Solid-State Electron.*, *14*(7), 541–550 (1971).

[49] Yu, A. Y. C., *Solid-State Electron.*, *13*(2), 239–247 (1970).

[50] Schroder, D. K., & Meier, D. L., *IEEE Trans. Electron Devices*, *31*(5), 637–647 (1984).

[51] Colinge, J.-P., Lee, C.-W., Afzalian, A., Akhavan, N. D., Yan, R., Ferain, I., et al., *Nat. Nanotechnol.*, *5*(3), 225–229 (2010).

[52] Wang, L., Yu, H., Schaekers, M., Everaert, J., Mocuta, D., Horiguchi, N., Collaert, N., Meyer, K. De., Jiang, Y., *IEEE Trans. Electron Devices*, *65*(5), 1869–1872 (2018).

[53] Yang, Y. R., Breil, N., Yang, C. Y., Hsieh, J., Chiang, F., Colombeau, B., et al., In *2016 IEEE Symp. on VLSI Technol.*, (pp. 1–2) (2016).

[54] Yu, H., Schaekers, M., Schram, T., Aderhold, W., Mayur, A. J., Mitard, J., et al. D., *IEEE Electron Device Lett.*, *37*(4), 482–485 (2016).

[55] Yu, H., Schaekers, M., Rosseel, E., Peter, A., Lee, J.-, Song, W.-, et al., In *2015 IEEE Int. Electron Devices Meeting (IEDM)*, (pp. 21.7.1-21.7.4) (2015).

[56] Niimi, H., Liu, Z., Gluschenkov, O., Mochizuki, S., Fronheiser, J., Li, J., et al., *IEEE Electron Device Lett.*, *37*(11), 1371–1374 (2016).

[57] Yu, H., Schaekers, M., Schram, T., Demuynck, S., Horiguchi, N., Barla, K., Collaert, N., Thean, A. V., Meyer, K. D., *IEEE Trans. Electron Devices*, *63*(7), 2671–2676 (2016).

[58] Agrawal, A., Lin, J., Barth, M., White, R., Zheng, B., Chopra, S., et al., *Appl. Phys. Lett.*, *104*(11), 112101 (2014).

[59] Yu, H., Schaekers, M., Zhang, J., Wang, L., Everaet, J., Horiguchi, N., Jiang, Y., Mocuta, D., Collaert, N., *IEEE Trans. Electron Devices*, *64*(2), 500–506 (2017).

[60] Tanenbaum, Morris, Bell Labs Notebook No. 25505, page 30 (January 26, 1954).

[61] Schuegraf, K., Abraham, M. C., Brand, A., Naik, M., & Thakur, R., *IEEE J. Electron Devices Soc.*, *1*(3), 66–75 (2013).

[62] C. Claeys, E. Simoen, *Germanium-Based Technologies: From Materials to Devices,* (Elsevier, 2007), pp. 246–261.

[63] Chui, C. O., Gopalakrishnan, K., Griffin, P. B., Plummer, J. D., & Saraswat, K. C., *Appl. Phys. Lett.*, *83*(16), 3275–3277 (2003).

[64] Kita, K., Kyuno, K., & Toriumi, A., *Appl. Phys. Lett.*, *85*(1), 52–54 (2004)

[65] Chui, C. O., Kulig, L., Moran, J., Tsai, W., & Saraswat, K. C., *Appl. Phys. Lett.*, *87*(9), 091909 (2005).

[66] Maeda, T., Ikeda, K., Nakaharai, S., Tezuka, T., Sugiyama, N., Moriyama, Y., & Takagi, S., *IEEE Electron Device Lett.*, *26*(2), 102–104 (2005).

[67] Zhang, S.-L., & Östling, M., *Crit. Rev. Solid State Mater. Sci.*, *28*(1), 1–129 (2003).

[68] Gaudet, S., Detavernier, C., Kellock, A. J., Desjardins, P., & Lavoie, C., *J. Vac. Sci. Technol. A*, *24*(3), 474–485 (2006).

[69] Brunco, D. P., Jaeger, B. D., Eneman, G., Mitard, J., Hellings, G., Satta, A., et al., *J. Electrochem. Soc.*, *155*(7), H552–H561 (2008).

[70] Brunco, D. P., Opsomer, K., Jaeger, B. D., Winderickx, G., Verheyden, K., & Meuris, M., *Electrochem. Solid State Lett.*, *11*(2), H39–H41 (2008).

[71] E. Simoen, K. Opsomer, C. Claeys, K. Maex, C. Detavernier, R.L. Van Meirhaeghe, P. Clauws, *Solid State Phenom.*, Vols. 131-133, pp. 47-52 (2008).

[72] L. Lajaunie, M.-L. David, K. Opsomer, E. Simoen, C. Claeys, J. F. Barbot, *Solid State Phenom.*, Vols. 131-133, pp. 107-112 (2008).

[73] Chawanda, A., Nyamhere, C., Auret, F. D., Mtangi, W., Diale, M., & Nel, J. M., *Phys. Status Solidi C*, *7*(2), 248–251 (2010).

[74] Jaafar, R., Nehme, Y., Berling, D., Bubendorff, J. L., Mehdaoui, A., Pirri, C., Garreau, G., Uhlaq-Bouillet, C., Appl. Phys. Lett., *93*(3), 033114 (2008).

[75] Jaafar, R., Berling, D., Sébilleau, D., & Garreau, G., *Phys. Rev. B*, *81*(15), 155423 (2010).

[76] Yoon, H., Lee, A. T., Choi, E.-A., Seo, K., Bagkar, N., Cho, J., Jo, Y., Chang, K. J., Kim, B., *J. Am. Chem. Soc.*, *132*(49), 17447–17451 (2010).

[77] Adelson, E., & Austin, A. E., *J. Phys. Chem. Solids*, 26(12), 1795–1804 (1965).

[78] Janardhanam, V., Kim, J.-S., Moon, K.-W., Ahn, K.-S., & Choi, C.-J., *Microelectron. Eng.*, *89*, 10–14 (2012).

[79] Dixit, H., Niu, C., Raymond, M., Kamineni, V., Pandey, R. K., Konar, A., et al., *IEEE Trans. Electron Devices*, *64*(9), 3775–3780 (2017).

[80] Chou, C., Chang, H., & Wu, Y., *IEEE Electron Device Lett.*, *39*(1), 91–94 (2018).

[81] Koltin, E., & Eizenberg, M., *J. Appl. Phys.*, *71*(9), 4604–4611 (1992).

[82] Genut, M., & Eizenberg, M., *J. Appl. Phys.*, *68*(5), 2146–2157 (1990).

[83] Joo, B. S., Kim, H., Jang, S., Han, D., & Han, M., *J. Phys. Chem. Solids*, *119*, 309–313 (2018).

[84] Stolwijk, N. A., & Lerner, L., *J. Appl. Phys.*, *110*(3), 033526 (2011).

[85] Opsomer, K., Simoen, E., Claeys, C., Maex, K., Detavernier, C., Van Meirhaeghe, R. L., Forment, S., Clauws, P., *Mater. Sci. Semicond. Process.*, *9*(4), 554–558 (2006).

[86] Simoen, E., Opsomer, K., Claeys, C., Maex, K., Detavernier, C., Van Meirhaeghe, R. L., Forment, S., Clauws, P., *Appl. Phys. Lett.*, *88*(18), 183506 (2006).

[87] Simoen, E., Opsomer, K., Claeys, C., Maex, K., Detavernier, C., Van Meirhaeghe, R. L., & Clauws, P., *J. Appl. Phys.*, *104*(2), 023705 (2008).

[88] Ishida, K., & Nishizawa, T., J. Phase Equilib., *12*(1), 77–83 (1991).

[89] Max Hansen, *Constitution of Binary Alloys*, McGraw-Hill, (1958).

[90] Audebrand, N., Ellner, M., & Mittemeijer, E. J., *J. Alloy. Comp.*, *353*(1), 228–232 (2003).

[91] Ashburn, S. P., Öztürk, M. C., Wortman, J. J., Harris, G., Honeycutt, J., & Maher, D. M., *J. Electron. Mater.*, *21*(1), 81–86 (1992).

[92] Rabie, M. A., Mirza, S., Jarvis, V., & Haddara, Y. M., *J. Appl. Phys.*, *121*(14), 145304 (2017).

[93] Ashburn, Stanton P., Öztürk, M. C., Harris, G., & Maher, D. M., *J. Appl. Phys.*, *74*(7), 4455–4460 (1993).

[94] Goldfarb, I., & Briggs, G. A. D., *J. Mater. Res.*, *16*(3), 744–752 (2001).

[95] Kanematsu, K., Yasukōchi, K., & Ohoyama, T., *J. Phys. Soc. Jpn.*, *18*(10), 1429–1436 (1963).

[96] Krontiras, C., Georga, S. N., Sakkopoulos, S., Vitoratos, E., & Salmi, J., *J. Phys. Condens. Matter*, *2*(14), 3323 (1990).

[97] Park, K., An, C.-H., Lee, M. S., Yang, C.-W., Lee, H.-J., & Kim, H., *J. Electrochem. Soc.*, *156*(4), H229–H232 (2009).

[98] Dayer, A., & Feschotte, P., *J. Less-Common. Met.*, *72*(1), 51–70 (1980).

[99] Howell, R. S., Sarcona, G., Saha, S. K., & Hatalis, M. K., *J. Vac. Sci. Technol. A*, *18*(1), 87–93 (2000).

[100] Tung, R. T., Poate, J. M., Bean, J. C., Gibson, J. M., & Jacobson, D. C., *Thin Solid Films*, *93*(1), 77–90 (1982).

[101] Pretorius, R., Marais, T. K., & Theron, C. C., *Mater. Sci. Eng. Rep.*, *10*(1), 1–83 (1993).

[102] Walser, R. M., & Bené, R. W., *Appl. Phys. Lett.*, *28*(10), 624–625 (1976).

[103] Chen, L. J., *Silicide technology for integrated circuits*, Institution of Electrical Engineers (2004), p. 22.

[104] Bené, R. W., *Appl. Phys. Lett.*, *41*(6), 529–531 (1982).

[105] Wittmer, M., Nicolet, M.-A., & Mayer, J. W., *Thin Solid Films*, *42*(1), 51–59 (1977).

[106] Rabie, M. A., Aden-Ali, I., & Haddara, Y. M., In 2017 Int. Conf. on Simul. of Semicond. Processes and Devices (SISPAD), pp. 69–72 (2017).

[107] Dhar, S., & Kulkarni, V. N., *Thin Solid Films*, *333*(1), 20–24 (1998).

[108] Tsuruta, A., Chu, W. G., Tamura, K., Ishii, H., Owari, M., & Nihei, Y., *Surf. Interface Anal.*, *37*(2), 230–234 (2005).

[109] Smith, G. A., Luo, L., Hashimoto, S., Gibson, W. M., & Lewis, N., *J. Vac. Sci. Technol. A*, *7*(3), 1475–1478 (1989).

[110] Shi, J., Ishii, D., Hashimoto, M., Barna, A., Barna, P. B., Haga, Y., & Nittono, O., *J. Crys. Growth*, *222*(1), 235–242 (2001).

[111] Peter, A. P., Opsomer, K., Adelmann, C., Ammel, A. van, Meersschaut, J., Moussa, A., et al., *J. Mater. Chem. C*, *2*(10), 1904–1912 (2014).

[112] Sun, H. P., Chen, Y. B., Pan, X. Q., Chi, D. Z., Nath, R., & Foo, Y. L.. *Appl. Phys. Lett.*, *86*(7), 071904 (2005).

[113] Goldfarb, I., & Briggs, G. A. D., *J Vac Sci Technol B*, *20*(4), 1419–1426 (2002).

[114] Ewert, M., Schmidt, T., Flege, J. I., Heidmann, I., Grzela, T., Klesse, W. M., et al., Nanotechnology, 27, No. 32, p. 325705 (2016).

[115] Choi, J., Lim, D. K., Kim, Y., & Kim, S., *J. Phys. Chem. C*, *114*(19), 8992–8996 (2010).

[116] Vantomme, A., Degroote, S., Dekoster, J., Langouche, G., & Pretorius, R., *Appl. Phys. Lett.*, *74*(21), 3137–3139 (1999).

[117] Grzela, T., Koczorowski, W., Capellini, G., Czajka, R., Radny, M. W., Curson, N., Schofield, S. R., Schubert, M. A., Schroeder, T., *J. Appl. Phys.*, *115*(7), 074307 (2014).

[118] Chawanda, A., Nyamhere, C., Auret, F. D., Mtangi, W., Hlatshwayo, T. T., Diale, M., & Nel, J. M., *Physica B Condens Matter*, *404*(22), 4482–4484 (2009).

[119] Sun, H. P., Chen, Y. B., Pan, X. Q., Chi, D. Z., Nath, R., & Foo, Y. L., *Appl. Phys. Lett.*, *87*(21), 211909 (2005).

[120] Phung, T. H., Xie, R., Tripathy, S., Yu, M., & Zhu, C., *J. Electrochem. Soc.*, *157*(2), H208–H213 (2010).

[121] Lajaunie, L., David, M. L., Pailloux, F., Tromas, C., Simoen, E., Claeys, C., & Barbot, J. F., *Mater. Sci. Semicond. Process.*, *11*(5), 300–304 (2008).

[122] Opsomer, K., Deduytsche, D., Detavernier, C., Van Meirhaeghe, R. L., Lauwers, A., Maex, K., & Lavoie, C., *Appl. Phys. Lett.*, *90*(3), 031906 (2007).

[123] Keyser, K. D., Meirhaeghe, R. L. V., Detavernier, C., Jordan-Sweet, J., & Lavoie, C., *J. Electrochem. Soc.*, *157*(4), H395–H404 (2010).

[124] Prabhakaran, K., & Ogino, T., *Appl. Surf. Sci.*, *100–101*, 518–521 (1996).

[125] Lajaunie, L., David, M. L., & Barbot, J. F., *J. Phys. D: Appl. Phys.*, *44*(12), 125103 (2011).

[126] Hoshi, Y., Sawano, K., Hamaya, K., Miyao, M., & Shiraki, Y., *Appl. Phys. Express*, *5*(1), 015701 (2011).

[127] S. Cea, *Multidimensional viscoelastic modeling of silicon oxidation and titanium silicidation*, Ph.D. Thesis, University of Florida, 1996.

[128] Robert F. Pierret, *Semiconductor Device Fundamentals*, (Addison-Wesley Publishing Company, Inc., 1996), pp. 477–500.

[129] Lieten, R. R., Degroote, S., Kuijk, M., & Borghs, G., *Appl. Phys. Lett.*, *92*(2), 022106 (2008).

[130] Kim, S.-D., Park, C.-M., & Woo, J. C. S., *IEEE Trans. Electron Devices*, *49*(3), 467–472 (2002).

[131] K. Saraswat, Shallow Junctions & Contacts, (Stanford, 2018), http://web.stanford.edu/class/ee311/NOTES/Shallow%20Junctions%20Slides.pdf. Accessed 18 December 2018.

[132] Kasahara, K., Yamada, S., Sawano, K., Miyao, M., & Hamaya, K., *Phys. Rev. B*, *84*(20), 205301 (2011).

[133] Dimoulas, A., Tsipas, P., Sotiropoulos, A., & Evangelou, E. K., *Appl. Phys. Lett.*, *89*(25), 252110 (2006).

[134] Nishimura, T., Kita, K., & Toriumi, A., *Appl. Phys. Lett.*, *91*(12), 123123 (2007).

[135] Zhou, Y., Ogawa, M., Han, X., & Wang, K. L., *Appl. Phys. Lett.*, *93*(20), 202105 (2008).

[136] Han, D., Wang, Y., Tian, D., Wang, W., Liu, X., Kang, J., & Han, R., *Microelectron. Eng.*, *82*(2), 93–98 (2005).

[137] Chawanda, A., Nyamhere, C., Auret, F. D., Mtangi, W., Diale, M., & Nel, J. M., *J Alloys Compd*, *492*(1), 649–655 (2010).

[138] Yao, H. B., Chi, D. Z., Li, R., Lee, S. J., & Kwong, D.-L., *Appl. Phys. Lett.*, *89*(24), 242117 (2006).

[139] Thanailakis, A., & Northrop, D. C., *Solid-State Electron.*, *16*(12), 1383–1389 (1973).

[140] Yamane, K., Hamaya, K., Ando, Y., Enomoto, Y., Yamamoto, K., Sadoh, T., & Miyao, M., *Appl. Phys. Lett.*, *96*(16), 162104 (2010).

[141] Guo, E., Zeng, Z., Zhang, Y., Long, X., Zhou, H., & Wang, X., *Microelectron. Rel.*, *62*, 63–69 (2016).

[142] Sun, S., Sun, Y., Liu, Z., Lee, D.-I., Peterson, S., & Pianetta, P., *Appl. Phys. Lett.*, *88*(2), 021903 (2006).

[143] Prabhakaran, K., Maeda, F., Watanabe, Y., & Ogino, T., *Appl. Phys. Lett.*, *76*(16), 2244–2246 (2000).

[144] Lauwaert, J., Van Gheluwe, J., Vanhellemont, J., Simoen, E., & Clauws, P., *J. Appl. Phys.*, *105*(7), 073707 (2009).

[145] Auret, F. D., Meyer, W. E., Coelho, S., & Hayes, M., *Appl. Phys. Lett.*, *88*(24), 242110 (2006).

[146] Simoen, E., Claeys, C., Sioncke, S., Van Steenbergen, J., Meuris, M., Forment, S., Vanhellemont, J., Clauws, P., Theuwis, A., *J. Mater. Sci. Mater. Electron.*, *18*(7), 799–804 (2007).

[147] Gaubas, E., Vanhellemont, J., Simoen, E., Theuwis, A., & Clauws, P., *MRS Proceedings*, *994* (2007).

[148] Wu, C. S., Scott, D. M., Chen, W., & Lau, S. S., *J. Electrochem. Soc.*, *132*(4), 918–922 (1985).

[149] Kuzmin, M., Laukkanen, P., Mäkelä, J., Tuominen, M., Yasir, M., Dahl, J., Punkkinen, Marko P. J., Kokko, K., *Phys. Rev. B*, *94*(3), 035421 (2016).

[150] Tsipas, P., & Dimoulas, A., *Appl. Phys. Lett.*, *94*(1), 012114 (2009).

[151] Kasahara, K., Yamada, S., Sakurai, T., Sawano, K., Nohira, H., Miyao, M., & Hamaya, K., *Appl. Phys. Lett.*, *104*(17), 172109 (2014).

[152] Weber, J. R., Janotti, A., Rinke, P., & Van de Walle, C. G., *Appl. Phys. Lett.*, *91*(14), 142101 (2007).

[153] Stesmans, A. *Appl. Phys. Lett.*, *68*(15), 2076–2078 (1996).

[154] Afanas'ev, V. V., Fedorenko, Y. G., & Stesmans, A., *Appl. Phys. Lett.*, 87(3), 032107 (2005).

[155] Broqvist, P., Alkauskas, A., & Pasquarello, A., *Phys. Rev. B, 78*(7), 075203 (2008).

[156] Houssa, M., Pourtois, G., Caymax, M., Meuris, M., Heyns, M. M., Afanas'ev, V. V., & Stesmans, A., *Appl. Phys. Lett., 93*(16), 161909 (2008).

[157] Baldovino, S., Molle, A., & Fanciulli, M., *Appl. Phys. Lett., 96*(22), 222110 (2010).

[158] Paleari, S., Baldovino, S., Molle, A., & Fanciulli, M., *Phys. Rev. Lett., 110*(20), 206101 (2013).

[159] Yeo, Y.-C., King, T.-J., & Hu, C., *J. Appl. Phys., 92*(12), 7266–7271 (2002).

[160] Louie, S. G., & Cohen, M. L., *Phys. Rev. B, 13*(6), 2461–2469 (1976).

[161] Muller, D. A., Shashkov, D. A., Benedek, R., Yang, L. H., Silcox, J., & Seidman, D. N., *Phys. Rev. Lett., 80*(21), 4741–4744 (1998).

[162] Thornton, R. L., *Electron. Lett., 17*(14), 485–486 (1981).

[163] Kamineni, V., Carr, A., Niu, C., Adusumilli, P., Abrams, T., Xiel, R., et al., *In 2018 IEEE Int. Interconnect Technol. Conf. (IITC)*, (pp. 28–29) (2018).

[164] Li, Zhiqiang, *The Source/Drain Engineering of Nanoscale Germanium-based MOS Device*, (Springer, 2016), Chapter 2 pp. 11–**26**.

[165] Mueller, M., Zhao, Q. T., Urban, C., Sandow, C., Buca, D., Lenk, S., Estevez, S., Mantl, S., *Mater. Sci. Eng., B, 154–155*, 168–171 (2008).

[166] Grimmeiss, H. G., Montelius, L., & Larsson, K., *Phys. Rev. B, 37*(12), 6916–6928 (1988).

[167] Tong, Y., Liu, B., Lim, P. S. Y., & Yeo, Y., *IEEE Electron Device Lett., 33*(6), 773–775 (2012).

[168] Ikeda, K., Yamashita, Y., Sugiyama, N., Taoka, N., & Takagi, S., *Appl. Phys. Lett., 88*(15), 152115 (2006).

[169] Thathachary, A. V., Bhat, K. N., Bhat, N., & Hegde, M. S., *Appl. Phys. Lett., 96*(15), 152108 (2010).

[170] Kobayashi, M., Kinoshita, A., Saraswat, K., Wong, H.-P., & Nishi, Y., In 2008 Symp. on VLSI Tech. (pp. 54–55) (2008).

[171] Connelly, D., Faulkner, C., Grupp, D. E., & Harris, J. S., *IEEE Trans. Nanotechnol.*, *3*(1), 98–104 (2004).

[172] Kim, G.-S., Kim, S.-W., Kim, S.-H., Park, J., Seo, Y., Cho, B. J., Shin, C., Shim, J. H., Yu, H.-Y., *ACS Appl. Mater. Interfaces*, *8*(51), 35419–35425 (2016).

[173] Li, Z., An, X., Yun, Q., Lin, M., Zhang, X., & Huang, R., *ECS Solid State Lett.*, *1*(4), Q33–Q34 (2012).

[174] Zhou, Y., Han, W., Wang, Y., Xiu, F., Zou, J., Kawakami, R. K., & Wang, K. L., *Appl. Phys. Lett.*, *96*(10), 102103 (2010).

[175] Kobayashi, M., Kinoshita, A., Saraswat, K., Wong, H.-S. P., & Nishi, Y., *J. Appl. Phys.*, *105*(2), 023702 (2009).

[176] Wu, H. D., Wang, C., Wei, J. B., Huang, W., Li, C., Lai, H. K., Li, j., Liu, C., Chen, S. Y., *IEEE Electron Device Lett.*, *35*(12), 1188–1190 (2014).

[177] Ranade, P., Choi, Y.-K., Ha, D., Agarwal, A., Ameen, M., & King, T.-J. *In Digest. Int. Electron Devices Meeting (IEDM)*, (pp. 363–366) (2002).

[178] Smoluchowski, R., *Phys. Rev.*, *60*(9), 661–674 (1941).

[179] Wronski, C. R., Carlson, D. E., & Daniel, R. E., *Appl. Phys. Lett.*, *29*(9), 602–605 (1976).

[180] Mello, K. E., Murarka, S. P., Lu, T.-M., & Lee, S. L., *J. Appl. Phys.*, *81*(11), 7261–7267 (1997).

[181] S. M. Sze and Kwok K. Ng, *Physics of semiconductor devices*, 3rd Edition, (John Wiley & Sons, Inc., 2007), p. 353.

[182] Blauwe, J. D., *IEEE Trans. Nanotechnol.*, *99*(1), 72–77 (2002).

Chapter 5

Conclusion and Future Work

Cobalt germanide is a candidate material for the formation of high quality contacts that would solve major technological problems in multiple critical application areas. It is a candidate for the formation of low resistivity contacts manufacturable at low temperatures that are needed for advanced CMOS technology where the specific contact resistivity has become the most severe challenge to low overall contact resistance. It is also a candidate for contacts in GaN power electronic devices to reduce heating losses at the contact interface, which is one of the major obstacles in developing that technology. In this thesis we have focused on the study of the formation of the germanide both theoretically and experimentally and we have investigated the electrical properties of the contact and the factors that affect them.

Advanced silicon CMOS technology is approaching its physical limit due to continuous device scaling. High mobility channel materials such as Ge have been extensively studied as candidates for replacing silicon for continuous device improvement [1-6]. The instability of the germanium oxide that was seen as a disadvantage in early days of semiconductors turned out to be an advantage in case of using high-k dielectrics. For the same deposition oxide, the interfacial oxide thickness is significantly lower in case of a Ge substrate compared with Si [7] resulting in a higher quality high-k gate dielectric. One of the main issues that have been observed in case of Ge devices is the difficulty of formation of an ohmic metallic contact on n-type Ge [8-11]. Despite forming ohmic contacts on p-type Ge, metals tend to form Schottky contacts on n-type Ge with a Schottky barrier height (SBH) ranging between 0.49eV to 0.65eV [8-11]. The Schottky behavior has been attributed to Fermi Level Pinning (FLP). The range of the SBH reported for different n-Ge crystal orientation was different for (100) compared to (111) [12-14]. The SBH was variable and no FLP was observed in case of (111) n-Ge.

The main criterion for choosing a contact in the state-of-the-art advanced CMOS technology is the interface contact resistivity [15] which is exponentially dependent on the SBH [16]. Titanium silicides have been the preferred contacts by the industry in recent years and substantial effort have taken place to minimize the titanium

silicide-silicon interface contact resistivity [17-20] with a record low of $8.4x10^{-10}$ohm.cm^2 [20]. Such a low resistivity could only be achieved by using amorphizing high dose implants and recrystallizing Si using solid phase epitaxial regrowth. The high active dopant concentration at the interface results in substantial carrier tunneling through the narrow Schottky barrier at the contact interface decreasing the intrinsic resistivity and mimicking ohmic behavior [21]. Heavy doping is not a feasible solution for some applications including solar cells in which low doping in the contact region is needed to have high efficiency [22] and junction-less nanowires transistors, recently suggested, to replace conventional transistors [23]. On the other hand, some phases of cobalt silicides grow epitaxially on silicon and that gives them by default an advantage over titanium silicides [24]. The Schottky barrier height of crystalline contacts displays a lower value than that of their amorphous counterparts [25]. Cobalt silicides were abandoned by the industry upon the incorporation of Ge in the devices for the purpose of enhancing the mobility through stress engineering [26, 27]. The main reason being that the low resistivity cobalt silicide phase: $CoSi_2$ forms only after Ge is expelled from CoSi at impractically high temperatures [26, 27].

On the contrary to cobalt silicides, cobalt germanides form at lower temperatures [28, 29] since the inward diffusion of cobalt into the underlying bulk Ge is 150˚C compared to 350˚C in bulk Si [30]. In addition, the equilibrium concentrations of interstitials and vacancies are higher in Ge than in Si at the same temperature [30]. Theoretically, it should be possible to grow some single crystalline cobalt germanides phases on germanium since the lattice mismatch is small: 2.7% for Co_5Ge_7 and 0.4% for $CoGe_2$ compared to 7.5% in case of titanium germanide. Single crystalline $CoGe_2$ phase was grown on Ge by Choi et al. [32]. Partial epitaxial Co_5Ge_7 and $CoGe_2$ were reported by a number of other researchers [24, 33, 34]. Therefore, cobalt germanides could also be good candidates for contacts to germanium and silicon germanium devices. Cobalt germanides also form high quality ohmic contacts to wide bandgap semiconductors like GaAs [35, 36].

In this chapter a summary of our contributions towards the process design for forming a high quality cobalt germanide contact to germanium based devices is first presented. Epitaxial cobalt germanides are expected to minimize FLP contribution and, consequently, have a very low interface resistivity. The limitations of the TCAD

model presented in chapter 3 will be presented in the following section along with suggestions for future work to conclude the chapter.

1- Summary of Contributions

The first requirement in obtaining a high quality cobalt germanide contact is to have a single phase germanide to avoid resistivity variations. Four phases form during cobalt germanidation: Co_5Ge_3, CoGe, Co_5Ge_7, and $CoGe_2$. There was experimental and theoretical controversy in the literature regarding the first phase to form during cobalt germanidation. The main thermodynamic phase formation model, effective heat of formation (EHF), identifies CoGe as the phase with lowest EHF but this phase is non-congruent. The only congruent phase is Co_5Ge_3. The model suggests that Co_5Ge_3 would then be the first phase to form since non-congruent phases are usually skipped. The model was 80% successful to predict the first phase to form. Therefore, it cannot confirm with certainty that Co_5Ge_3 is the first phase to form. Temperature ramp-up experiments, on the other hand, show the first phase to form to be CoGe. Solid-state anneal experiments showed the first phase to form to be Co_5Ge_3. We conducted a set of long time low temperature anneal experiments with in-situ phase monitoring to investigate the first phase to form and were able to identify it to be Co_5Ge_3 settling the controversy regarding the first phase to form. The main difference between our experiments and previously conducted experiments is the in-situ XRD monitoring of the phase forming during the reaction. An important outcome of the experiments was that both Co_5Ge_3 and CoGe were partially epitaxial phases. This semi-epitaxial growth makes these phases potentially good candidates for low-temperature high quality contacts. The low thermal budget is very appealing for the process designer since it is compatible with the middle of line and back end of line processes to follow the contact formation.

We were able to experimentally observe the transformation of Co_5Ge_3 into CoGe at the same reaction temperature, 227°C, using in-situ XRD. This observation and other experimental results reported in the literature led us to understand how the solid state germanidation reaction proceeds. For each of the four phases nucleation happens above a critical temperature. The phases form in sequence. Co_5Ge_3 forms first. Once Co is consumed or if the reaction becomes diffusion limited the next phase, CoGe, will start to form. If the experimental temperature is

above the critical nucleation temperature of Co_5Ge_7 and once Co_5Ge_3 is consumed or if the reaction becomes diffusion limited the next phase Co_5Ge_7 will form. Similar kinetics applies for the last and most stable phase $CoGe_2$. We were able to represent this physical model mathematically and implemented the mathematical model in a TCAD process simulator, SProcess. The model was calibrated to our experimental results as well as other results reported in the literature. This model is the first calibrated predictive multiphase model for germanidation or silicidation reaction. It is capable of predicting the forming phase among the four phases of cobalt germanides: Co_5Ge_3, CoGe, Co_5Ge_7, $CoGe_2$, the composition of the germanide in case of mixed phase experiment, and the thickness of the forming germanide layer. The inputs to the model are germanidation time, temperature, and ambient. The model gives the designer the capability to design a high quality contact by using different process parameters as inputs to a simulation and concluding the phase and the thickness of the cobalt germanide contact from the simulation. This model can help in the design of single-phase low-resistivity cobalt germanide contacts. While the model was calibrated for cobalt germanidation process, it can be generally used for any multiphase binary system. It can be calibrated and applied for any silicide or germanide growth reaction resulting in more than a single phase.

The experiments selected to calibrate the model presented in chapter 3 used solid-state anneal at a constant temperature where Co was sputtered on Ge. Other experimental setups result in different germanide phases or different quality of the germanide for the same time, temperature, and ambient conditions. It became clear that other factors contribute to the resulting phase and the quality of the germanide. To understand those factors the experimental results for cobalt germanidation were extensively reviewed in a survey presented in chapter 4. Based on the survey, we concluded that there are mainly three different methods that have been used for cobalt germanidation. Reactive deposition, the first method, yields interfacial germanides at temperatures as low as room temperature. The thickness of such layer is not easily controlled and the slow deposition methods used are impractical for industrial mass production. In addition, mixed phases have been observed even at temperatures as high as 650°C. Temperature ramp-up experiments result in high formation temperatures compared to solid state anneal at a constant temperature. Therefore, solid state anneal at a constant temperature seems to be the best option for contact formation. The effect of other factors on the phase and the quality of the germanide was evaluated including the crystallinity of Ge, mechanical strain, microstructure, and the pretreatment of the surface. N_2 as an

ambient slows down the reaction. As the crystallinity of Ge increases, higher temperatures are needed to form $CoGe_2$. The crystalline structures ordered from low to high germanide formation temperatures are: amorphous, polycrystalline, (100) and finally (111)-Ge. Higher temperature germanidation should be avoided to eliminate the possibility of Co in-diffusion into the Ge substrates. Such behavior has been seen at 600°C and above [71]. Compressive strain appears to enhance the germanidation reaction and tensile strain appears to retard the reaction based on some of the experimental reports. More experimental results are needed to confirm the effect of strain.

The main practical factor that determines the quality of the germanide is its electrical properties. We evaluated the electrical interface resistivity of various cobalt germanide phases and the parameters controlling that resistivity. The role of germanium crystal orientation in ohmic and Schottky properties of the contact was analyzed. We concluded that FLP plays a role only on one of four interfaces, that is, the germanide/(100) n-Ge interface. No evidence of FLP on other interfaces including p-type Ge interfaces and germanide/(111) n-Ge interface. Schottky barrier heights for cobalt and cobalt germanide contacts reported in the literature were surveyed. Multiple values have been reported for the SBH at Co/(100) n-type Ge interface [34, 37-41] ranging between 0.28eV [40] and 0.62eV [37] but Co/p-type Ge (100) interface has ohmic characteristics [37]. Similarly, a range of SBH's has been measured by different researchers for different phases of cobalt germanides [38, 40-42]. Factors contributing to the variation in SBH's were identified. Those include the phase of the germanide, the crystallinity of Ge and the germanide, the surface pretreatment before Co deposition, the deposition method of Co, and the doping profile in Ge. Epitaxial cobalt germanides are expected to reduce the SBH significantly. We identified the main technique used to grow such epitaxial germanides which is high temperature Co deposition followed by a constant temperature anneal.

2- Limitations and Future Work

Prior to this work, little attention was given to cobalt silicides and germanides as contacts for advanced CMOS technology nodes. Cobalt silicides and germanides could be viable candidates to contact the source and drain regions in 3D devices. More research and contact resistivity optimization is needed to understand the capabilities of cobalt silicides as liner contacts as compared to titanium silicides. Cobalt silicides grow epitaxially on silicon and that

gives them by default an advantage over titanium silicides. However, no recent attempts have been made to lower the contact resistivity of cobalt silicides. Cobalt germanides have shown variability in the Schottky and ohmic behaviors as discussed in the thesis. Multiple factors contribute to the variation in SBH's including the phase of the germanide, the crystallinity of Ge and the germanide, the surface pretreatment before Co deposition, the deposition method of Co, and the doping profile in Ge. While multiple researchers indicated those factors, a systematic study is still lacking to quantify the contributions of each of those parameters to the behavior of the contact and the SBH. The understanding of the electric behavior of Co germanides on (111)Ge has not yet been reported both for n- and p-types. Most schemes for GaAs contact metallization require alloying. The alloying process is known to introduce nonhomogeneous interface morphology and potentially spiking problem. $CoGe_2$ is a high melting contact with a small mismatch to GaAs. High quality epitaxial $CoGe_2$ layer was grown on GaAs. The electrical properties of the contact on GaAs still need to be studied.

Single crystalline phases have not yet been achieved reliably. Such phases might be of great importance to the contact formation since they are expected to have very low contact resistivity without having to depin the interface by introducing heavy doping. In addition to advanced CMOS applications, such contacts will be very attractive for solar cells and junction-less transistors. Epitaxial Co germanides could be achieved using high temperature Co deposition followed by an anneal step or by using reactive deposition. Future experiments should focus on creating epitaxial Co germanide contacts and measuring their interfacial resistivities and SBH. Low-temperature phases, Co_5Ge_3 and CoGe, could potentially serve as good contacts since they have been shown to be partially epitaxial. Experimental measurements of bulk and interfacial resistivities of those low-temperature phases would be needed to evaluate the quality of those phases as contacts. Heavy doping fermi level depinning technique could also be employed in case of cobalt germanides to be compared to titanium germanides performance.

The kinetic model presented in chapter 3 could be improved by taking into account the nucleation temperatures of various phases as a limiting factor. In addition, the model could be used for other experimental conditions like reactive deposition by using different activation energy for the reaction terms. It can also be extended to incorporate other factors like strain, pretreatement of the surface. More experimental data is needed to understand the

crystallinity of the resulting germanide. The model could be of great benefit if it is able to predict the crystallinity of the resulting phase.

References

[1] Wu et al. “First experimental demonstration of Ge CMOS circuits,” IEDM 2014.

[2] A. Toriumi, et al., IEDM 2011, p.28.4.1.

[3] R. Pillarisetty, Nature, p. 324, 2011.

[4] B. Duriez, et al., IEDM 2013, p.522.

[5] J. Mitard, et al., IEDM 2008, p.876.

[6] B. Liu, et al., IEDM 2013, p.657

[7] E. H. Rhoderick and R. H. William, Metal-Semiconductor Contacts Clarendon, Oxford, 1988.

[8] Kasahara, K., S. Yamada, K. Sawano, M. Miyao and K. Hamaya (2011). "Mechanism of Fermi level pinning at metal/germanium interfaces." Physical Review B **84**(20).

[9] A. Dimoulas, P. Tsipas, A. Sotiropoulos, and E. K. Evangelou, "Fermi-level pinning and charge neutrality level in germanium," *Applied Physics Letters*, vol. 89, p. 252110, 2006.

[10] Nishimura et al., APPLIED PHYSICS LETTERS **91**, 123123 (2007)

[11] Zhou Y, Ogawa M, Han X, Wang KL (2008) “Alleviation of Fermi-level pinning effect on metal/germanium interface by insertion of an ultrathin aluminum oxide.” Appl Phys Lett 93:202105–202105-3

[12] K. Yamane, K. Hamaya, Y. Ando, Y. Enomoto, K. Yamamoto, T. Sadoh, and M. Miyao, Appl. Phys. Lett. 96, 162104 (2010)

[13] A. Thanailakis and D. C. Northrop, Solid-State Electron. 16, 1383 (1973)

[14] Guo, Erjuan, Zhigang Zeng, Yan Zhang, Xiao Long, Haijun Zhou, and Xiaohong Wang. 2016. "The effect of annealing temperature on the electronic parameters and carrier transport mechanism of Pt/n-type Ge Schottky diode." Microelectronics Reliability no. 62:63-69

[15] Christian Lavoie, Praneet Adusumilli, Adra V. Carr, Jean S. Jordan Sweet, Ahmet S. Ozcan, Elisabeth Levrau, Nicholas Breil, and Emre Alptekin, "Contacts in Advanced CMOS: History and Emerging Challenges," ECS Transactions, 77 (5) 59-79 (2017).

[16] C. Y. Chang, Y. K. Fang, and S. M. Sze, "Specific contact resistance of metal-semiconductor barriers," *Solid-State Electron.*, vol. 14, no. 7, pp. 541–550, Jul. 1971.

[17] Y. R. Yang, N. Breil, C. Y. Yang, J. Hsieh, F. Chiang, B. Colombeau, B. N. Guo, K. H. Shim, N. Variam, G. Leung, J. Hebb, S. Sharma, C. N. Ni, J. Ren, J. Wen, J. H. Park, H. Chen, S. Chen, M. Hou, D. Tsai, J. Kuo, D. Liao, M. Chudzik, S. H. Lin, H. F. Huang, N. H. Yang, J. F. Lin, C. T. Tsai, G. C. Hung, S. C. Hsu, O. Cheng, J. Y. Wu, and T. R. Yew, IEEE Symp. VLSI Technology, 2016, p. 1.

[18] H. Yu, M. Schaekers, T. Schram, W. Aderhold, A. J. Mayur, J. Mitard, L. Witters, K. Barla, N. Collaert, N. Horiguchi, A. V. Y. Thean, and K. D. Meyer, IEEE Electron Device Lett. 37, 482 (2016).

[19] H. Yu, M. Schaekers, E. Rosseel, A. Peter, J.-G. Lee, W.-B. Song, S. Demuynck, T. Chiarella, J. Ragnarsson, S. Kubicek, J. Everaert, N. Horiguchi, K. Barla, D. Kim, N. Collaert, A. V.-Y. Thean, and K. De Meyer, "1.5×10-9 cm2 contact resistivity on highly doped Si:P using Ge pre-amorphization and Ti silicidation," in Proc. IEEE Int. Electron Devices Meeting (IEDM), Dec. 2015, pp. 21.7.1–21.7.4.

[20] H. Niimi *et al.*, "Sub- $10^{-9}~\Omega $ -cm2 n-Type Contact Resistivity for FinFET Technology," in *IEEE Electron Device Letters*, vol. 37, no. 11, pp. 1371-1374, Nov. 2016.

[21] A. Y. C. Yu, "Electron tunneling and contact resistance of metal-silicon contact barriers," *Solid-State Electron.*, vol. 13, no. 2, pp. 239–247, Feb. 1970.

[22] D. K. Schroder and D. L. Meier, “Solar cell contact resistance—A review,” *IEEE Trans. Electron Devices*, vol. ED-31, no. 5, pp. 637–647, May 1984.

[23] J.-P. Colinge *et al.*, “Nanowire transistors without junctions,” *Nature Nanotechnol.*, vol. 5, no. 3, pp. 225–229, Mar. 2010.

[24] Y. F. Hsieh, L. J. Chen, E. D. Marshall, and S. S. Lau, “Partial epitaxial growth of cobalt germanides on (111) Ge,” Appl. Phys. Lett., 51, P. 1588, 1987.

[25] C. R. Wronski, D. E. Carlson and R. E. Daniel. (1976). “Schottky-barrier characteristics of metal-amorphous-silicon diodes,” Applied Physics Letters. 29. P. 602.

[26] C . Lavoie, C. Cabral Jr., F.M. d’Heurle, J.L. Jordan-Sweet, J.M.E. Harper, J. Electron. Mater. 31 (2002) 597.

[27] Z. Wang, D.B. Aldrich, Y.L. Chen, D.E. Sayers, and R.J. Nemanich, *Thin Solid Film* 270, 555 (1995).

[28] Rabie et al. “First phase during cobalt germanidation,” JAP 2017.

[29] Rabie et al. SISPAD 2017.

[30] K. Prabhakaran and Ogino, “Behavior of ultrathin layers of Co on Si and Ge systems,” Applied Surface Science 100/101, 518 (1996).

[31] Zhang, S.-L.; Ostling, M. Metal Silicides in CMOS Technology: Past, Present, and Future Trends., *Crit. Rev. Solid State* 2003, *28*, 1–129.

[32] J. Choi, D. K. Lim, Y. Kim, and S. Kim, “Structural and Electronic Properties of Cobalt Germanide Islands on Ge(100),” J. Phys. Chem. C 2010, 114, 8992-8996.

[33] H. P. Sun, Y. B. Chen, X. Q. Pan, D. Z. Chi, R. Nath, and Y. L. Foo, “Formation and evolution of epitaxial Co5Ge7 on Ge(001) surface by reactive deposition inside an ultrahigh-vacuum transmission electron microscope,” APL 86, 071904 (2005).

[34] L. Lajaunie, M. L. David, F. Pailloux, C. Tromas, E. Simoen, C. Claeys, and J. F. Barbot, "Influence of the pre-treatment anneal on Co-germanide Schottky contacts," Materials Science in Semiconductor Processing, V. 11, 5-6, (2008), 300-304.

[35] E. Koltin and M. Eizenberg, "Ge-rich Co-Ge contacts to n-type GaAs," J. Appl. Phys. 71 (9), 1992.

[36] M. Genut and M. Eizenberg, "Study of the Co-Ge/GaAs contact system," Journal of Applied Physics 68, 2146 (1990)

[37] Zhou Y, Ogawa M, Han X, Wang KL (2008) Alleviation of Fermi-level pinning effect on metal/germanium interface by insertion of an ultrathin aluminum oxide. Appl Phys Lett 93:202105–202105-3

Appendix A: TCAD Model Code

```
# This command sets up the initial calibration from synopsys

AdvancedCalibration

math pardiso

mater add name=CoO

ambient name=O2 react add

reaction name= CoOreaction mat.l=Cobalt mat.r=Gas mat.new=CoO \

new.like= Oxide ambient.name= O2 diffusing.species= O2

solution name= O2 add !negative GrowthStep solve

pdbSetString CoO O2 Equation "ddt(O2)- \[Arrhenius 1e12 1.86\]*grad(O2)"

pdbSetString Gas_CoO O2 Equation_CoO "-(O2_CoO - 1e20)"

pdbSetString Cobalt_CoO O2 Equation_CoO "-5e2*(O2_CoO)"

pdbSetString Cobalt_CoO O2 GrowthReaction " 1e10*(O2_CoO)"



# Add CobaltGermanide material to the global material list

mater add name= CobaltGermanide new.like= NickelSilicide
```

Name of the reaction

The material names for left & right sides

Specifies a valid material name as the product of the reaction

Name of the existing material that the new material is behaving like

List of reactants for material growth reactions

reaction name= CobaltGermanide mat.l= Germanium mat.r= Cobalt mat.new= CobaltGermanide new.like= NickelSilicide diffusing.species= GermaniumReact

Density or bulk equilibrium molecular/atomic concentrations of cobalt and cobalt germanides

set CCoGe0 3.73e22

set CCo5Ge30 1.525083e22

set CCo0 9.1e22

set CCoGe20 2.305e22

set CCo5Ge70 5.9296394e21

Reaction constants used for calibration

set k1 1e5

set k2 "\[Arrhenius 1.962e7 1.319\]"

set k3 "\[Arrhenius 4.675e12 1.99\]"

set k4 "\[Arrhenius 9.2695e9 1.972\]"

solution name= CCoGe2 add !negative !damp solve

solution name= CCo5Ge7 add !negative !damp solve

solution name= CCoGe add !negative !damp solve

solution name= CCo5Ge3 add !negative !damp solve

solution name= CCo add !negative !damp solve

solution name= GermaniumReact add !negative !damp solve

pdbSetString CobaltGermanide CCoGe2 Equation "ddt(CCoGe2)-(5/3)*$k4*((CCo5Ge7/$CCo5Ge70))*GermaniumReact"

pdbSetString CobaltGermanide CCo5Ge7 Equation "ddt(CCo5Ge7)-(1/2)*$k3*((CCoGe/$CCoGe0))*GermaniumReact+(1/3)*$k4*((CCo5Ge7/$CCo5Ge70))*GermaniumReact"

pdbSetString CobaltGermanide CCoGe Equation "ddt(CCoGe)-(5/2)*$k2*((CCo5Ge3/$CCo5Ge30))*GermaniumReact+(5/2)*$k3*((CCoGe/$CCoGe0))*GermaniumReact"

pdbSetString CobaltGermanide CCo5Ge3 Equation "ddt(CCo5Ge3)-(1/3)*$k1*((CCo/$CCo0))*GermaniumReact+(1/2)*$k2*((CCo5Ge3/$CCo5Ge30))*GermaniumReact"

pdbSetString CobaltGermanide CCo Equation "ddt(CCo)+(5/3)*$k1*((CCo/$CCo0))*GermaniumReact"

pdbSetString CobaltGermanide GermaniumReact Equation "ddt(GermaniumReact)- \[Arrhenius @GePreDiff@ 1.86\]*grad(GermaniumReact)+$k4*(CCo5Ge7/$CCo5Ge70)*GermaniumReact+$k3*(CCoGe/$CCoGe0)*GermaniumReact+$k2*(CCo5Ge3/$CCo5Ge30)*GermaniumReact+$k1*(CCo/$CCo0)*GermaniumReact"

P568 Alagator language for diffusion equation

Arrhenius expression 0.2*e^(-1.86/kT)

set CGeStar 1e17

pdbSetString Cobalt_CobaltGermanide GermaniumReact Equation_CobaltGermanide "-\[Arrhenius @GePreDiff@ 1.86\]*(GermaniumReact_CobaltGermanide - CGeStar)"

Setting equilibrium concentrations of reaction components in the bulk sides

pdbSetBoolean Germanium_CobaltGermanide GermaniumReact Fixed_CobaltGermanide 1

pdbSetString Germanium_CobaltGermanide GermaniumReact Equation_CobaltGermanide "GermaniumReact_CobaltGermanide-4.4e22"

pdbSetString Cobalt_CobaltGermanide CCo Equation_Cobalt "CCo_Cobalt-9.1e22"

pdbSetString Cobalt_CobaltGermanide CCo5Ge3 Equation_CobaltGermanide "CCo5Ge3_CobaltGermanide-1.525e22"

Growth reaction of cobalt germanide

pdbSetString Cobalt_CobaltGermanide GermaniumReact GrowthReaction "(1/3)*$k1*(CCo/$CCo0)*(GermaniumReact_CobaltGermanide)"

pdbSetDouble Cobalt_CobaltGermanide GermaniumReact Beta [expr 5/3]

pdbSetDouble Cobalt_CobaltGermanide GermaniumReact Expansion.Ratio [expr (65.57*$r1+26.80875*$r2+168.625*$r3+43.385*$r4)/(11.205*(5*$r1+$r2+5*$r3+$r4))]

pdbSetDouble Cobalt_CobaltGermanide GermaniumReact Density.Grow $CCo0

pdbSetDouble Germanium_CobaltGermanide GermaniumReact Beta 1

pdbSetDouble Germanium_CobaltGermanide GermaniumReact Expansion.Ratio [expr (65.57*$r1+26.80875*$r2+168.625*$r3+43.385*$r4)/(22.545*(5*$r1+$r2+5*$r3+$r4))]

pdbSetDouble Germanium_CobaltGermanide GermaniumReact Density.Grow [expr [pdbGetDouble Cobalt_CobaltGermanide GermaniumReact Beta]*(5.0*$r1+$r2+5.0*$r3+2.0*$r4)/(65.57*$r1+26.80875*$r2+168.625*$r3+43.385*$r4)]

Define the boundaries of the structure in 2D location mesh lines space the lines of interest

line x loc= 0.0<um> spacing=0.1<um> tag=SubTop

line x loc= 3.0<um> spacing=0.1<um>

```
line x loc= 6.0<um> spacing=0.7<um> tag=SubBottom

line y loc= 0.0<um>                 tag=Left

line y loc= 1.0<um>                 tag=Right


# Use the unified coordinate system (UCS) to define the mesh for the simulation

math coord.ucs


region Germanium xlo=SubTop xhi=SubBottom ylo=Left yhi=Right


# Specify the principal wafer orientation

#if @wafer@==0

init !DelayFullD wafer.orient= {0 0 1}

#else

init !DelayFullD wafer.orient= {1 1 1}

#endif

grid set.min.normal.size= 0.1<nm> set.normal.growth.ratio.2d= 1.1 set.min.grid= 0.01<nm>

pdbSet Grid NativeLayerThickness 1.0e-7

pdbSet Silicon Grid Remove.Dist 3.0e-8

pdbSet Germanium Grid Remove.Dist 3.0e-8
```

pdbSet Cobalt Grid Remove.Dist 3.0e-8

pdbSet CobaltGermanide Grid Remove.Dist 3.0e-8

refinebox interface.materials= { Germanium Cobalt CobaltGermanide } min.normal.size= 0.1<nm> normal.growth.ratio= 1.1

pdbSet CobaltGermanide Grid perp.add.dist 0.5e-7

Deposit a Cobalt layer with thickness

deposit CobaltGermanide thickness=1<nm> species= CCo5Ge3 concentration= 1.525083e22

deposit Cobalt thickness=@Cobalt@<nm>

#deposit Silicon thickness= 50<nm>

struct tdr= n@node@_1

pdbSet Diffuse minT 150

pdbSet Diffuse minAnnealT 150

Diffusion conditions Annealing temperature time pressure of the ambient gas flow of Nitrogen minimum annealing temperature

#if @O2@==0

diffuse temperature=@temperature@<C> time=@time@<min> pressure=@pressure@<torr> flowN2=1<l/min> minT=200<C> info= 1

#else

```
  diffuse temperature=@temperature@<C> time=@time@<min> pressure=@pressure@<torr> O2 minT=200<C>
info= 1

#   diffuse temperature=500<C> time=1<hr> pressure=@pressure@<torr> O2 minT=200<C> info= 1

#endif

# select store name= CoFraction z= CCo/(CCo+CCo5Ge3+CCoGe2+CCoGe+CCo5Ge7)

select store name= Co5Ge3Fraction z= CCo5Ge3/$CCo5Ge30

select store name= CoGeFraction z= CCoGe/$CCoGe0

select store name= Co5Ge7Fraction z= CCo5Ge7/$CCo5Ge70

select store name= CoGe2Fraction z= CCoGe2/$CCoGe20



# Layers thicknesses in nm

select z=1e7

set thick [lindex [lindex [layers y=0.5] 2] 2]

puts "DOE: Thickness $thick"



# Save structure

struct tdr=n@node@
```